MASTER'S THESIS

IMPROVEMENTS IN LOCALIZATION OF PLANAR ACOUSTIC HOLOGRAPHY

Philipp Schmidt

Supervisor: DI. Dr. Franz Zotter
Assessor: o.Univ. - Prof. Mag. DI. Dr. Robert Höldrich

Institute of Electronic Music and Acoustics
University of Music and Performing Arts Graz

May 29, 2012

institut für elektronische musik und akustik

Dedicated to the loving memory of Friedrich Luttmann

ABSTRACT

To describe a soundfield in planar nearfield holography it is mathematically sufficient to know the boundary values. Inverse equations can be set up to trace back the sound waves to their source, based on measurements of the sound pressure. Available techniques are based on solutions of the Helmholtz equation or the Helmholtz integral equation and are frequently applied in noncontact measurement scenarios. These are, for instance, the wave superposition method (WSM), Helmholtz equation least squares (HELS), inverse boundary element method (IBEM), nearfield acoustic holography (NAH) or the statistically optimized NAH (SONAH).

All these approaches have a tendency to be numerically ill-posed and are usually treated using the classical ℓ_2-norm based system inversion techniques. How to deal with spatial aliasing, boundary wrap-around and loss or numerical instability is well discussed, however, available literature does not excessively address the poor point localization of these techniques. In this thesis, the mapping properties of ℓ_1-optimized planar holography is discussed and compared with ℓ_2-optimized calculation. To reveal different types of algorithmic behavior, a simulation of the soundfield is calculated for different types of sources.

ZUSAMMENFASSUNG

Um das Schallfeld mit Hilfe der planaren Nahfeldholografie (PNAH) zu beschreiben genügt es, das Feldes an definierten Grenzen zu kennen. Basierend auf Schalldruckmessungen können inverse Gleichungssysteme angesetzt werden, um die Schallausbreitung zur Quelle zurück zu berechnen. Viele der Techniken, die bereits heute bei kontaktlose Messungen angewendet werden, basieren auf der bekannten Formulierung des Kirchhoff Helmholtz Integrals. Dazu gehören beispielsweise die "Wave superposition method" (WSM), die "Helmholtz least squares method" (HELS), die "Inverse boundary method" (IBEM) oder die fourierbasierte planare Nahfeldholografie.

All diese Ansätze tendieren zu schlechter numerischer Konditionierung und werden üblicherweise mit Hilfe der ℓ_2-Norm invertiert. Der Umgang mit räumlichen Aliasing, numerischer Instabilität und Fehlern, die aufgrund der begrenzten Messapertur entstehen, sind in der Literatur ausgiebig beschrieben. Die schlechte Lokalisierung dünn besetzter Lösungen bei Anwendung der oben genannten Methoden wurde bisher jedoch noch nicht ausreichend diskutiert. In dieser Arbeit sollen die Eigenschaften einer ℓ_1-optimierten Nahfeldholografie untersucht und die deutlich verbesserte Lokalisation von Punktquellen im Gegensatz zu den bekannten ℓ_2- optimierten Lösungen aufgezeigt werden. Dafür wurden Messimulationen und reale Messungen an unterschiedlichen Quelltypen durchgeführt, um das Verhalten dieser neuen Optimierung aufzuzeigen.

Leider lässt sich eine wahrhafte Dankbarkeit
mit Worten nicht ausdrücken.

Johann Wolfgang von Goethe

ACKNOWLEDGMENTS

Foremost, I would like to show my deepest gratitude to my supervisor Dr. Franz Zotter, whose exceptional competence and inspiration guided me through this work.

It is also a pleasure for me to thank the IEM staff, especially my roommates on the first floor, for creating such a enjoyable working atmosphere. I also convey thanks to Dr. Karoly Jalics of the Virtual Vehicle who provided the volume acceleration source used for the measurements.

Furthermore, I want to thank my fellow students, especially Antonio Hölzl, Michael Tauch, Fabio Kaiser and all the other friends for studying, discussing and having such a wonderful time together for the last seven years. I hope we stay in touch!

I wish to thank my girlfriend Bernadette for her marvelous support in every sense and for being such a special person in my life.

Finally, I am truly indebted and thankful to my family, especially to my parents, for their constant and unconditional support, their love and belief in me. Thank you so much!

CONTENTS

1 INTRODUCTION

1.1 INTRODUCTION

Acoustic measurements provide useful tools to analyze the properties of a vibrating structure by measuring its emission. In this scope, holography promises contact-free measurements in the sound field to observe the vibration on the structural source plane. Therefore, it has become a major factor in the optimization and design process for acoustic emissions of structures.

In the past 30 years, several holographic techniques were introduced which aim at the calculation of acoustic quantities in space and on the vibrating structure [1]. On the one hand, Maynard and Williams introduced the *Fourier-based nearfield acoustical holography (NAH)* [2], which utilizes the benefits of spatial Fourier transform to calculate the structural velocity . Several variations and hybrid techniques such as the *Statistically optimized near-field acoustical holography (SONAH)* [3], the *Wave superposition method (WSM)* [4] or the *Least-squares method (LSM)* [5] enrich the toolkits of acoustic holography today.

On the other hand, the sound field can be evaluated numerically by *Boundary element methods*, for which the basic derivation for acoustical purposes is given by Veronesi and Maynard [6].

1.2 MOTIVATION

Improvements in signal processing and regularization techniques led to today's holography systems that yield results robust to measurement noise and enable sound field analysis in real-time.

Nevertheless, there is still a lot of potential for improvements. One is the application of holography to a sparsely distributed structural vibration. Existing systems usually underestimate point-like velocity distributions in amplitude and show uncertainties for their localization as illustrated in figure 1.1. In the recent advancements, ideas emerged in the field of compressive sensing of how to optimize linear equation systems in terms of sparse solutions.

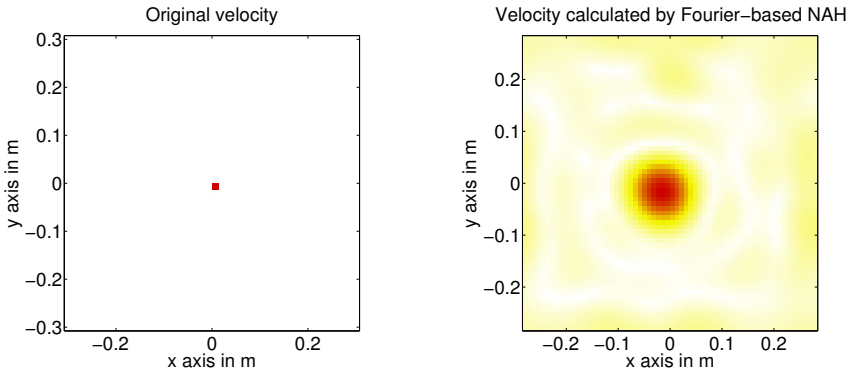

(a) Original velocity at 300Hz (b) Calculated velocity at 300Hz

Figure 1.1: Poor reconstruction of a sparsely distributed structural vibration, measured by an 8×8 microphone array at a distance $a = 0.05m$

1.3 OBJECTIVE

The objective of this work is to apply the sparse optimization techniques of compressive sensing on several simulation studies and some practical examples to show their benefits.

In particular, sparse optimization is suitable to overcome the location problems of the known holography approaches in terms of well-localized structural vibration.

2

PLANAR ACOUSTIC HOLOGRAPHY

In the upcoming section, a general formulation of acoustic holography based on Rayleigh integrals is derived. Some important relations are explained which are crucial to understand the assumptions made. For a comprehensive explanation of the general basics in acoustics, the reader is referred to the manifold standard literature such as [7] and [8].

2.1 BASICS

2.1.1 *Euler equation*

We know from Newton's law that the force **F** in a direction x is caused by the mass m and the acceleration a_x of a body:

$$F_x = m \cdot a_x = m \cdot \frac{\partial v_x}{\partial t} = \rho_0 \partial x \partial y \partial z \cdot \frac{\partial v_x}{\partial t} \, .$$

The force **F** at the location x is equivalent to a pressure change:

$$\begin{aligned} F_x &= [p(x) - p(x + \Delta x)] \cdot \Delta y \Delta z \\ &= \frac{[p(x) - p(x + \Delta x)]}{\Delta x} \cdot \Delta x \Delta y \Delta z \\ &= -\frac{\partial p}{\partial x} \cdot \partial x \partial y \partial z \, . \end{aligned}$$

Both expressions combined yield the *Euler equation*:

$$\nabla p = -\rho_0 \frac{\partial \mathbf{v}}{\partial t} \, . \tag{2.1}$$

This equation relates the sound particle velocity $\mathbf{v}$ to the sound pressure p. In the frequency domain, the expression becomes:

$$\nabla p = -j\omega\rho_0 \mathbf{v} \tag{2.2}$$

2.1.2 *The homogeneous wave equation*

Using Euler's equation (eq. 2.1), the continuity equation $\frac{\partial \rho}{\partial t} = -\nabla(\rho_0 \mathbf{v})$ and the formulation for the adiabatic compression equation $\nabla(p) = c^2 \nabla(\rho)$, we can derive the *homogeneous wave equation* for the sound pressure p:

$$\Delta p - \frac{1}{c^2} \cdot \frac{\partial^2 p}{\partial t^2} = 0 \, . \tag{2.3}$$

A detailed derivation, is found in the textbooks on acoustics. The equivalent equation in the frequency domain is known as the *Helmholtz equation*:

$$\Delta p + k^2 p = 0 \, . \tag{2.4}$$

2.1.3 *The inhomogeneous wave equation*

By adding a differential mass $\frac{\partial m}{\partial t}$ to the *law of mass conservation*

$$\frac{\partial \rho}{\partial t} - \nabla (\rho_0 \mathbf{v}) = 0 \, ,$$

we obtain:

$$\frac{\partial \rho}{\partial t} - \nabla (\rho \mathbf{v}) = \frac{\partial m_{src}}{\partial t} \delta(\mathbf{r} - \mathbf{r_0}) \, . \tag{2.5}$$

This equation addresses the continuous addition and subtraction of mass from a source in the volume at r_0. By differentiation of *Euler's equation* with regard to time and of eq. 2.5 with regard to space and involving the compression equation, the wave equation becomes:

$$\nabla^2 p - \frac{1}{c^2} \frac{\partial^2 p}{\partial t^2} = -\frac{\partial^2 m}{\partial t^2} \cdot \delta(\mathbf{r} - \mathbf{r_0}) = -\rho_0 \frac{\partial q_{src}}{\partial t} \cdot \delta(\mathbf{r} - \mathbf{r_0}) \, . \tag{2.6}$$

This is called *inhomogenious Helmholtz equation* in the frequency domain:

$$\nabla^2 p(\mathbf{r}) + k^2 p(\mathbf{r}) = -j\omega \rho_0 q_{src}(\mathbf{r}) \tag{2.7}$$

The right-hand side of the equation is equivalent to a point monopole source. The inhomogeneous Helmholtz equation is solved by the Green's function.

2.1.4 *The Free Space Green's Function*

The free space Green's function is the response of the wave equation to a pulse excitation. It is the spatial *transfer function* of a point monopole source. The question is, how this function can be derived from eq. 2.7?

We can regard a point monopole source as a breathing sphere of radius a that oscillates at a frequency ω. The relation of the radial displacement $\zeta(t)$ to its derivative, the velocity $v(t)$, is:

$$\zeta(t) = \hat{\zeta} e^{j\omega t} = \int v(t) dt \, , \qquad \text{with } \hat{\zeta} \ll a \, .$$

In the frequency domain this is

$$\frac{v}{j\omega} = \zeta \, .$$

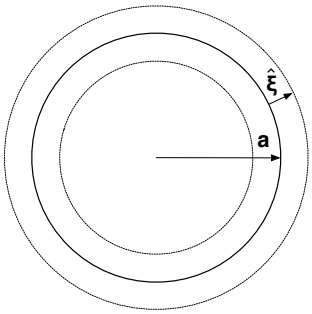

Figure 2.1: Pulsating monopole

Using Euler's equation $v_r = \frac{j}{\omega\rho}\frac{\partial p}{\partial r}$, we obtain:

$$\hat{\zeta} = \frac{1}{\omega^2\rho}\left(\frac{\partial \hat{p}(r)}{\partial r}\right)\Bigg|_{r=a} .$$

Furthermore, the radial sound pressure of a monopole is known from Fahy [7]:

$$\hat{p}(r) = \left(\frac{\hat{A}}{r}\right) e^{-jkr} , \tag{2.8}$$

where k is known as *wavenumber* ($k = \frac{\omega}{c}$) and $\hat{A}$ corresponds to the maximum pressure amplitude.

This leads to a description of the displacement that solely depends on parameters of the source and the medium:

$$\begin{aligned} \Rightarrow \hat{\zeta} &= \frac{1}{\omega^2\rho}\left(-\frac{\hat{A}}{r^2}e^{-jkr} - \frac{\hat{A}}{r}jke^{-jkr}\right)\Bigg|_{r=a} \\ &= -\frac{\hat{A}}{\omega^2 a^2\rho}\left(1+jka\right)e^{-jka} . \end{aligned}$$

Resolving the equation for the maximum pressure amplitude $\hat{A}$ and inserting it into eq. 2.8 yields an expression for the sound pressure at r:

$$\begin{aligned} \hat{p}(r) &= -\hat{\zeta}\left(\frac{\rho ck\omega a^2}{(1+jka)r}\right)e^{jka}e^{-jkr} \\ &= -\hat{\zeta}\left(\frac{\rho\omega c(ka)\frac{a}{r}}{1+jka}\right)e^{-jk(r-a)} . \end{aligned}$$

Insertion of the source volume velocity

$$Q(t) = \hat{Q}e^{jwt} = \left[\left(jw\hat{\zeta}\right)\left(4\pi a^2\right)\right]e^{jwt} , \tag{2.9}$$

yields:

$$\hat{p}(r) = -\left(\frac{\omega\rho\hat{Q}}{j4\pi r}\right)\cdot\left(\frac{1}{1+jka}\right)e^{-jk(r-a)} .$$

To obtain an ideal monopole source, the radius of the pulsating sphere is made vanishingly small:

$$\begin{aligned} \text{with } a \to 0 \quad &: \qquad ka \ll 1 \\ \Rightarrow \quad \hat{p}(r) \quad &\approx \quad \left(\frac{j\omega\rho\hat{Q}}{4\pi r} \right) e^{-jkr} \, . \end{aligned} \tag{2.10}$$

The numerator can be interpreted as the strength of a monopole which we set to 1. The expression now describes the sound pressure per unit source strength of a harmonic point monopole [7]. This formulation is also known as the *harmonic free space Green's function*, which solves eq. 2.7:

$$G = \frac{e^{-jkr}}{4\pi r} \, . \tag{2.11}$$

2.1.5 *The Kirchhoff Helmholtz Integral*

Huygen's principle assumes that the sound field consists of superimposed elementary waves. This principle is mathematically described by the Kirchhoff Helmholtz Integral (KHI) either for radiation or interior problems. In order to derive an expression for the planar acoustic holography based on Rayleigh integrals, we take a closer look at the *Kirchhoff Helmholtz Integral for radiation problems*. After considering a very general view on vector fields, we apply this knowledge to our concrete problem [13].

First, we consider figure 2.2, where a volume Ω encloses a monopole source at $\mathbf{r}'$ and the observation point lies outside this volume at $\mathbf{r}$.

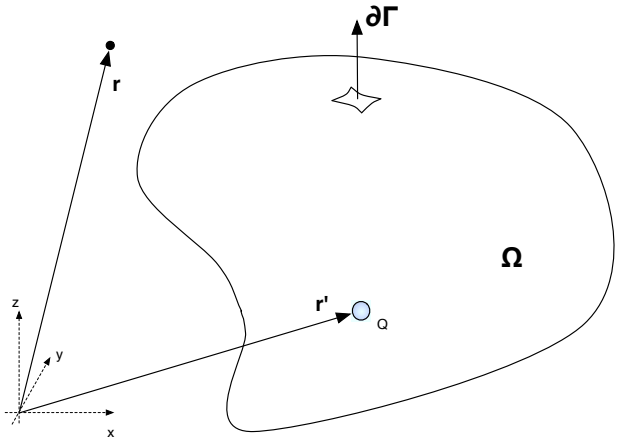

Figure 2.2: Point source surrounded by a sphere

The *divergence theorem* states that the integral over a vector field **F** bounded

by the surface Γ equals to the strength of the sources inherent in its volume Ω[1].

$$\oint_\Gamma \mathbf{F} d\Gamma = \int_\Omega \nabla \mathbf{F} d\Omega \, . \tag{2.12}$$

The vector field $\mathbf{F}$ can be replaced by a combination of two scalar fields p and G which fulfill the homogeneous and the inhomogeneous Helmholtz equation, respectively,

$$\mathbf{F} = G(\mathbf{r}|\mathbf{r}')\nabla p(\mathbf{r}) - p(\mathbf{r})\nabla G(\mathbf{r}|\mathbf{r}') \, , \tag{2.13}$$

which is true for[2]

$$\begin{aligned} \nabla^2 p(\mathbf{r}') + k^2 p(\mathbf{r}') &= 0 \\ \nabla^2 p(\mathbf{r}') &= -k^2 p(\mathbf{r}') \end{aligned} \tag{2.14}$$

$$\begin{aligned} \nabla^2 G(\mathbf{r}|\mathbf{r}') + k^2 G(\mathbf{r}|\mathbf{r}') &= -\delta(\mathbf{r}' - \mathbf{r}) \\ \nabla^2 G(\mathbf{r}|\mathbf{r}') &= -k^2 G(\mathbf{r}|\mathbf{r}') - \delta(\mathbf{r}' - \mathbf{r}) \, . \end{aligned} \tag{2.15}$$

The divergence theorem applied on $\mathbf{F}$ simplifies upon insertion of eq. 2.14 and 2.15:

$$\begin{aligned} \oint_\Gamma G\nabla p - p\nabla G d\Gamma &= \int_\Omega \nabla^{\mathbf{T}} \big(G\nabla p - p\nabla G\big) d\Omega \\ &= \int_\Omega \big(\nabla^{\mathbf{T}} G\nabla p + G\nabla^{\mathbf{T}}\nabla p - \nabla^{\mathbf{T}} p\nabla G - p\nabla^{\mathbf{T}}\nabla G\big) d\Omega \\ &= \int_\Omega \Big(G\nabla^2 p - p\nabla^2 G\Big) \, d\Omega \\ &= \int_\Omega \Big(-k^2 Gp + k^2 pG + p\delta(\mathbf{r} - \mathbf{r}')\Big) \, d\Omega \, . \end{aligned} \tag{2.16}$$

This KHI for radiation problems remains:

$$C_e \cdot p(\mathbf{r}) = \oint_\Gamma \left(G(\mathbf{r}|\mathbf{r}') \frac{\partial}{\partial \mathbf{n}} p(\mathbf{r}') - p(\mathbf{r}') \frac{\partial}{\partial \mathbf{n}} G(\mathbf{r}|\mathbf{r}') \right) d\mathbf{r}' \, . \tag{2.17}$$

The position of the observation point $\mathbf{r}$ defines the constant C_e according to

$$C_e = \begin{cases} 1, & \mathbf{r} \text{ outside } \Omega, \\ \frac{1}{2}, & \mathbf{r} \text{ on } \Gamma, \\ 0, & \mathbf{r} \text{ inside } \Omega. \end{cases}$$

---

1 The use of the nabla operator ∇ on a scalar yields its gradient:
$\nabla g = \left[\frac{\partial}{\partial x}\mathbf{e_x}, \frac{\partial}{\partial y}\mathbf{e_y}, \frac{\partial}{\partial z}\mathbf{e_z}\right]^{\mathsf{T}} \cdot g = \frac{\partial g}{\partial x}\mathbf{e_x} + \frac{\partial g}{\partial y}\mathbf{e_y} + \frac{\partial g}{\partial z}\mathbf{e_z}$

The use of the nabla operator ∇ on a vector yields its divergence:
$\nabla \mathbf{g} = \left[\frac{\partial}{\partial x}\mathbf{e_x}, \frac{\partial}{\partial y}\mathbf{e_y}, \frac{\partial}{\partial z}\mathbf{e_z}\right] \cdot \left[\mathbf{g_x}, \mathbf{g_y}, \mathbf{g_z}\right]^{\mathsf{T}} = \frac{\partial \mathbf{g_x}}{\partial x} + \frac{\partial \mathbf{g_y}}{\partial y} + \frac{\partial \mathbf{g_z}}{\partial z}$

2 ∇^2 is calculated as follows:
$\nabla^2 = \nabla \cdot \nabla = \left[\frac{\partial}{\partial x}\mathbf{e_x}, \frac{\partial}{\partial y}\mathbf{e_y}, \frac{\partial}{\partial z}\mathbf{e_z}\right]^{\mathsf{T}} \cdot \left[\frac{\partial}{\partial x}\mathbf{e_x}, \frac{\partial}{\partial y}\mathbf{e_y}, \frac{\partial}{\partial z}\mathbf{e_z}\right] = \frac{\partial^2}{\partial x^2} + \frac{\partial^2}{\partial y^2} + \frac{\partial^2}{\partial z^2}$

The KHI as written above is only helpful for observation points on the surface of the volume or outside, as it vanishes otherwise. If the point resides on the surface plane Γ, only the half-sphere outside the volume is considered [11].

The first term is composed of the Green's function and the gradient of the sound pressure. In chapter 2.1.4 we already derived the meaning of $G(\mathbf{r}|\mathbf{r}')$ as the transfer function of a monopole point source situated at $\mathbf{r}'$ and evaluated at $\mathbf{r}$. The gradient of the sound pressure $\frac{\partial}{\partial \mathbf{n}} p(\mathbf{r}')$ is a proportional to the sound particle velocity of the source as known from Euler's equation (eq. 2.1). The second term of the KHI consists of the gradient of the Green's function $\frac{\partial}{\partial \mathbf{n}} G(\mathbf{r}|\mathbf{r}')$ which corresponds to a dipole source aligned with the surface normal $\mathbf{n}$. This source is simply comprised of two monopole sources, one of which oscillates with inverted phase. This dipole is weighted by the sound pressure $p(\mathbf{r}')$. Here, the KHI is able to represent any sources inside the volume Ω by monopole and dipole sources on the surrounding boundary Γ, weighted either by the sound velocity or the sound pressure on this surface, respectively.

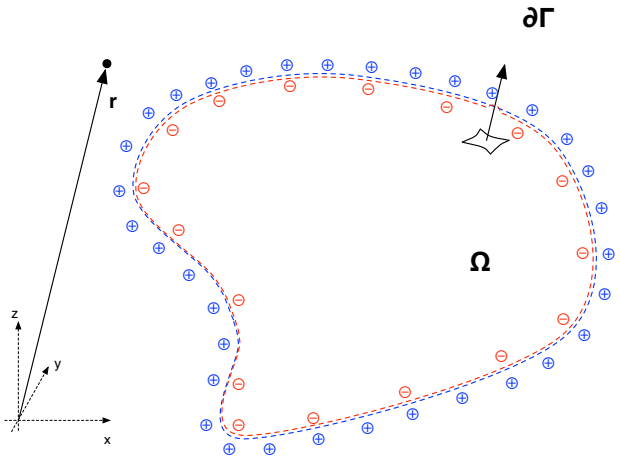

Figure 2.3: Representation of a vibrating body by the KHI

Accordingly, any inhomogeneous radiating sound field, also one of a vibrating body, can be fully represented in terms of the KHI. In any case, the vibrating structure or source field inside the volume Ω is replaced by a single and double source density layer at its boundary Γ equivalently to represent the radiating field (see figure 2.3).

The KHI is very general which means that it considers any 3-dimensional contours. For planar nearfield acoustic holography, simplifications of the KHI are possible yielding the so called *Rayleigh integrals*.

2.1.6 *Rayleigh integrals*

Instead of a finite body with a volume bounded by a surface, we are now extending this volume Ω to infinity and only consider the infinite surface plane generated in the a two-dimensional domain (cf. figure 2.4). The circular surface integral of the KHI thereby changes to a surface integral from $-\infty$ to $+\infty$ [13]:

$$p(\mathbf{r}) = -\int\int_{-\infty}^{+\infty} \left(G(\mathbf{r}|\mathbf{r}') \frac{\partial}{\partial z} p(\mathbf{r}') - p(\mathbf{r}') \frac{\partial}{\partial z} G(\mathbf{r}|\mathbf{r}') \right) dx dy \, . \tag{2.18}$$

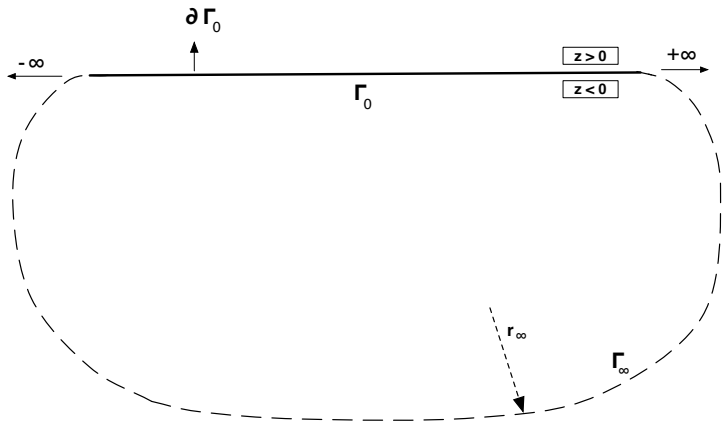

Figure 2.4: Extension of the KHI to infinity to evaluate a plane. The coordinate system is changed so that the surface normal is parallel to the z-axis at $z = 0$

With this formulation, we can still calculate the contributions of the sound field in front (for $z > 0$) as well as the field behind ($z < 0$) the plane surface. If we are just interested in the sound field of the positive z-plane, we can simplify the KHI.

If the velocity on the plane Γ_0 is forced to become zero, the condition corresponding to a rigid wall is called *Neumann condition*:

$$\left. \frac{\partial G_N}{\partial \mathbf{n}} \right|_{z=0} = 0 \tag{2.19}$$

To exploit this condition, we place a monopole source in front of this rigid boundary and evaluate its effect on an arbitrary point $\mathbf{r}$ above the source plane at $z = a$. Utilizing the image source principle [15], the incident field at the evaluation point is composed of the original source field $E(\mathbf{r}|\mathbf{r_m})$ at $z = a$ and a mirrored source component $F(\mathbf{r}|\mathbf{r'_m})$ at $z = -a$ (cf. figure 2.5) and becomes:

$$G_N(\mathbf{r}|\mathbf{r_m}) = E(\mathbf{r}|\mathbf{r_m}) + F(\mathbf{r}|\mathbf{r'_m}) \, . \tag{2.20}$$

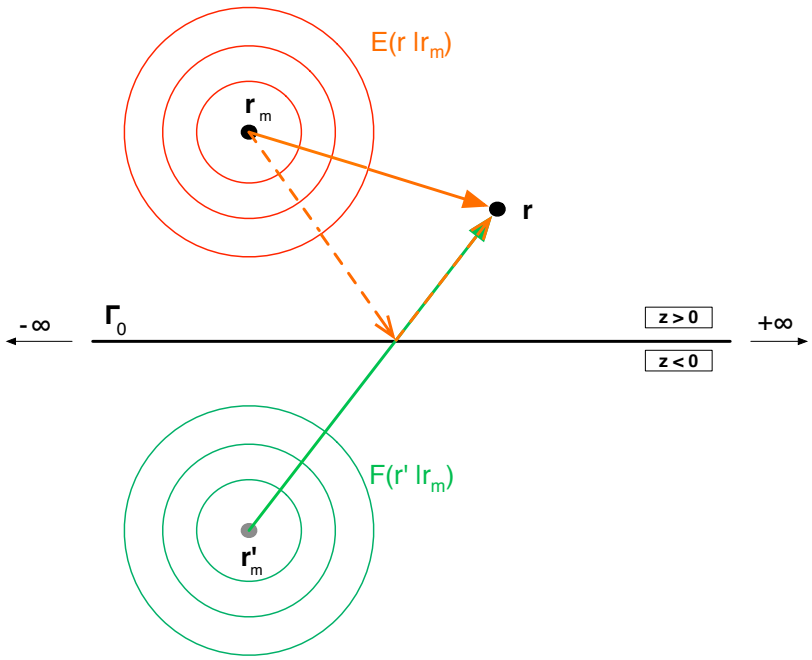

Figure 2.5: Image source principle

Before insertion into eq. 2.18, we need to derive both fields with respect to z. The derivatives of the field components are:

$$E(\mathbf{r}|\mathbf{r_m}) = \frac{e^{-jk(\mathbf{r}-\mathbf{r_m})}}{(\mathbf{r}-\mathbf{r_m})} \quad \Rightarrow \quad \frac{\partial E}{\partial z} = \frac{\partial}{\partial z}\left(\frac{e^{-jk(\mathbf{r}-\mathbf{r_m})}}{(\mathbf{r}-\mathbf{r_m})}\right),$$

$$F(\mathbf{r}|\mathbf{r'_m}) = \frac{e^{-jk(\mathbf{r}-\mathbf{r'_m})}}{(\mathbf{r}-\mathbf{r'_m})} \quad \Rightarrow \quad \frac{\partial F}{\partial z} = -\frac{\partial}{\partial z}\left(\frac{e^{-jk(\mathbf{r}-\mathbf{r'_m})}}{(\mathbf{r}-\mathbf{r'_m})}\right)$$

and yield a description of the pressure $p(r)$ in terms of both, original and image field:

$$\begin{aligned} p(\mathbf{r}) &= -\int\int_{-\infty}^{+\infty}\left(\left[E(\mathbf{r}|\mathbf{r_m})+F(\mathbf{r}|\mathbf{r'_m})\right]\frac{\partial}{\partial z}p(\mathbf{r_m}) - p(\mathbf{r_m})\frac{\partial}{\partial z}\left[E(\mathbf{r}|\mathbf{r_m})+F(\mathbf{r}|\mathbf{r'_m})\right]\right)dxdy \\ &= -\int\int_{-\infty}^{+\infty}\left(\frac{e^{-jk(\mathbf{r}-\mathbf{r_m})}}{(\mathbf{r}-\mathbf{r_m})}+\frac{e^{-jk(\mathbf{r}-\mathbf{r_m})}}{(\mathbf{r}-\mathbf{r_m})}\right)\frac{\partial}{\partial z}p(\mathbf{r_m})\,. \end{aligned} \tag{2.21}$$

Obviously, the dipole components vanish and a simple formulation of the sound pressure at $\mathbf{r}$ remains. One can still consider an infinitely thin layer lying in between the pair of sources with a pressure of zero. The potential $\frac{\partial}{\partial z}p$ of the integral lets us specify an additional component of the gradient specifying the vibration pattern of the rigid boundary (cf. figure 2.5 and 2.5). To describe the wavefield of a rigid vibrating plane, the pair of sources is positioned very close together so that they are practically coincide. Ap-

plying Euler's equation and evaluating this equation at any point $\mathbf{r}$ in the positive half space yields the *Rayleigh I Integral*

$$p(\mathbf{r}) = 2j\omega\rho \int\int_{-\infty}^{+\infty} G(x-x', y-y', z) v_n(x', y', 0)\, dx dy \; . \tag{2.22}$$

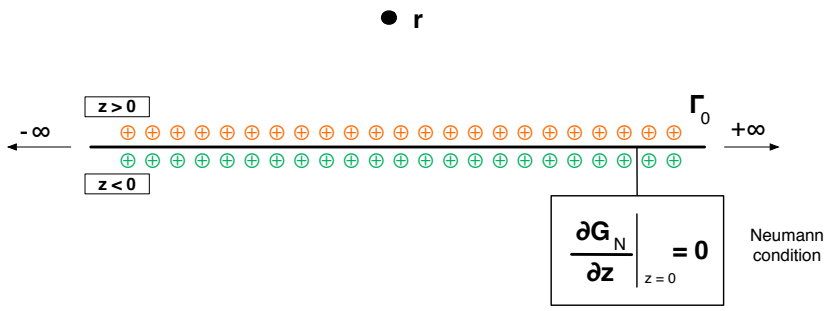

Figure 2.6: Mirrored monopole source layer over Neumann boundary

Alternatively assuming a pressure release boundary instead of a rigid wall, the so called *Dirichlet condition* holds:

$$G_D = 0 \; . \tag{2.23}$$

Again, the image source principle offers an elegant solution, this time with a mirrored dipole source layer such that their fields fulfill the condition:

$$G_D(\mathbf{r}|\mathbf{r_m}) = E(\mathbf{r}|\mathbf{r_m}) + F(\mathbf{r}|\mathbf{r'_m}) = 0 \; . \tag{2.24}$$

After derivation and insertion this combined field into eq. 2.18 the relation becomes:

$$\begin{aligned} p(\mathbf{r}) &= -\int\int_{-\infty}^{+\infty} \left(\left[E(\mathbf{r}|\mathbf{r_m}) + F(\mathbf{r}|\mathbf{r'_m}) \right] \frac{\partial}{\partial z} p(\mathbf{r_m}) - p(\mathbf{r_m}) \frac{\partial}{\partial z} \left[E(\mathbf{r}|\mathbf{r_m}) + F(\mathbf{r}|\mathbf{r'_m}) \right] \right) dx dy \\ &= -\int\int_{-\infty}^{+\infty} p(\mathbf{r_m}) \frac{\partial}{\partial z} \left(\frac{e^{-jk(\mathbf{r}-\mathbf{r_m})}}{(\mathbf{r}-\mathbf{r_m})} + \frac{e^{-jk(\mathbf{r}-\mathbf{r_m})}}{(\mathbf{r}-\mathbf{r_m})} \right) \; . \end{aligned} \tag{2.25}$$

Utilizing Euler's equation gives us the *Rayleigh II Integral* which describes a source layer of dipoles and its mirrored counterpart that are situated infinitely close to the Dirichlet boundary. These are weighted by the sound pressure distribution:

$$p(\mathbf{r}) = 2 \int\int_{-\infty}^{+\infty} p(x', y', 0) \frac{\partial}{\partial z} G(x-x', y-y', z)\, dx dy \; . \tag{2.26}$$

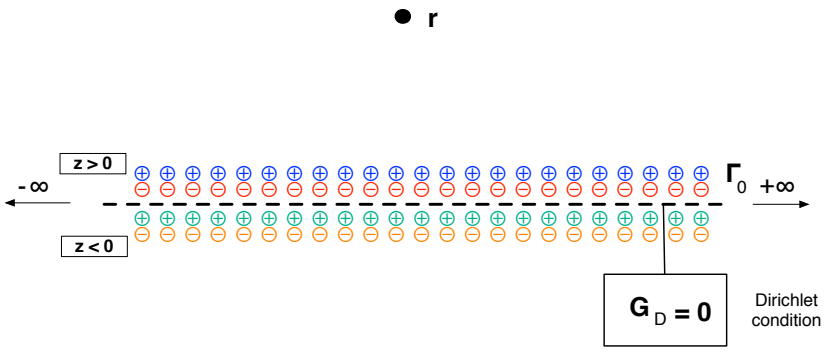

Figure 2.7: Mirrored dipole source layer below Dirichlet boundary

2.2 A DESCRIPTION OF PLANAR ACOUSTIC HOLOGRAPHY BASED ON RAYLEIGH INTEGRALS

The main goal of planar acoustic holography (PAH) is the determination of the sound velocity on the source plane from sound pressure measurements performed above the source plane.

From the Rayleigh integrals, which are simple and general, we easily obtain a compact description of planar acoustic holography. A common setup is shown in figure 2.8, where the sound pressure is measured on a planar grid parallel to the source plane at $z = a$. With the help of the free space Green's function and its derivative, either the sound velocity or sound pressure can be calculated on the source plane at $z = 0$. It is possible to determine the sound pressure in the field at any distance from the structure if the field is freefield.

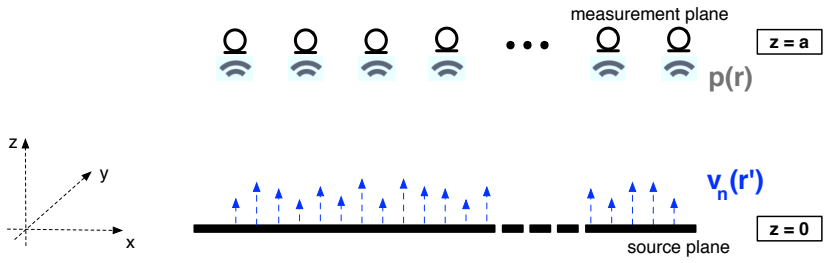

Figure 2.8: Measurement setup for planar acoustic holography

2.2.1 *Formulation*

We use the original formulation of the Rayleigh integral and calculate the sound pressure at a specific point $\mathbf{r}$ above the measurement surface ($z > 0$).

For this, the integral of eq. 2.22 needs to be discretized at a sufficiently high sampling rate that the following approximation is valid:

$$p(\mathbf{r}) \approx 2j\omega\rho \sum_{i=-\infty}^{+\infty} \sum_{j=-\infty}^{+\infty} G(x - x'_i, y - y'_j, z) v_n(x'_i, y'_j, 0) \Delta x_i \Delta y_i \, . \tag{2.27}$$

In real-world applications, the size of the measuring aperture is usually finite. Therefore, the patch of the source plane we are interested in is discretized in K steps in the x-direction and L steps in the y-direction. This leads to a truncation of the measurement plane:

$$p(\mathbf{r}) \approx 2j\omega\rho \sum_{i=0}^{K} \sum_{j=0}^{L} G(x - x'_i, y - y'_j, z) v_n(x'_i, y'_j, 0) \Delta x_i \Delta y_i \, . \tag{2.28}$$

It is important to keep in mind that the Rayleigh I integral still considers the velocity outside this patch to be zero despite of the truncation. The effect of this truncation is further addressed in chapter 2.2.4 .

All $N = K \times L$ values of the Green's function can be written into one vector $\mathbf{G_r}^T = [G(r|r'_1), G(r|r'_2), \ldots, G(r|r'_N)]^T$ and the associated velocity components into another vector $\mathbf{v} = [v(r'_1), v(r'_2), \cdots, v(r'_N)]$. With this, the discretized Rayleigh I integral becomes:

$$p(\mathbf{r}) = 2j\omega\rho \cdot \mathbf{G_r}^T \mathbf{v} \, . \tag{2.29}$$

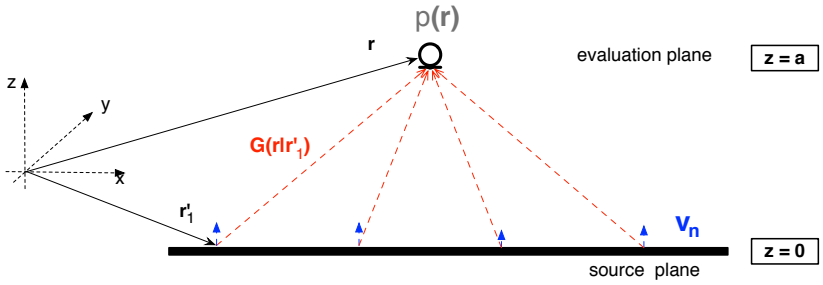

Figure 2.9: Calculation of the sound propagation

Up to now, we only calculated one single point above the plane. However, using linear algebra it is also possible to calculate the sound pressure at more than one point. For this, we consider an additional vector $\mathbf{p} = [p(r_1), p(r_2), \cdots, p(r_M)]$, containing M sound pressure components on a measurement plane at $z = a$. This alters the vector of the Green's

functions into a *circulant matrix* of size $M \times N$, comprised of the Green's function from each source velocity to the M evaluation points:

$$\mathbf{G} = \begin{pmatrix} \mathbf{G_{r_1}}^T \\ \mathbf{G_{r_2}}^T \\ \cdot \\ \cdot \\ \cdot \\ \mathbf{G_{r_M}}^T \end{pmatrix} = \begin{pmatrix} G(r_1|r'_1) & G(r_1|r'_2) & \cdots & G(r_1|r'_N) \\ G(r_2|r'_1) & G(r_2|r'_2) & \cdots & G(r_2|r'_N) \\ \cdot & \cdot & \cdots & \cdot \\ \cdot & \cdot & \cdots & \cdot \\ \cdot & \cdot & \cdots & \cdot \\ G(r_M|r'_1) & G(r_M|r'_2) & \cdots & G(r_M|r'_N) \end{pmatrix} .$$

This setup is illustrated in figure 2.10 for a simple setup with $N = M = 4$. With the derivations above, eq. 2.29 becomes

$$\mathbf{p} = 2j\omega\rho \cdot \mathbf{G}\mathbf{v} \, . \tag{2.30}$$

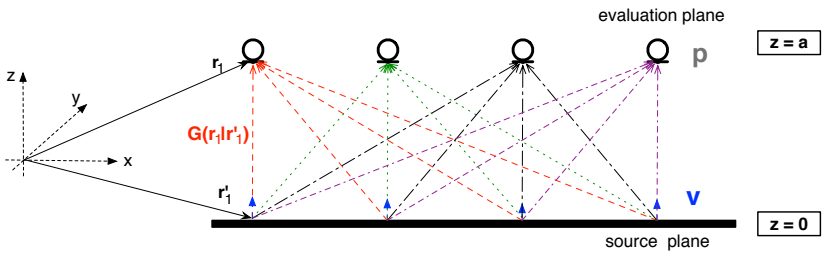

Figure 2.10: Calculation of sound propagation for $N = M$

Considering M microphone positions and $N = M$ velocity positions, eq. 2.30 is a fully determined system of equations and allows for a unique solution of the inverse problem:

$$\mathbf{v} = \frac{1}{2j\omega\rho} \mathbf{G}^{-1}\mathbf{p} \tag{2.31}$$

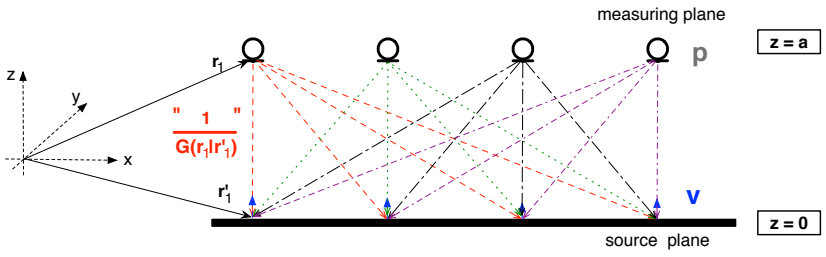

Figure 2.11: Planar acoustic holography for $N = M$

Figure 2.11 illustrates such a configuration and also reveals its drawbacks.

If we want to simulate the velocity on the source plane at a satisfactory resolution, an impractically number of microphones has to be used. Because of this, we need to reformulate the problem into an underdetermined equation system, where the number of of measuring points M is significantly lower than the number of calculated sources N:

$$\mathbf{v}_N = \frac{1}{2j\omega\rho} \left(\mathbf{G}_{M\times N}\right)^{\dagger} \mathbf{p}_M \tag{2.32}$$

The system is also depicted in figure 2.12 and ways to increase the resolution under different assumptions are given in the following chapters.

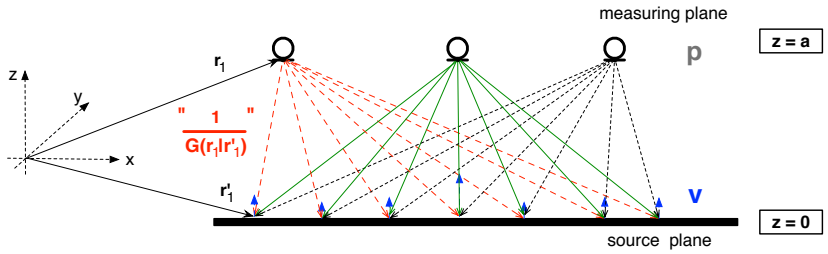

Figure 2.12: Planar acoustic holography for $N \neq M$

2.2.2 *Analysis of the inverse problem*

To solve the problem of eq. 2.32, we need to invert the matrix $\mathbf{G}$, describing the the transfer functions from source to sensor position.

For the *exactly determined problem* ($M = N$), it is known from linear algebra that we can calculate the inverse of a square matrix of $\mathbf{G}$ by finding matrix $\mathbf{H}$ that yields:

$$\mathbf{G} \cdot \mathbf{H} = \mathbf{I} = \mathbf{H} \cdot \mathbf{G} \,,$$

where $\mathbf{I}$ denotes the identity matrix. If this equation is fulfilled, we call matrix $\mathbf{H}$ the inverse of $\mathbf{G}$. This can also be written as $\mathbf{G}^{-1}$. If the matrix is regular, the inverse exist and can be numerically computed. If, on the other hand, the matrix is close to singular, we need to utilize regularization techniques. The following equation illustrates an exactly determined problem, where the number of measurement points M equals the number of parameters to calculate N:

$$\underbrace{\begin{pmatrix} * & * & * \\ * & * & * \\ * & * & * \end{pmatrix}}_{\mathbf{G}_{M\times N}} \cdot \underbrace{\begin{pmatrix} * \\ * \\ * \end{pmatrix}}_{\mathbf{v}_N} = \underbrace{\begin{pmatrix} * \\ * \\ * \end{pmatrix}}_{\mathbf{p}_M}$$

If plenty of measurements are available but only few points shall be calculated on the source plane, a system can be described as *overdetermined*. For equation 2.32, this would mean $M > N$:

$$\underbrace{\begin{pmatrix} * & * & * \\ * & * & * \\ * & * & * \\ * & * & * \\ * & * & * \end{pmatrix}}_{\mathbf{G}_{M\times N}} \cdot \underbrace{\begin{pmatrix} * \\ * \\ * \end{pmatrix}}_{\mathbf{v}_N} = \underbrace{\begin{pmatrix} * \\ * \\ * \\ * \\ * \end{pmatrix}}_{\mathbf{p}_M}$$

A problem of overdetermined systems is that there are more equations than unknowns. To solve these systems, the squared error between a guess of the unknown variables $\mathbf{v}$ multiplied by the appropriate Green's functions $\mathbf{G}$ and the measurement data $\mathbf{p}$ is minimized[3]:

$$\|\mathbf{e}\|_2^2 = \|\mathbf{G}\mathbf{v} - \mathbf{p}\|_2^2 \;\rightarrow\; \min \;.$$

We will not regard this solution in detail because the systems that are found in PAH are usually *underdetermined*. This means that only a few measurements are available, but a lot of points on the source plane are desired ($N > M$):

$$\underbrace{\begin{pmatrix} * & * & * & * & * \\ * & * & * & * & * \\ * & * & * & * & * \end{pmatrix}}_{\mathbf{G}_{M\times N}} \cdot \underbrace{\begin{pmatrix} * \\ * \\ * \\ * \\ * \end{pmatrix}}_{\mathbf{v}_N} = \underbrace{\begin{pmatrix} * \\ * \\ * \end{pmatrix}}_{\mathbf{p}_M}$$

Underdetermined systems do not have a unique solution. They either yield an infinite number of solutions or not any. To solve this problem and to calculate the unknown velocity vector $\mathbf{v}$, we introduce a penalty function $J(\mathbf{v})$ that fulfills the following constraint:

$$\begin{aligned} &\min_{\mathbf{v}} \; J(\mathbf{v}) \\ &\text{subject to } \mathbf{G}\mathbf{v} \;=\; \mathbf{p} \end{aligned} \tag{2.33}$$

Due to simplicity, the scalar term $2j\omega\rho$ is included into the matrix of the Green's functions $\mathbf{G}$. For the penalty we choose

$$J(\mathbf{v}) = \|\mathbf{v}\|_2^2 \,,$$

3 The solution to this problem is known as the *least-squares solution* and was already proposed by Gauss in the 18th century

which is the squared ℓ_2 - norm. It minimizes the energy on the source plane by a least-squares optimization. Eq. 2.33 minimizes this norm under the constraint that the equation system is fulfilled. At this point it is also possible to use other approaches, e.g. the ℓ_1-norm, as a penalty function. For now, we are solving the least-squares problem by constructing the *Lagrangian function* $\mathcal{L}(\mathbf{v})$ using the Lagrangian multiplier γ:

$$\begin{aligned}\mathcal{L}(\mathbf{v}) &= \mathbf{v}^T\mathbf{v} + \boldsymbol{\gamma}^T(\mathbf{G}\mathbf{v} - \mathbf{p}) \\ &= \mathbf{v}^T\mathbf{v} + \left(\mathbf{p}^T - \mathbf{v}^T\mathbf{G}^T\right)\boldsymbol{\gamma}\,.\end{aligned}$$

To solve the minimizing problem, we have to derive the costfunction with regard to $\mathbf{v}$ and γ

$$\begin{aligned}\frac{\partial\mathcal{L}(\mathbf{v})}{\partial\mathbf{v}} = 2\mathbf{v} + \mathbf{G}^T\boldsymbol{\gamma} &= 0 \\ \mathbf{v}_{opt} &= -\mathbf{G}^T\frac{\boldsymbol{\gamma}}{2}\,, \qquad (2.34)\end{aligned}$$

$$\begin{aligned}\frac{\partial\mathcal{L}(\mathbf{v})}{\partial\boldsymbol{\gamma}} = \mathbf{G}\mathbf{v}_{opt} - \mathbf{p} &= 0 \\ \mathbf{G}\mathbf{v}_{opt} &= \mathbf{p}\,. \qquad (2.35)\end{aligned}$$

Replacing $\mathbf{v}_{opt}$ in eq. 2.35 with the expression calculated in eq. 2.34 yields γ_{opt}:

$$\boldsymbol{\gamma}_{opt} = 2\left(\mathbf{G}\mathbf{G}^T\right)^{-1}\mathbf{p}\,.$$

Inserted into eq. 2.34 it becomes:

$$\mathbf{v}_{opt} = \underbrace{\mathbf{G}^T\left(\mathbf{G}\mathbf{G}^T\right)^{-1}}_{\text{right-inverse}}\mathbf{p}\,. \qquad (2.36)$$

With this, the so called *pseudoinverse* of the matrix $\mathbf{G}$ is obtained which gives an optimal solution of the inverse problem in the least-squares sense. We should keep in mind that even this matrix inverse cannot be calculated if the matrix $\mathbf{G}$ is of deficient row-rank and therefore singular. In this case, a working solution is obtained by regularization that modifies the matrix so that a slightly different but regular problem is solved instead.

The *Singular Value Decomposition (SVD)* is used to calculate the pseudoinverse due to its potential to deal with possible singularities of the inversion problem. It is known from linear algebra that a rectangular matrix can be represented by two orthogonal and one diagonal matrices [18]:

$$\mathbf{G} = \mathbf{U}\mathbf{S}\mathbf{V}^H\,,$$

where

$\mathbf{G}$	matrix of dimension $M \times N$
$\mathbf{U}$	orthogonal matrix of dimension $M \times M$
$\mathbf{S}$	diagonal matrix of dimension $M \times N$
$\mathbf{V}$	orthogonal matrix of dimension $N \times N$

Furthermore the matrices $\mathbf{U}$ and $\mathbf{V}$ are unitary:

$$\mathbf{U}\mathbf{U}^{H} = \mathbf{U}^{H}\mathbf{U} = \mathbf{I}$$

$$\mathbf{V}\mathbf{V}^{H} = \mathbf{V}^{H}\mathbf{V} = \mathbf{I}$$

The columns of $\mathbf{U}$ are the orthogonal eigenvectors of $\mathbf{G}\mathbf{G}^{H}$ whereas the columns of $\mathbf{V}$ are orthogonal eigenvectors of $\mathbf{G}^{H}\mathbf{G}$. The elements of the diagonal in $\mathbf{S}$ are the square roots of the eigenvalues of $\mathbf{V}$ or $\mathbf{U}$ (which are the same), which are often arranged in increasing order. We can now use the formulation of the SVD to invert the matrix $\mathbf{G}$:

$$\mathbf{G}^{-1} = \left(\mathbf{U}\mathbf{S}\mathbf{V}^{H}\right)^{-1} = \mathbf{V}\mathbf{S}^{-1}\mathbf{U}^{H} \tag{2.37}$$

The above inverse takes the hermitian response of $\mathbf{V}$ and $\mathbf{U}$ and inverts the diagonal of $\mathbf{S}$, which is padded with zeros:

$$\mathbf{S}^{-1} = \underset{N\times M}{\operatorname{diag}}\left(\frac{1}{\sigma_1},\cdots,\frac{1}{\sigma_M}\right) = \begin{pmatrix} \frac{1}{\sigma_1} & 0 & 0 & \cdots & 0 & 0 \\ 0 & \frac{1}{\sigma_2} & 0 & \cdots & 0 & 0 \\ 0 & 0 & \frac{1}{\sigma_3} & \cdots & 0 & 0 \\ . & . & . & \cdots & . & . \\ . & . & . & \cdots & . & . \\ 0 & 0 & 0 & \cdots & \frac{1}{\sigma_{M-1}} & 0 \\ 0 & 0 & 0 & \cdots & 0 & \frac{1}{\sigma_M} \\ 0 & 0 & 0 & \cdots & 0 & 0 \\ . & . & . & \cdots & . & . \\ 0 & 0 & 0 & \cdots & 0 & 0 \end{pmatrix} \tag{2.38}$$

With eq. 2.37, the calculation of a high resolution normal surface velocity $\mathbf{v}$ by means of only few measurements is in principle feasible, as long as the singular are not too small or even zero. $\mathbf{G}$ is ill-conditioned in this case. To address this problem, we now want to try to find a physical explanation of the origin of this ill-posedness.

2.2.3 *Evanescent waves and the ill-posed problem*

The matrix $\mathbf{G}$ that inherits the Green's functions is ill-conditioned due to exponentially decaying surface waves that are called *evanescent waves* [20]. Before proposing solutions to this problem, we want to take a look at the physical causes of these short ranging waves.

The speed of sound c of a medium usually differs from that in the air. As a consequence, the wavelengths for air and solid media λ_b, λ_L are different at the same frequency. This is illustrated in figure 4.3a, where the surface wavelength of a steel plate of different thickness h and that of air are compared. There are regions where the wavelength of the structure λ_b is greater

than λ_L and vice versa. The frequency at which both are equal is called *coincidence frequency* f_c. Because of the smaller wavelength of the plate below f_c and a resulting bad impedance matching, an acoustical short circuit occurs as fig. 4.3b illustrates. This means that the acoustic energy flows from the crest of the waves to its bottom and is merely emitted into the air.

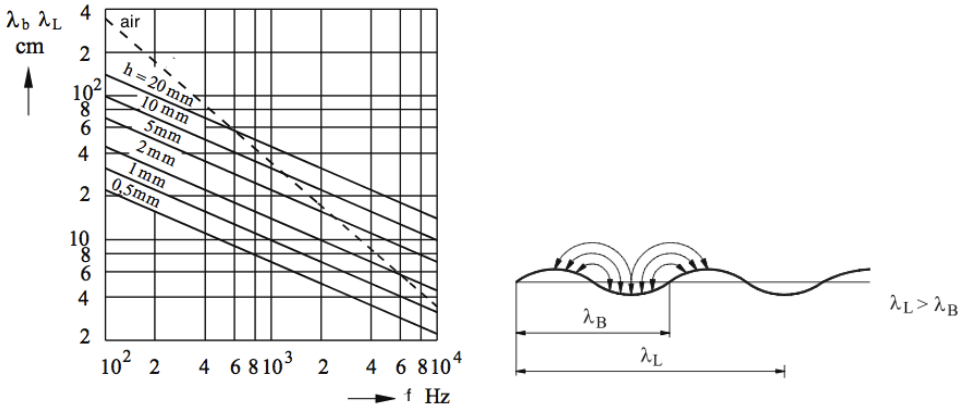

(a) Description of the wavelength in different media

(b) Acoustic short circuit due to bad impedance matching

Figure 2.13: Coincide frequency and the resulting evanescent waves (from [23])

Nevertheless the flowing energy still interacts with the air but rapidly vanishes with increasing distance to the structure. This results in exponentially decaying surface waves that are called *evanescent waves* (cf. figure 2.14).

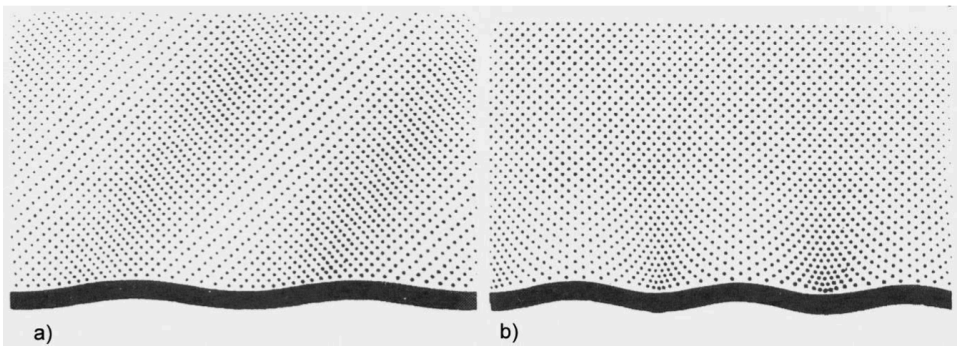

Figure 2.14: Propagation of plane waves (a) and evanescent waves (b) (from [24])

To calculate the true normal velocity of a structure by means of sound pressure measurements, the microphone array needs to capture these evanescent waves. Due to noise and a resulting limited *signal to noise ratio* of the measurement system, these waves can only be captured close to the source [4]. However, a measurement without these components will lead to serious problems in the reconstruction process. If the evanescent waves are important degrees of freedom, e.g. because the microphones are positioned close

4 Valdivia and Williams analyzed this problem and recommend to position the array at a distance between d and 2d from the source plane, when d equals to the microphone distance [25]

together for a regarded wavelength, the inversion of **G** is only possible, if the matrix is of full row-rank, i.e.:

$$\text{rank}\,(\mathbf{G}) \geqslant M \tag{2.39}$$

Measurements in the farfield do not contain the evanescent waves because only the plane waves can propagate far. This leads to a linear dependency of the rows of **G** and therefore to a reduction of its rank. Thus, the problem gets ill-posed as some singular values tend to zero. Inversion would boost the singular vectors associated with the small singular values of eq. 2.38 to infinity.

A good overview of regularization techniques to avoid this is given by Williams [21], Scholte [22], Sarkissian [20] and others. Most of these reports focus on NAH, but Sarkissian also describes a regularization technique that can explicitly be used for the theory presented above.

2.2.4 *Effects of discretized and truncated measurement aperture*

If the measurement aperture is discretized by a limited number of microphones, it causes different effects.

First of all, the *sampling theorem* must be fulfilled which means that the emitted wavelength needs to be sampled at a sufficiently narrow grid to avoid *spatial aliasing*. The theorem states that at least two microphones have to sample the wavelength λ_{min}. As for time and frequency, there also exists a relation between space and frequency. The propagating wavefield in space is described by the wavenumbers in the so called k-space. The relationship between frequency and wavenumber domain is illustrated in figure 2.15

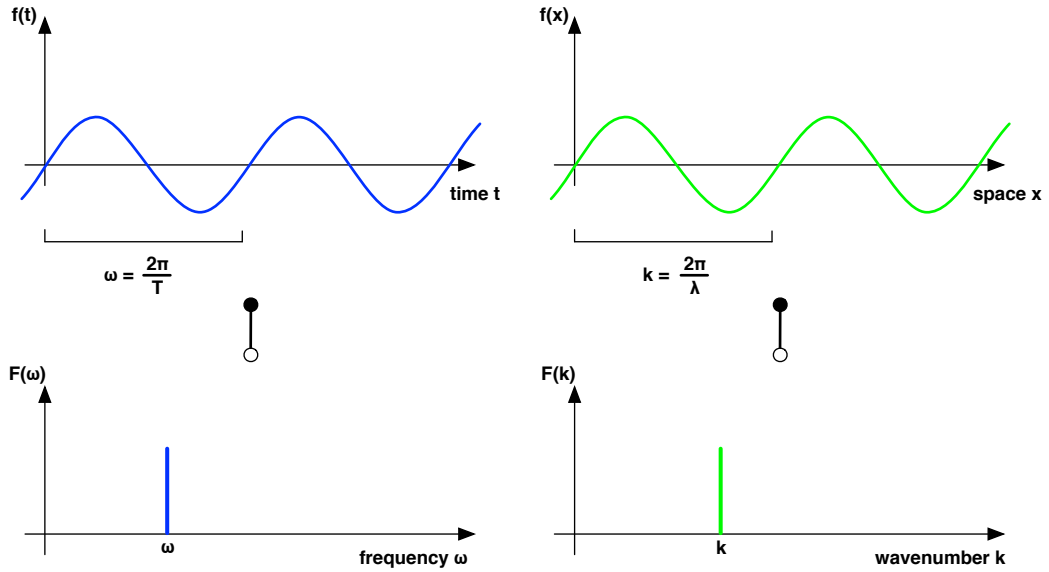

Figure 2.15: Transformations in time and space

The upper limit to avoid aliasing is defined by:

$$\begin{aligned} \lambda_{min} &= 2d\,, \\ k_{max} &= \frac{2\pi}{\lambda_{min}} = \frac{2\pi}{2d} = \frac{\pi}{d}\,. \end{aligned} \tag{2.40}$$

All components above this limit lead to misinterpretations of wavenumbers and therefore to alias components that occur in the spatial domain. Evanescent waves do not fulfill the upper wavenumber limit derived from plane waves.

The imposed wavenumber limit due to aliasing results in a rectangular truncation in k-space. From signal processing we know that the truncation of a signal in one domain may lead to artifacts in the corresponding domain. The application of a rectangular window in k-space therefore leads to a convolution of the signal with a sinc-function in the spatial domain.

Talking about truncation, we also have to consider the spatial rectangular window we apply by measuring with a finite number of microphones. This window in turn, will lead to sinc-function like artifacts in k-space (cf. figure 2.16)

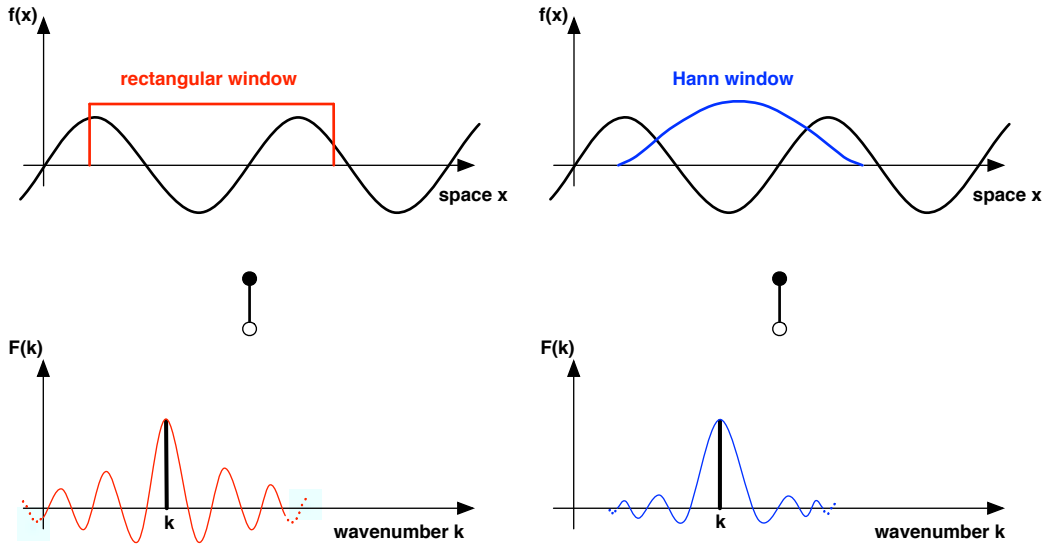

Figure 2.16: The effect of windowing

One way to deal with those artifacts, also known as spectral leakage, is the use of window-functions like the Hann-window. These functions ease the abrupt breakaway of the signal by implying a weight on the outmost signal components. This leads to improvements in the reconstruction, whereas the truncation in space seems to be of much less importance. However, we need to keep in mind that this windowing does not circumvent aliasing at all. To achieve this, we need to apply an anti-aliasing filter in k-space.

An elegant way to implement this is to use the lowpass properties of the Green's function described in the following chapter.

2.2.5 *Influence of the measurement distance* a

The preceding chapter discussed the corrupting effects of aliasing originating from a misinterpretation of the emitted soundfield due to a insufficient number of sensors per wavelength. In the nearfield of the source, evanescent waves of high wavenumbers exist (cf. chapter 2.2.3). To capture these components, the number of sensors must be increased. These evanescent waves are the reason for the supremacy of the nearfield acoustic holography to measure the velocity of a structure.

To avoid the potentially resulting artifacts of aliasing due to this wavenumbers, a lowpass filter has to be applied in k-space. It comes in handy that the Green's function, expressing the sound field propagation, has the characteristic of a resonant lowpass filter. Its cut-off wavenumber k_{co} is defined by the analyzed frequency f, whereas the slope is dependent on the distance of the aperture to the source. Figure 2.17 illustrate this for different measurement distances a. We can clearly see the steeper slope for a larger distance. With this in mind we can ensure the upper wavenumber limit given in eq. 2.40 by adjusting the distance of the measurement aperture to the source plane. Nevertheless, this only excludes the presence of potentially aliased sound field components for structures that are not excessively exciting evanescent normal velocity patterns.

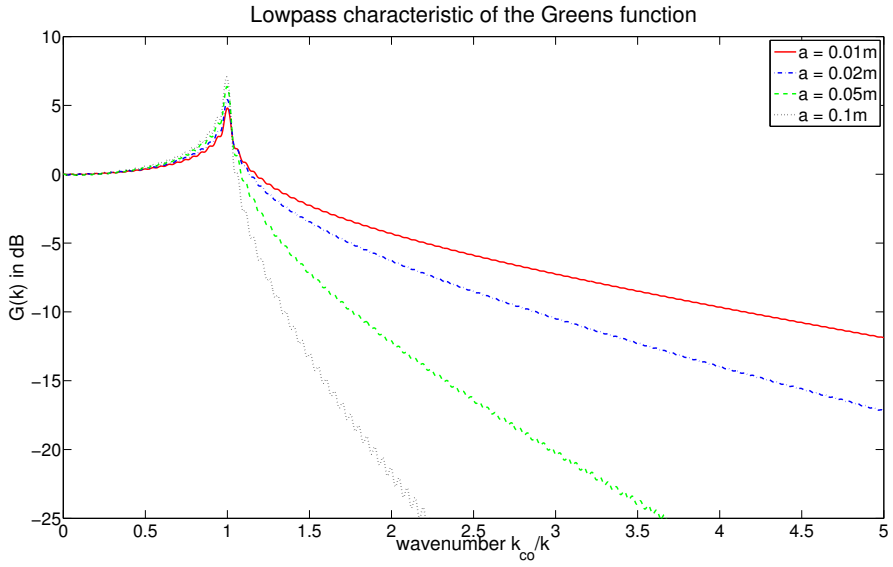

Figure 2.17: Lowpass characteristic of the Green's function

2.2.6 *A note on point sources*

In chapter 2.2.4, the sampling theorem was discussed thoroughly. This requirement is straightforward for modal vibrations whose material wavelength can easily be restricted by controlling the frequency range. However, it gets more complicated considering point sources on the source plane. Independent of the emitted frequency, the distance of the measurement aperture to the source layer has a crucial influence. High frequency components potentially violate the sampling theorem. The closer the array is positioned, the larger the spatial variation of the observed sound pressure will be. This effect is illustrated in figure 2.18

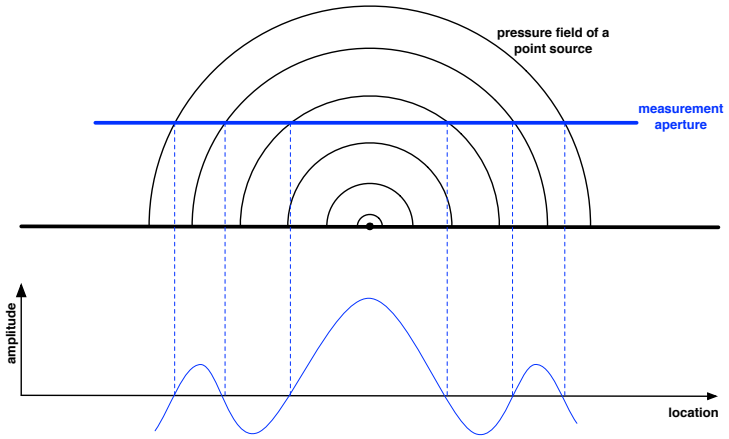

(a) Resulting spatial variation at a large measurement distance

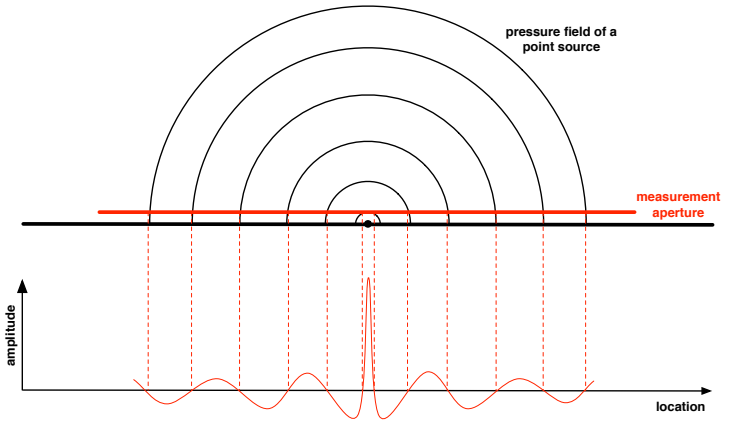

(b) Resulting spatial variation at a small measurement distance

Figure 2.18: Dependency of the spatial variation of the observed sound pressure on the distance: it becomes large for close distances

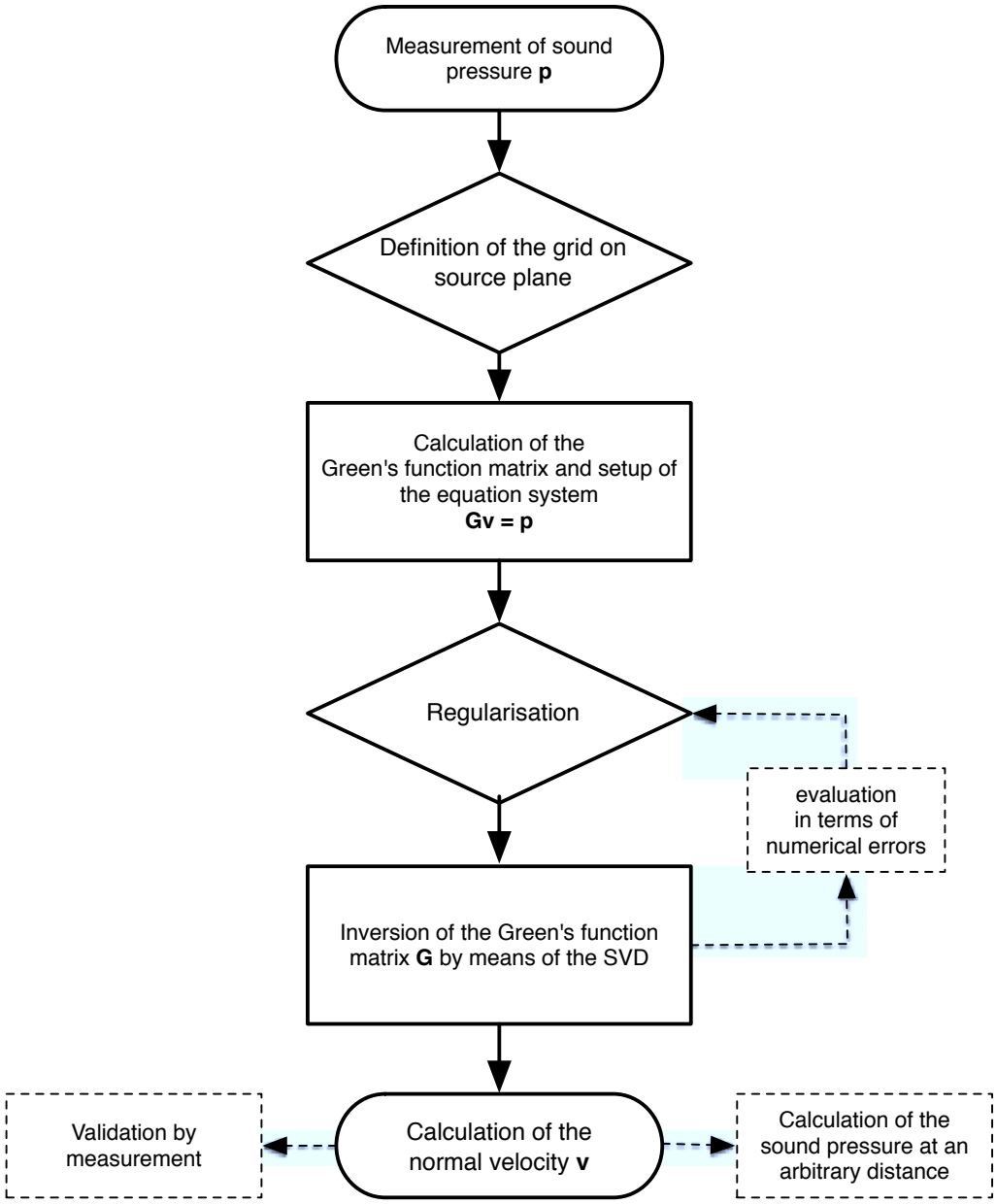

Figure 2.19: State graph of the planar acoustic holography

This section provides an overview of simulated results using PAH. We want to focus on two types of sources. The first one is a resonating plate with all edges clamped. The second setup consists of three point sources with different strength emitting from a plane surface. For both configurations, the propagation of the sound field is simulated and the measurement can be virtually performed at a desired distance with an arbitrary number of sensors. This thesis focus on rectangular measurement apertures with microphones placed at an equidistant grid. However, it is important to mention that the theory of PAH is neither limited to a rectangular measurement aperture, nor to equidistant grids.

2.3.1 *PAH solution for a vibrating plate example*

The propagation of a sound field excited by a resonating metal plate is simulated. The first analysis focus on the quality of the inversion of eq. 2.31 performed by means of the SVD. Therefore we consider an exactly determined system with equally many measurement points in the emitted field as discrete points on the source plane.

The frequency of the resonating plate is given by Möser [23]:

$$f_{res} = \frac{\pi}{2}\left[\left(\frac{n_x}{l_x}\right)^2 + \left(\frac{n_y}{l_y}\right)^2\right]\sqrt{\frac{B'}{m''}}\,,$$

and

$$B' = \frac{E}{1-\mu}\cdot\frac{h^3}{12}\,,$$

$$m'' = \rho_{steel}\cdot h\,,$$

where

h	thickness of vibrating plate $(0,001\,m)$
ρ_{steel}	density of steel $(7850\,\frac{kg}{m^3})$
E	Young's modulus of steel $(2,1\cdot 10^{11}\,\frac{N}{m^2})$
μ	Poisson's ratio $(0,3)$
l_x	length of plate in x-direction
l_y	length of plate in y-direction
n_x	order of the resonance in x-direction
n_y	order of the resonance in y-direction .

The vibrating plate of the dimension $0.4m \times 0.4m$ is discretized by 40×40 equidistant points. The resulting source velocity is shown in figure 2.20.

The propagating sound pressure field is simulated at four different recording distances (0.01m, 0.02m, 0.05m and 0.1m). Figure 2.21 gives an idea about the evolution of this field for an increasing distance to the source.

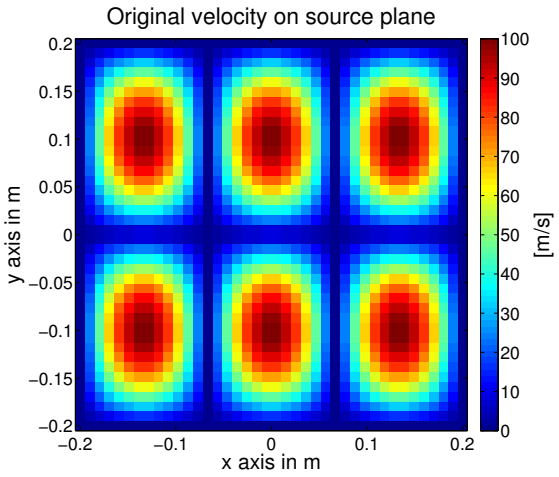

Figure 2.20: Normal velocity of a vibrating plate in a 2-3 mode

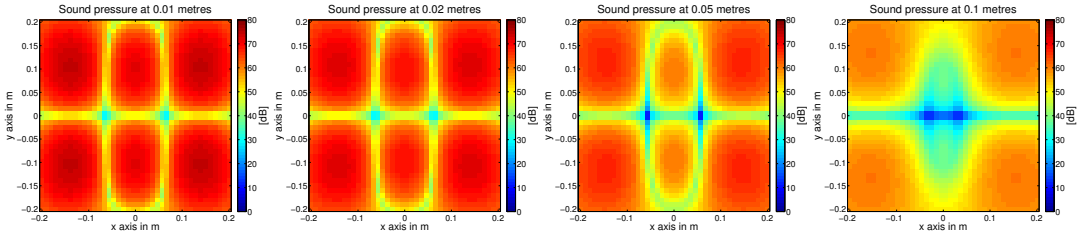

(a) $a = 0.01\text{m}$ (b) $a = 0.02\text{m}$ (c) $a = 0.05\text{m}$ (d) $a = 0.1\text{m}$

Figure 2.21: Evolution of the sound pressure field of a vibrating plate in a 2-3 mode

In the first example, the simulated measurement aperture is positioned at a distance of $a = 0.01\text{m}$ and the source velocity is calculated. As already mentioned, an exactly determined system is assumed for which the calculated normal velocity $\mathbf{v}$ and the error shown in figure 2.22. The solution at this distance yields an almost perfect result with a negligible misfit.

The distance of the measurement aperture is now increased to 0.02m. The result of the PAH and the errors in figure 2.23 is also close to perfect.

Another simulation is performed at $z = 0.05\text{m}$ and displayed in figure 2.24. Although the resonances of the plate are still recognizable, errors, which we would not expect in a perfectly determined system, occur. Recapitulating chapter 2.2.3 leads to the conclusion that these are caused by the ill-posedness due to evanescent waves that already vanish at this distance. The loss leads to linear dependencies in the equation system of eq. 2.31 and thus to a reduction of the rank of $\mathbf{G}$. The ill-posed problem has singular values that tend to zero, as observed. This leads to a boost in inverted results that cause numerical errors. To ease the ill-posedness, a simple regularization is used to alter the singular values to reasonably large numbers. We

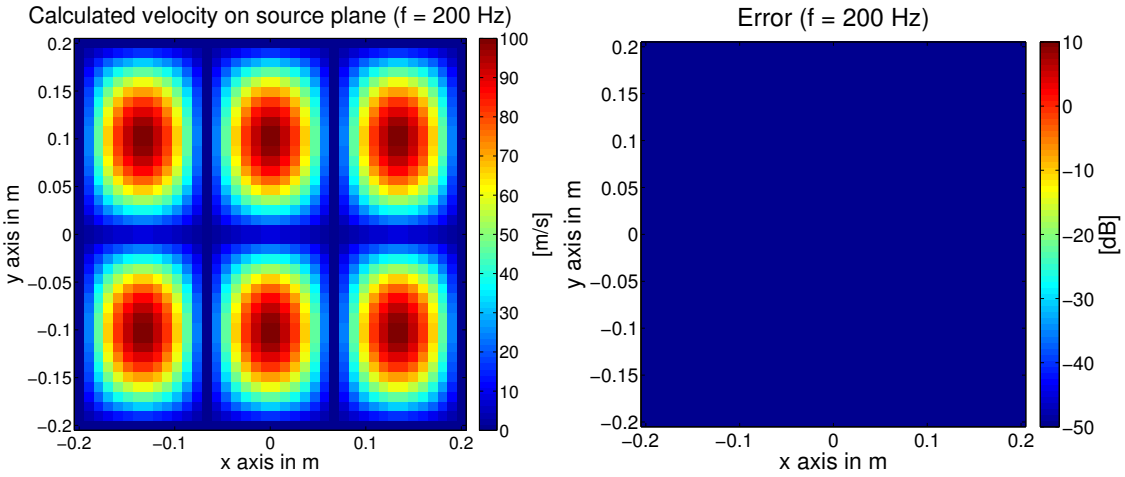

(a) Calculated velocity (b) Error in dB

Figure 2.22: PAH result at a distance of $a = 0.01m$

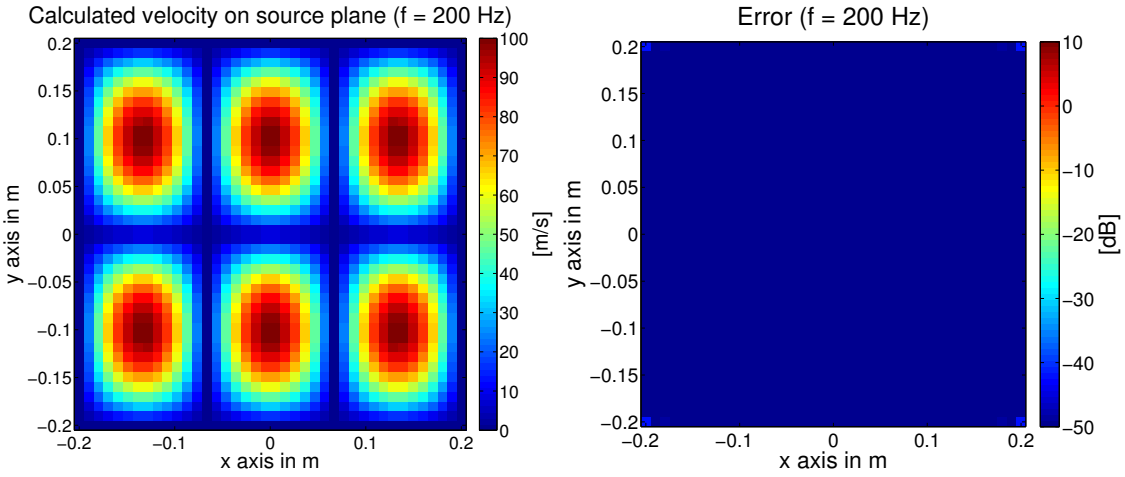

(a) Calculated normal velocity (b) Error in dB

Figure 2.23: PAH result at a distance of $a = 0.02m$

can do so by adding a small number r to the main diagonal of the matrix $\mathbf{S}$ of eq. 2.37 before inverting it:

$$\mathbf{S}^{-1} = \underset{N\times M}{\text{diag}}\left(\frac{1}{\sigma_1 + r}, \cdots, \frac{1}{\sigma_M + r}\right) . \tag{2.41}$$

It is convenient to define r in terms of a regularization parameter R in decibel and the maximum singular value σ_{max}:

$$r = \sigma_{max} \cdot 10^{\frac{R}{20}} . \tag{2.42}$$

The result of this regularization is displayed in figure 2.25. Table 2.1 reveals that the quality of the solution significantly increases.

With this simple regularization technique at our hand, we now try to double the distance of the measurement aperture and evaluate the results at

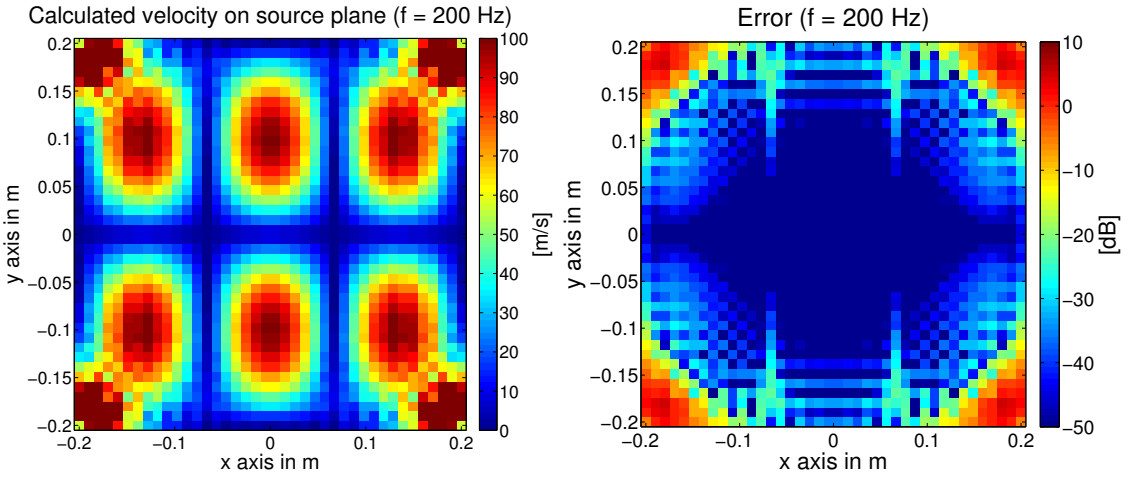

(a) Calculated normal velocity (b) Error in dB

Figure 2.24: PAH result at a distance of $a = 0.05m$ without regularization

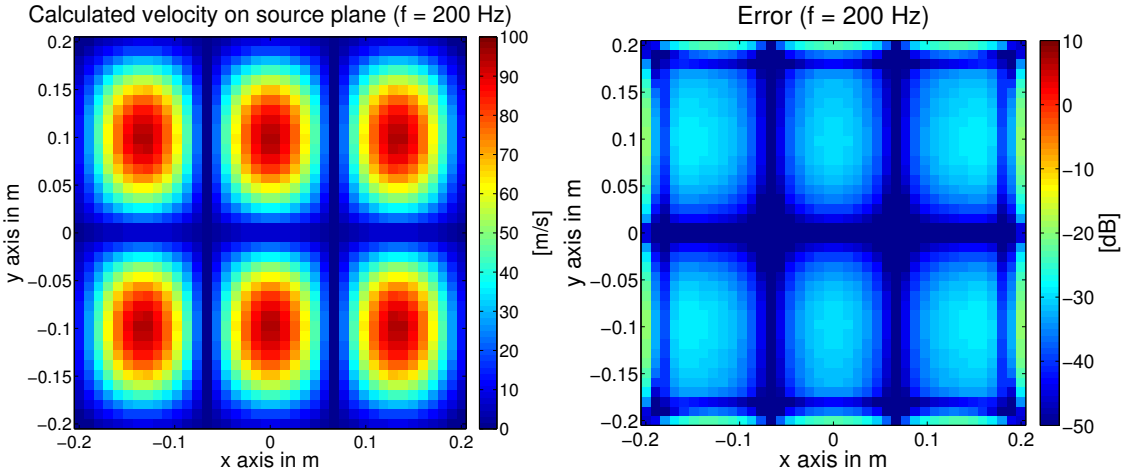

(a) Calculated normal velocity (b) Error in dB

Figure 2.25: PAH result at a distance of $a = 0.05m$ with $R = -50dB$

$a = 0.1m$. For the regularization parameter R set to $-50dB$, the surface waves of the structure are still observable although the error increases.
If the regularization parameter R is raised to $-45dB$, the result degenerates further which is illustrated in figure 2.27) and table 2.1. This table displays a single value error e which is explained in chapter 4. Using other regularization techniques proposed by Williams [21], Scholte [22], Sarkissian [20] and others it might offer a possibility to enhance the result even further. However, these approaches are not covered in this thesis.

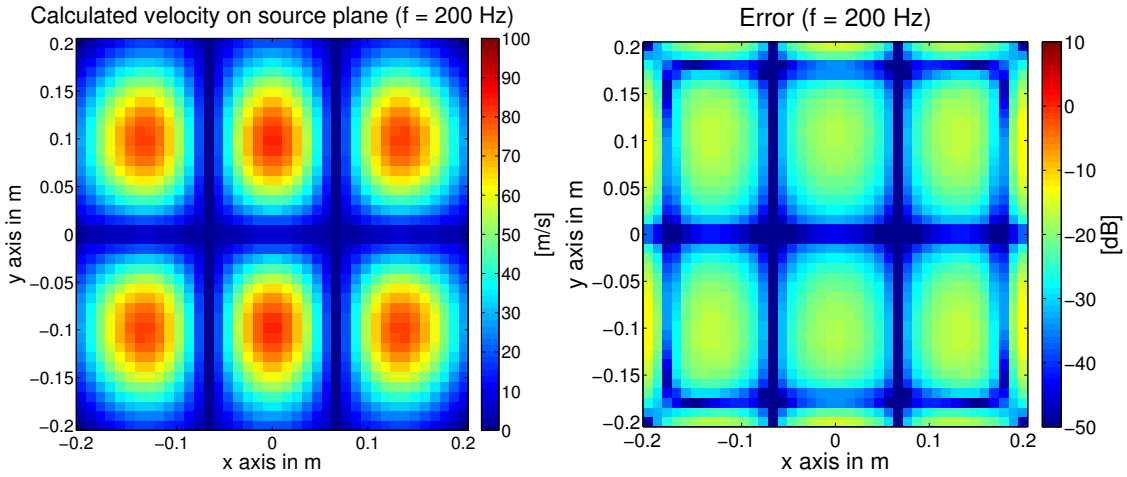

(a) Calculated normal velocity (b) Error in dB

Figure 2.26: PAH result at a distance of $a = 0.1m$ with $R = -50dB$

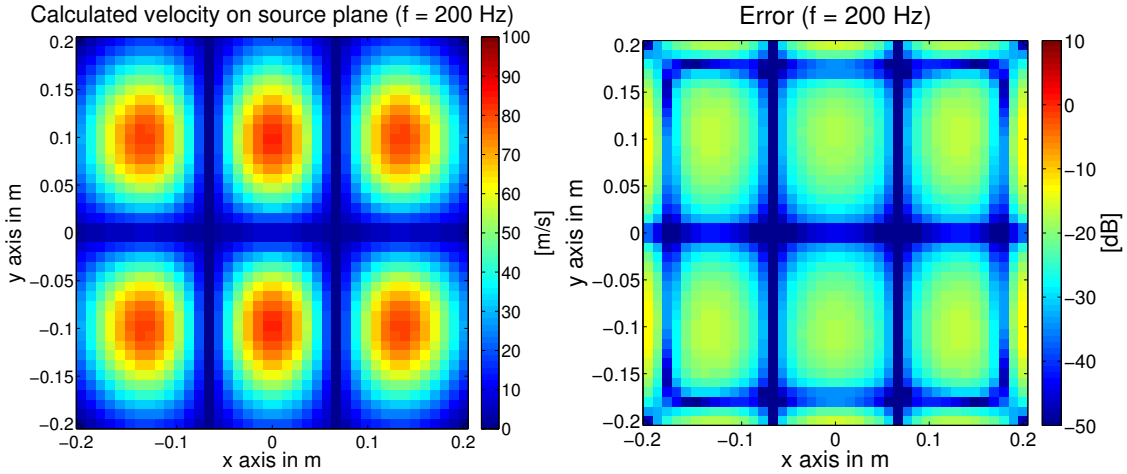

(a) Calculated normal velocity (b) Error in dB

Figure 2.27: PAH result at a distance of $a = 0.1m$ with $R = -45dB$

distance a in m	$a = 0.01$	$a = 0.02$	$a = 0.05$		$a = 0.1$	
	no reg.	no reg.	no reg.	$R = -50dB$	$R = -50dB$	$R = -45dB$
error e	**0.11**	**0.27**	**55.71**	**7.9**	**20.6**	**28.4**

Table 2.1: Single value error e

2.3.2 *PAH solution for a point source example*

This section describes the evaluation of point sources in terms of the Rayleigh-based PAH. A source layer consisting of three monopoles with different strength is created and the propagation of the resulting pressure field is simulated. Figure 2.28 displays the resulting field at 0.02m, evaluated at

three selected frequencies (300Hz, 1kHz, 3kHz). The plots show a significant decrease of sound pressure with increasing distance (around 10dB for 0.01m - 0.05m). At higher frequencies, interference occur in the propagation.

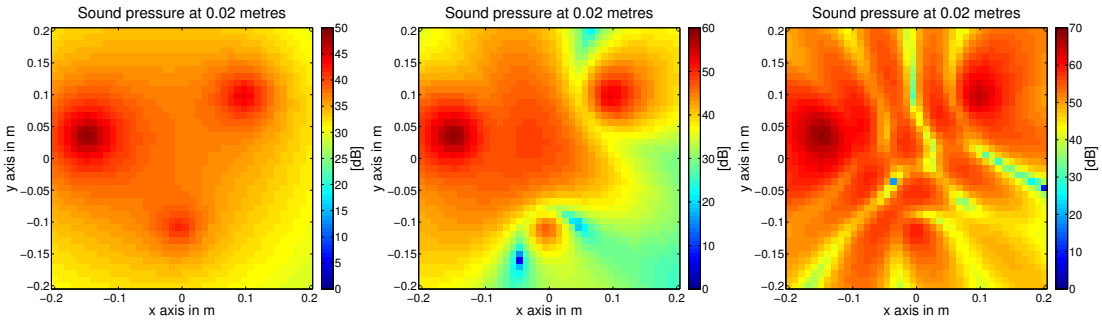

(a) $f = 300Hz$, $a = 0.02m$ (b) $f = 1kHz$, $a = 0.02m$ (c) $f = 3kHz$, $a = 0.02m$

Figure 2.28: Propagation of the sound pressure field of point sources for $f = 300Hz$, $f = 1kHz$ and $f = 3kHz$ at $0.02m$

In contrast to the other examples in chapter 2.3.1, the measurement grid is now fixed at a distance of $0.02m$. Again, we will start with a simulation of the exactly determined system to examine the best possible result. As we can see in figure 2.29, the equation system is solved perfectly, with no appreciable error to mention. For all further simulation examples, we consider a more realistic setup, where the number of microphones is small, to reduce cost and hardware complexity. Such an equation system will be underdetermined but still solvable as described before.

Three arrays are simulated with 15×15 (225), 8×8 (64) and 6×6 (36) microphones. All arrays cover the same size of $0.4m \times 0.4m$, resulting in microphone distances of $2.7cm$, $5cm$ and $6.7cm$ respectively. As already described in section 2.2.4, the sampling theorem and the distance of the measurement plane to the source has to be considered to avoid aliasing. Assuming the wavelength of a plane wave, the maximum frequencies for the given measurement grids are:

$$\begin{aligned} f_{max,15\times15} &= \frac{343\frac{m}{s}}{2 \cdot 0.027} = 6431Hz\,, \\ f_{max,8\times8} &= 3430Hz\,, \\ f_{max,6\times6} &= 2573Hz \end{aligned} \tag{2.43}$$

The results for a first analysis at 300Hz is displayed in figure. 2.30. Although the reduction of sensors to a 15×15 grid still leads to an acceptable localization of the sources (see fig. 2.30), the calculated velocity is significantly lower than of the original source (mind the axis of the velocity). Furthermore, we can encounter an excitation spread around the peak with a

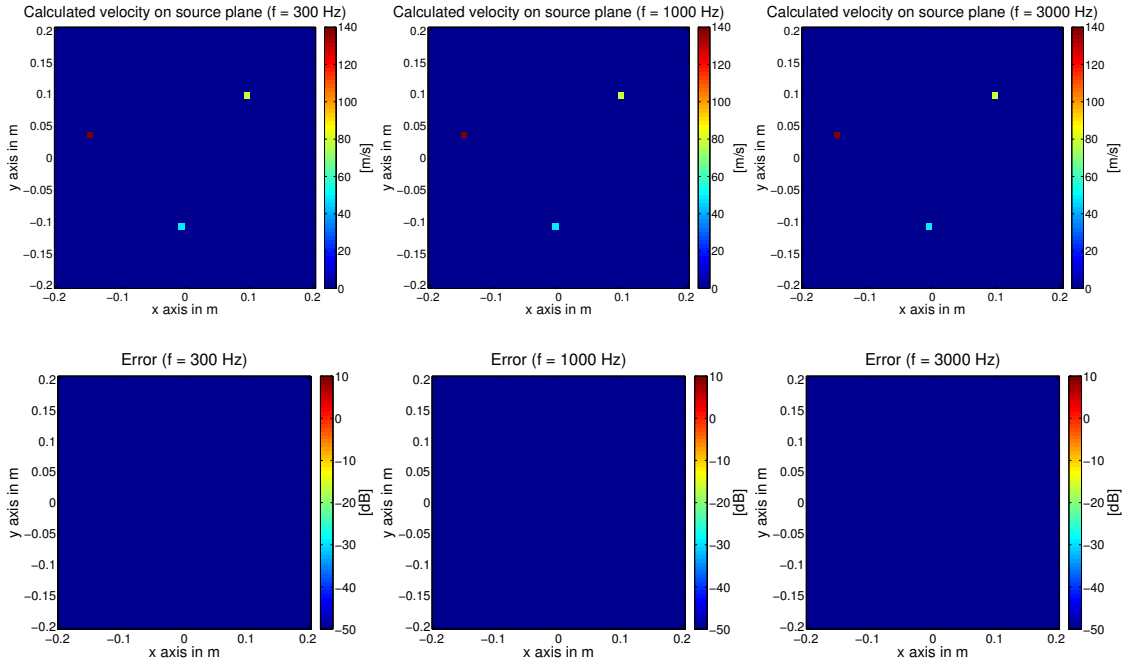

f = 300Hz f = 1kHz f = 3kHz

Figure 2.29: Calculated normal velocity (upper row) and equivalent error (lower row) at a measurement distance $a = 0.02m$ for the exactly determined case

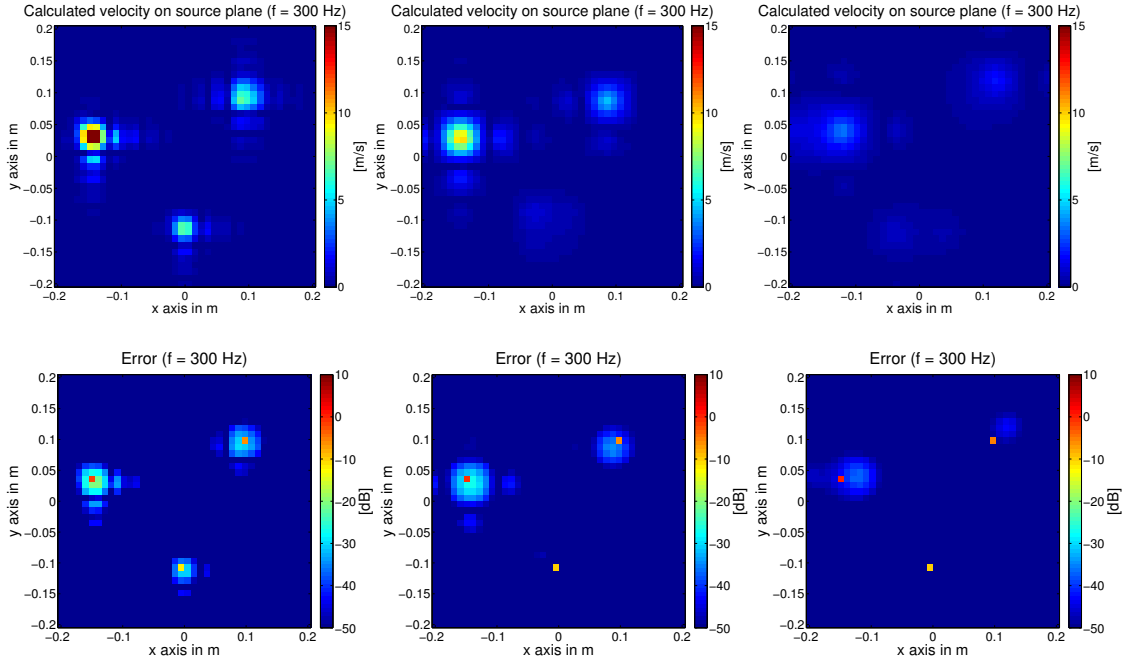

15×15 8×8 6×6

Figure 2.30: Calculated normal velocity (upper row) and equivalent error (lower row) for a measurement distance $a = 0.02m$ at $f = 300Hz$ with reduced sensor positions

characteristic shape. As described in chapter 2.2.4, this pattern is caused by the upper frequency limit, determined by the sampling theorem. It is interesting to see that aliasing already occurs, although in eq. 2.43 a sufficiently high frequency limit was derived. Obviously, the close source causes rapid vibrations (cf. section 2.2.6). A further reduction of microphones leads to an increase of these artifacts and to a further reduction of the calculated velocity. The source emitting the lowest energy can hardly be distinguished without prior knowledge. The simulation using the 6×6 measurement grid finally gives only a glimpse about the original position of the sources. The analysis for 1000Hz yields a similar result (figure 2.31).

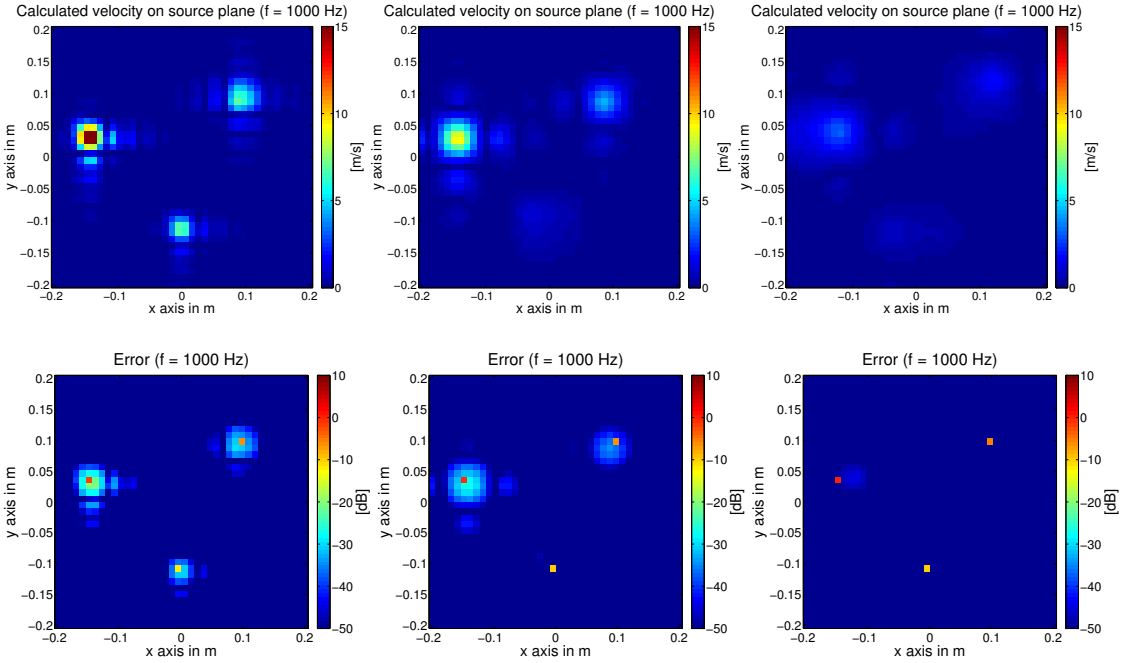

Figure 2.31: Calculated normal velocity (upper row) and equivalent error (lower row) for a measurement distance $a = 0.02m$ at $f = 1000Hz$ with reduced sensor positions

The analysis at 3000Hz degenerates even faster because more aliasing artifacts are introduced due to the higher analysis frequency (cf. figure 2.32). The least-squares optimization inherits the property to "smear" the energy and to align equal components. Therefore, the simulation grid for 6×6 microphones almost yields no recognizable solution. The results, which are also similar elsewhere in literature, motivate the investigation of potentially improved resolution which is carried out in this thesis.

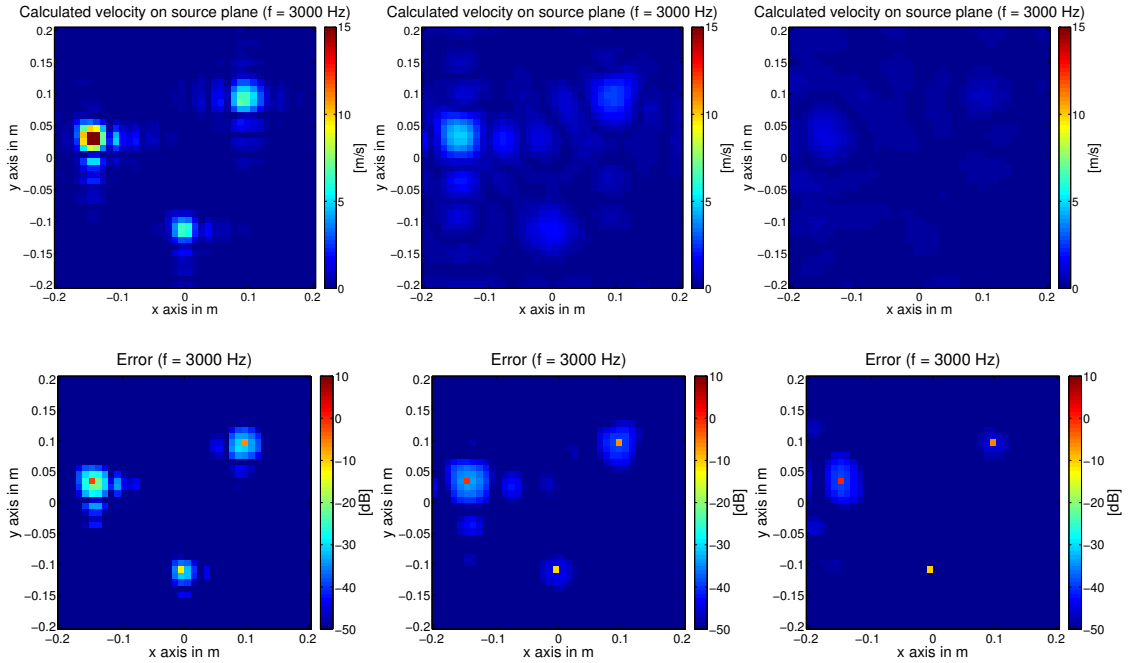

Figure 2.32: Calculated normal velocity (upper row) and equivalent error (lower row) for a measurement distance $a = 0.02m$ at $f = 3000Hz$ with reduced sensor positions

	40×40	15×15	8×8	6×6
300Hz	**0.2**	**93.7**	**97.2**	**99.4**
1000Hz	**0.5**	**93.7**	**97.3**	**99.5**
3000Hz	**1.8**	**93.7**	**98.2**	**99.0**

Table 2.2: Single value error e for the reduced system at distance $a = 0.02m$

2.4 SUMMARY

In this chapter, a solution to planar acoustic holography based on Rayleigh integrals was introduced. From the KHI, a description of a vibrating plate in terms of the Rayleigh I integral was derived. After the formulation as a linear equation system, the underdetermined system was reviewed, to head to a more realistic scenario. The underdetermined inverse problem was thoroughly analyzed and led to the assumption that the resulting equation system can be solved using a least-squares ansatz.

This theory was successfully examined using simulations for two distinct problems, a resonating plate and a point source problem. While the results of the resonating plate were very convincing, the performance for problems sparse in space were poor. The reason for this is the least-squares optimization of the inverse problem that smears the energy of point sources. In the

following chapter, a new formulation of the optimization problem is given to support this sparsity and to successfully apply the PAH also to this kind of problems.

3

SPARSE HOLOGRAPHIC IMAGING

The Rayleigh-based PAH in the previous chapter did not yield convincing results in terms of localization for problems with small and localized velocity patterns. This is mainly due to the property of the applied least-squares approach, which tend to spread the energy all over the solution vector.

However, in the past years, new ideas in optimization theory became apparent that could now be helpful, to solve this sparse problem[1]. In this chapter, the techniques to enforce good results to sparse problems are examined and the formulation for PAH is extended.

3.1 SPARSE SOLUTIONS OF UNDERDETERMINED SYSTEMS

In chapter 2, an underdetermined linear equation system was derived to solve the planar acoustic holography .

$$\mathbf{G}_{M\times N}\,\mathbf{v}_N = \mathbf{p}_M \tag{3.1}$$

Usually, the number of available microphones is much lower than the number of desired points on the source plane ($M \ll N$). Such a system leads to an infinite number of solutions. In 2.33, we calculated the valid solution by minimizing the ℓ_2-norm as a penalty function. The reason for this choice was simplicity, as the solution is unique and easily determined by the right-inverse. The question arises, if there exist an alternative. We first analyze the properties of the ℓ_2-norm to see its benefits, but also what its drawbacks are.

3.1.1 *Convexity*

The reason for the unique ℓ_2-solution lies in the fact that it corresponds to a strictly convex function, meaning that its solution converges to a global minimum. To understand this property, a convex vector-set is defined and expanded to a description of convex functions. A mathematical problem can only called convex if the set of variables and all applied functions are convex [27].

Therefore, the vector set of $\mathcal{W}$ is convex, if all possible vectors $\mathbf{x}_1, \mathbf{x}_2 \in \mathcal{W}$ combined with the arbitrary factor $t \in [0.1]$ to the form of

$$\mathbf{x} = t\mathbf{x}_1 + (1-t)\mathbf{x}_2\,, \tag{3.2}$$

1 A very comprehensive article about the reasons of sparse optimization besides acoustical optimization is given in [26]

result in a vector $\mathbf{x}$ that also lies in the set of $\mathcal{W}$. Figuratively spoken, each point on the vector between $\mathbf{x}_1$ and $\mathbf{x}_2$ has to be in the set $\mathcal{W}$ as figure 3.2 illustrates.

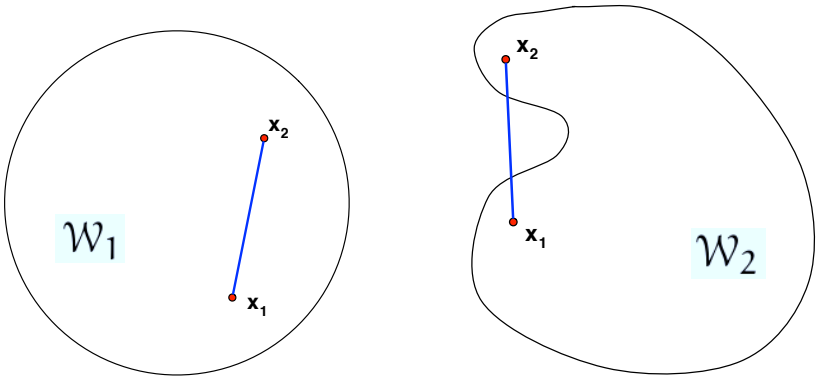

(a) Convex vector set $\mathcal{W}_1$ (b) Non-convex vector set $\mathcal{W}_2$

Figure 3.1: Description of convexity

A function $J(\mathbf{x})$ is strictly convex if it satisfies the inequality[2]:

$$J(t\mathbf{x}_1 + (1-t)\mathbf{x}_2) < tJ(\mathbf{x}_1) + (1-t)J(\mathbf{x}_2) \tag{3.3}$$

Furthermore, it has to fullfill the property:

$$J(\mathbf{x}_2) \geqslant J(\mathbf{x}_1) + \nabla J(\mathbf{x}_1)^T(\mathbf{x}_2 - \mathbf{x}_1) \tag{3.4}$$

The ℓ_2-norm $J(\mathbf{v}) = \|\mathbf{v}\|_2$, used as penalty function in chapter 2, fulfills all of this demands. However, there are other functions that are convex too. In fact, all so called ℓ_p-norms share this property for $p > 1$ [27]. These functions are defined as follows:

$$\|\mathbf{x}\|_p = \left(\sum_i |x_i|^p \right)^{\frac{1}{p}} \tag{3.5}$$

The characteristic of these norms can be used to solve a diversity of problems. Applying them as a penalty function, the optimization process can be properly controlled to answer to the special needs of each individual problem. In figure 3.2, the so called ℓ_p-balls, a kind of unity circle for the norms, are depicted for the ℓ_1, the ℓ_2 and the ℓ_∞-norm.

The extension of possible penalty functions to a set of eligible options is now utilized to give a solution to the misfits we were facing in chapter 2. For this, the ℓ_1-norm is further analyzed and the advantages and drawbacks are demonstrated.

2 If we add equality to this equation, we can still speak of convex functions. The result of this will be apparent in chapter 3.1.2

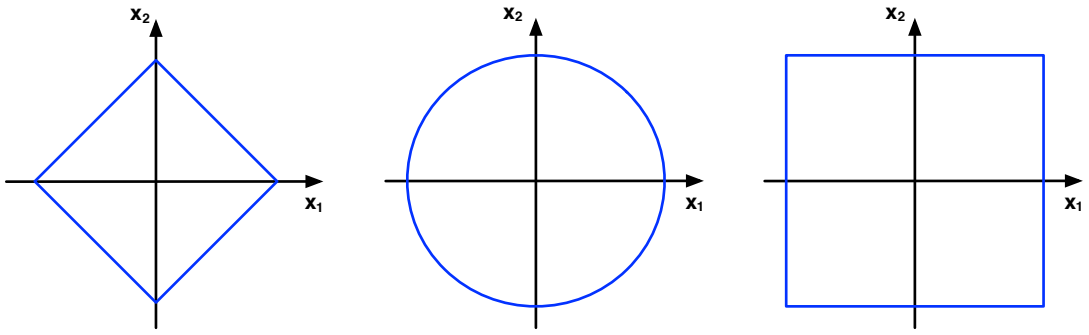

(a) ℓ_1-norm (b) ℓ_2-norm (c) ℓ_∞-norm

Figure 3.2: 2-dimensional ℓ_p-balls

3.1.2 *Application of the ℓ1-norm - sparse optimization*

In general, a signal vector $\mathbf{x}$ is called sparse if only a small number of elements is large and all other entries tend to zero [30]. The ℓ_1-norm as a penalty function is suitable for enforcing sparsity of the solution. It is obtained by setting $p = 1$ in eq.3.5. Employing this norm as a penalty function, we can only achieve a convex, but not a strictly convex optimization problem. This means that the optimization problem may have more than one solution. Nevertheless we know that among these solutions the most sparse option exists. To demonstrate the characteristic properties of sparse optimization, a random underdetermined problem is generated with the sparse vector $\mathbf{x}$ and the system matrix $\mathbf{A}$

$$\mathbf{A}\mathbf{x} = \mathbf{b} \tag{3.6}$$

where $\mathbf{A} \in \mathbb{C}^{M\times N}$, $\mathbf{x} \in \mathbb{C}^N$ and $\mathbf{b} \in \mathbb{C}^M$ and $M \ll N$. Assuming $\mathbf{A}$ and $\mathbf{b}$ are given and the linear constraint $\mathbf{A}\mathbf{x} = \mathbf{b}$ can be fulfilled by infinitely many solutions, a sparse solution is obtained by minimizing

$$\begin{aligned} &\min_{\mathbf{x}} \ \|\mathbf{x}\|_1 \,, \\ &\text{subject to } \ \mathbf{A}\mathbf{x} \ = \ \mathbf{b} \,. \end{aligned} \tag{3.7}$$

This formulation was introduced by Chen, Donoho and Saunders [28] as *Basis Pursuit (BP)*.

Before we solve this problem numerically, a geometrical explanation is given. With the description of the ℓ_p-balls in figure 3.2 and the formulation in eq. 3.7 we can construct a 2-dimensional example:

$$\begin{aligned} &\min_{\mathbf{x}} \ \|\mathbf{x}\|_1 \,, \\ &\text{subject to } \ \begin{pmatrix} \frac{1}{3} \\ \frac{1}{2} \end{pmatrix}^T \cdot \mathbf{x} \ = \ 1 \,. \end{aligned}$$

All possible solutions to the problem lie to a straight line that intersects the abscissa at $x_1 = 3$ and the ordinate at $x_2 = 2$ given by the constraint. To find the sparse solution in the ℓ_1-optimal sense, the ℓ_1-ball is minimized until the line intersects the ball at one point. The solution is unique only at this point as illustrated in figure 3.3. If the ℓ_1-ball and the constraint mistakenly intersect at two points due to a bad minimization, the solution is not unique anymore. If on the other hand no intersection exists, no solution can be found. To solve this sophisticated task, convex optimization techniques are applied.

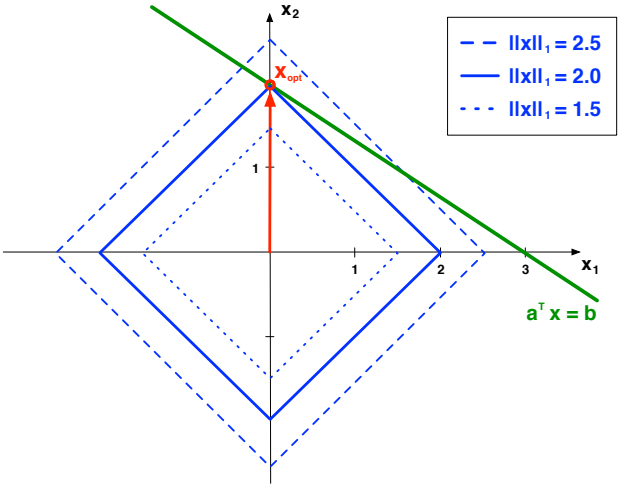

Figure 3.3: Sparse ℓ_1-solution to the given example

As we can see, a sparse solution is found. For comparison, the ℓ_2-optimized problem is illustrated in figure 3.4. We can see that the non-sparse solution vector consists of both linear components.

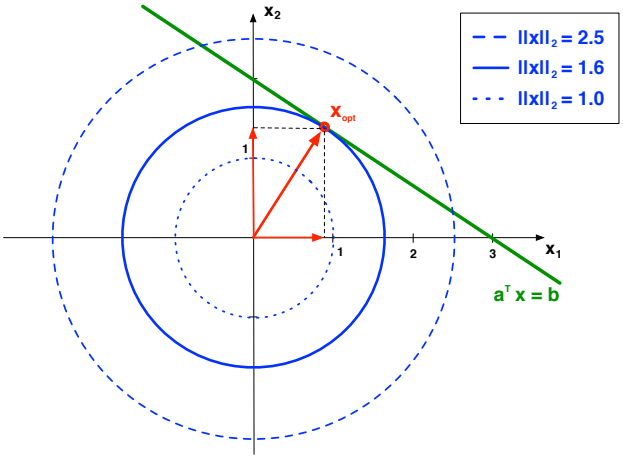

Figure 3.4: Non-sparse ℓ_2-solution to the given example

Using a convex optimization toolbox for MATLAB called *cvx*, the problem is now solved numerically by the following routine:

```
n = size(A,2);
cvx_begin
    variable x(n) complex;

    minimize(norm(x,1));
    subject to
        A*x == b
cvx_end
```

The numerical solutions to this simple example are $\mathbf{x}_{\ell_1} = \binom{0}{2}$ for the sparse optimization and $\mathbf{x}_{\ell_2} = \binom{0.92}{1.38}$ for the least-squares solution.

For the upcoming examples, it is important to declare the variable x to be complex if the problem is complex valued[3]. The toolbox thereby selects the appropriate solver. Complex-valued problems usually require a formulation into a so called *second-order-cone problem*, instead of *linear programming*. Both methods are not further addressed in this thesis, but good and comprehensive descriptions can be found in [29] and [30].

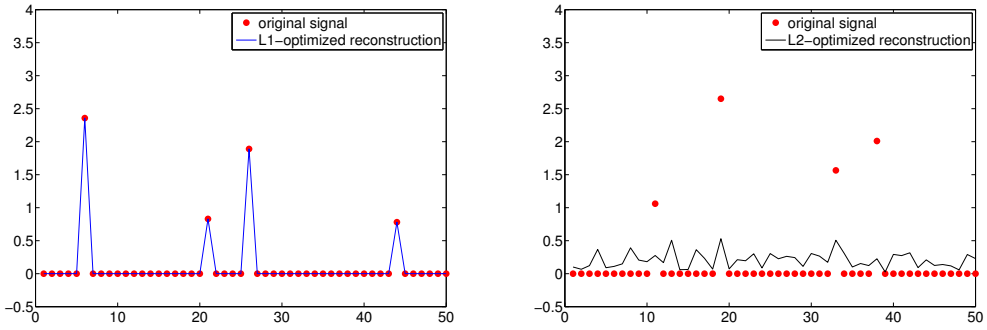

(a) Constrained ℓ_1-minimization (b) Constrained ℓ_2-minimization

Figure 3.5: Solutions to an example problem known to be sparse

Figure 3.5a displays the ℓ_1-minimum solution of another example, which is perfectly solved. By contrast, the least-squares solution (ℓ_2-minimum) in fig. 3.5b does not retrieve the sparse vector. The example demonstrates the energy smearing introduced by the ℓ_2-minimum when solving sparse problems. A closer look at the linear combination of the solution can confirm this guess. In figure 3.6, another simple underdetermined system is given. It consists of a 2-dimensional vector set, the sum of which shall represent a given vector. Each linear component is shown for both, the ℓ_1 and the ℓ_2-minimum. Again, the ℓ_2-solution yield broadly distributed shares in contrast to the sparse ℓ_1-optimized result.

3 For simplification, the variable was already declared complex for the first example.

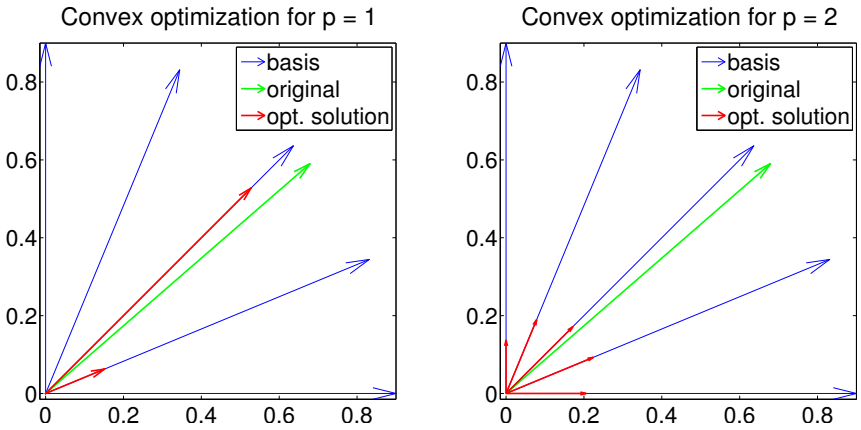

(a) Convex ℓ_1-optimization (b) Convex ℓ_2-optimization

Figure 3.6: Sparse ℓ_1 and spread ℓ_2-solution to an underdetermined linearly constrained 2-dimensional problem

3.1.3 *Sparse optimization in the presence of noise*

Up to now, all simulations were performed considering ideal systems without noise, usually present in physical measurements. However, if noise exist, the sparse solution might degrade and become invalid. In figure 3.7, this degradation is displayed for a signal-to-noise ratio (SNR) of 60dB (fig. 3.7a) and 40dB (fig. 3.7b).

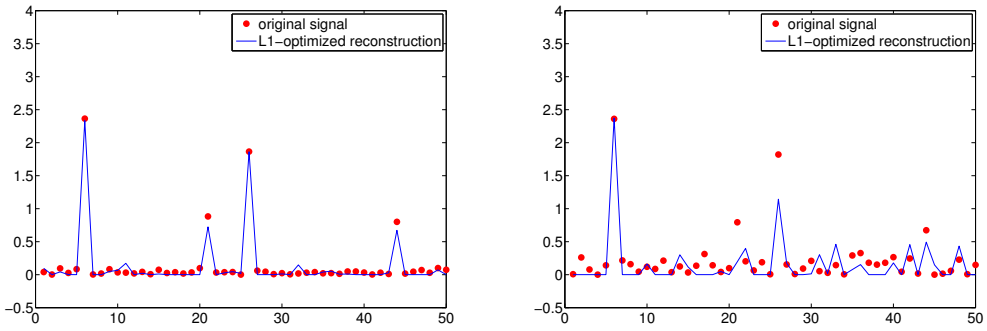

(a) ℓ_1-optimization with SNR = 60dB (b) ℓ_1-optimization with SNR = 40dB

Figure 3.7: Solutions to a sparse problem with noisy data

To improve the optimization task on noisy data, a regularization parameter β is useful to control the level of noise permitted in the data. As the noise can be complex-valued, this regularization parameter can be seen as radius within which the linear constraint is allowed to mismatch. The op-

timization task in this case is known as the *basis pursuit denoising (BPDN)* [28]:

$$\min_{\mathbf{x}} \ \|\mathbf{x}\|_1 \ , \qquad \text{subject to} \ \ \|\mathbf{A}\mathbf{x}-\mathbf{b}\|_2^2 \ \leqslant \ \beta \tag{3.8}$$

In *cvx*, we may write this as:

```
n = size(A,2);
cvx_begin
    variable x(n) complex;

    minimize(norm(x,1));
    subject to
        sum(square_abs(A*x - b)) <= beta;
cvx_end
```

Figure 3.8 displays solutions for a realistic scenario with a SNR of 60dB and the parameter β set to $\beta = 0.9$ or $\beta = 4$, respectively. With this regularization, a better result is achieved (see fig. 3.11a). However it is important not to over-regularize the optimization because the solution tends to zero if the linear constraint is weakened too heavily (cf. fig. 3.11b).

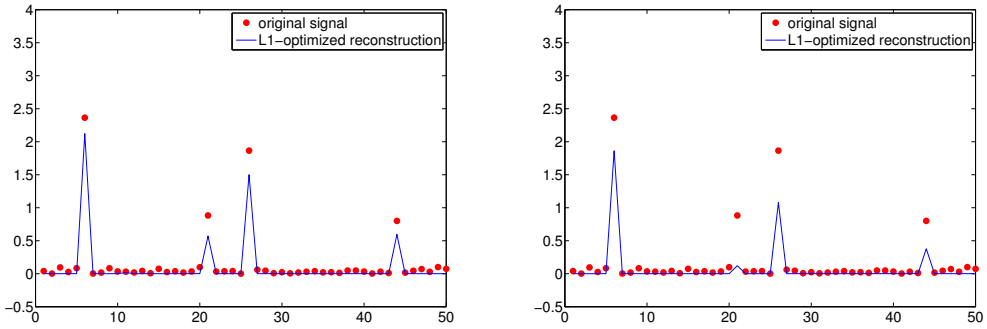

(a) ℓ_1-optimization with $\beta = 0,9$ (b) ℓ_1-optimization with $\beta = 4$

Figure 3.8: Solutions to a regularized sparse problem with SNR = 60dB and a weakened linear constraint

In chapter 2.2.1, we already formulated the solution to the *planar acoustic holography (PAH)* based on Rayleigh integrals:

$$\mathbf{p}_M = 2j\omega\rho \cdot \mathbf{G}_{M\times N}\, \mathbf{v}_N \,. \tag{3.9}$$

Usually, we desire more points to be calculated on the source plane than measurement points exist. This leads to an underdetermined system of equation ($M \ll N$). To obtain a reasonable solution, we may formulate a minimization problem with the linear equality constraint and a penalty function $J(\mathbf{v})$:

$$\begin{aligned} \min_{\mathbf{v}} \quad & J(\mathbf{v}) \\ \text{subject to} \quad & 2j\omega\rho \cdot \mathbf{G}\mathbf{v} \;=\; \mathbf{p} \end{aligned} \tag{3.10}$$

In contrast to chapter 2, we now want to focus on sparse solutions to this problem which means that we search for a proper $J(\mathbf{v})$.

3.2.1 *Formulation to enforce sparsity in space*

A sparse Rayleigh integral of PAH contains only a few non-zero surface components, i.e. the velocity becomes zero on most of the source plane. Therefore the basis pursuit of eq. 3.7 is a viable solution strategy. To handle noisy data and to provide an option to control its influence, the basis pursuit of denoising (BPDN) provides a reasonable strategy. The sparsity promoting formulation to the Rayleigh-based PAH for *sparse holographic imaging* therefore becomes:

$$\begin{aligned} \min_{\mathbf{v}} \quad & \|\mathbf{v}\|_1 \\ \text{subject to} \quad & \|2j\omega\rho \cdot \mathbf{G}\mathbf{v} - \mathbf{p}\|_2^2 \;\leqslant\; \beta \,. \end{aligned} \tag{3.11}$$

In *cvx*, this is solved by the code:

```
n = size(G,2);
cvx_begin
    variable v(n) complex;

    minimize(norm(v,1));
    subject to
        sum(square_abs((2*1i*omega*rho)*G*v - p)) <= beta;
cvx_end
```

For problems that are proven not to be sparse in space, an ℓ_1-optimization of the source velocity is not suitable. Thus, it is necessary to make careful assumptions on the nature of the given problem. The following sections provide further ideas to enhance the solution and to expand the application range.

3.2.2 *Blending between sparse and non-sparse problems*

Up to this point, we only considered integer numbers for the value p in eq. 3.5. However it is also possible to set p to values between $1 < p < 2$ which we expect to work as a crossfade between sparse and energy distributing optimization. The behavior of the penalty function for $1 < p < 2$ is displayed in figure 3.9a for one quadrant of the ℓ_p-balls.

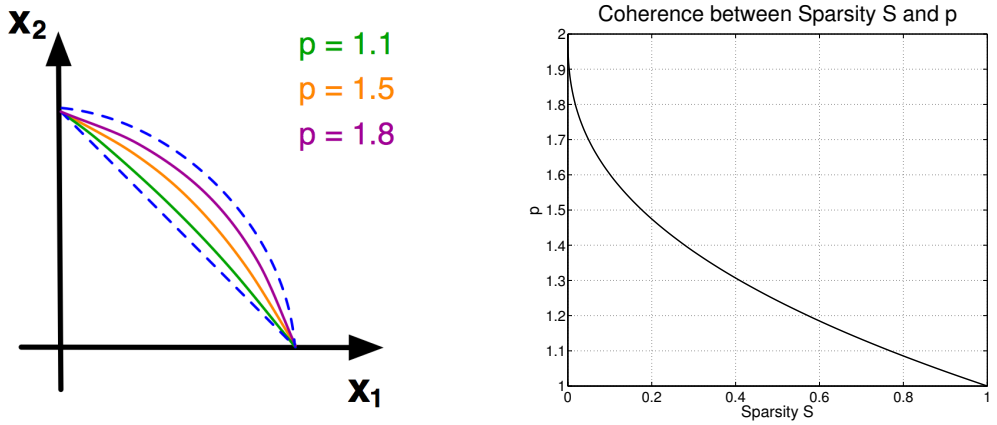

(a) $\|x\|_p$ between $1 < p < 2$ (b) The sparsity parameter

Figure 3.9: Blending between sparse and non-sparse representation

Solutions for an optimization using values for p between 1 and 2 are displayed in figure 3.10 for the multidimensional system already introduced in chapter 3.1.2. Clearly we can trace the degradation of the sparse linear combination to a solution components of all existing basis vectors. However, the main mutation certainly happens between $p = 1$ and $p = 1,5$. For larger values, the solutions almost corresponds to the least-squares optimization. To meet this behavior and to give a parameter that is easier to control, the empirical sparsity control parameter S is introduced.

$$S = (2 - p)^{\frac{5}{2}} \tag{3.12}$$

The application of this parameter is helpful to solve problems that are not perfectly sparse in space and it makes it easy, to blend between possible solutions when analyzing the given measurement problem.

The range is given from $S = 0$ for the least-squares solution to the maximum sparse optimization using the ℓ_1-penalty at $S = 1$. The mapping between p and this new parameter S is illustrated in fig. 3.9b. Furthermore, realizations of the linearly constrained 2-dimensional vector problem are plotted in appendix A.1 for different levels of the sparsity parameter S.

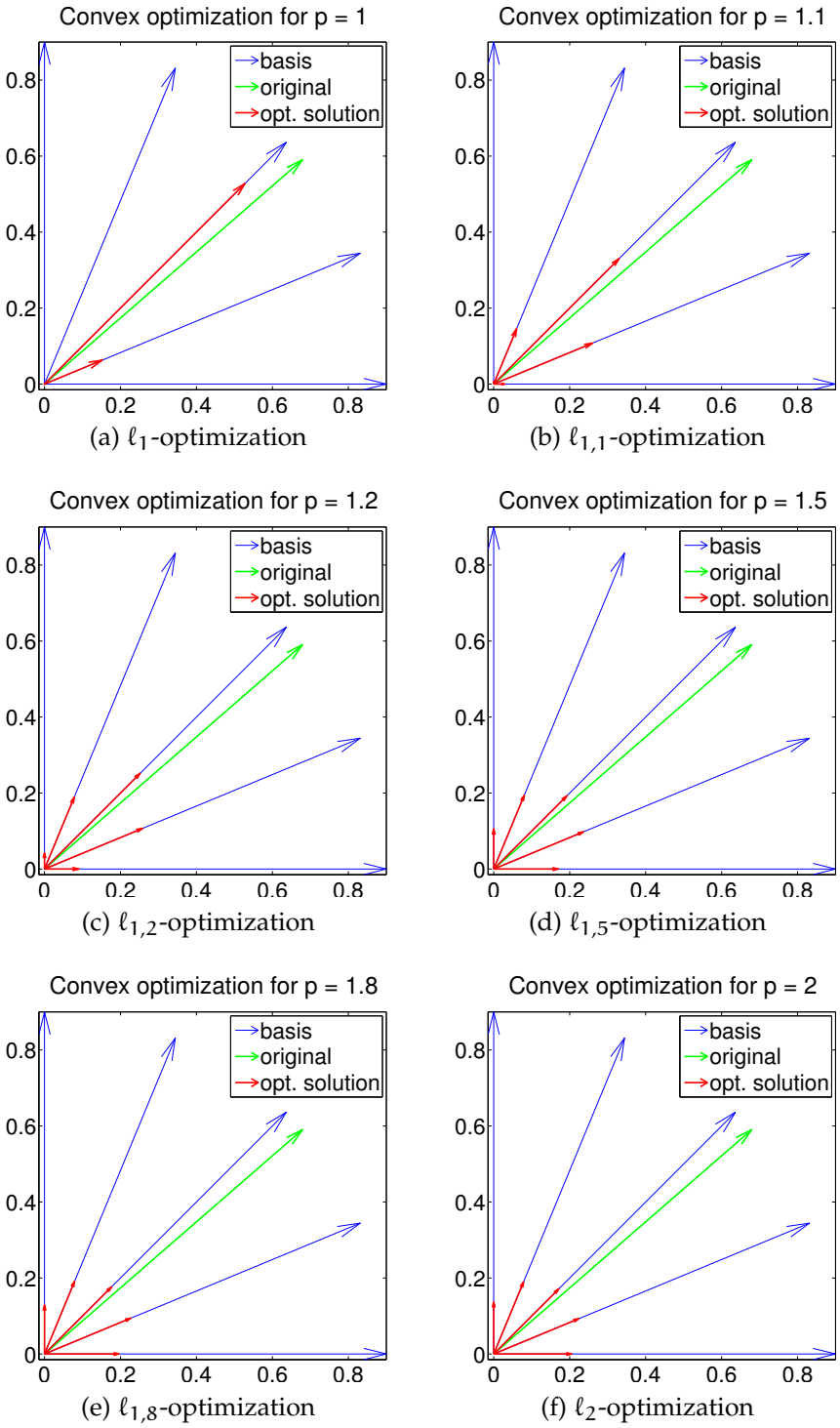

(a) ℓ_1-optimization (b) $\ell_{1,1}$-optimization (c) $\ell_{1,2}$-optimization (d) $\ell_{1,5}$-optimization (e) $\ell_{1,8}$-optimization (f) ℓ_2-optimization

Figure 3.10: Optimization of multidimensional example using different penalty functions

3.2.3 *Formulation to enforce sparsity of modes*

Problems, exhibiting surface modes are certainly not sparse in space. However, the concept of compressive sensing can still be applied, as modes also

have a sparse representation in the wavenumber-domain. Therefore, the problem can be solved in this domain by sparse optimization [26].

For a vibration pattern, the 2-dimensional transformation into this k-space is defined as:

$$V(k_x, k_y) = \int_{-\infty}^{+\infty} \int_{-\infty}^{+\infty} v(x, y) e^{-i(k_x x + k_y y)} dx dy \tag{3.13}$$

A plate that vibrates in its 2,2 - mode is therefore described by only four components in the k-space [11]:

$$\cos(k_{x0} x) = \frac{1}{2} \left(e^{i k_{x0} x} + e^{-i k_{x0} x} \right)$$

$$\cos(k_{y0} y) = \frac{1}{2} \left(e^{i k_{y0} y} + e^{-i k_{y0} y} \right)$$

From this description we can directly read the sparse equivalence to the broadly distributed velocity (cf. figure 3.11).

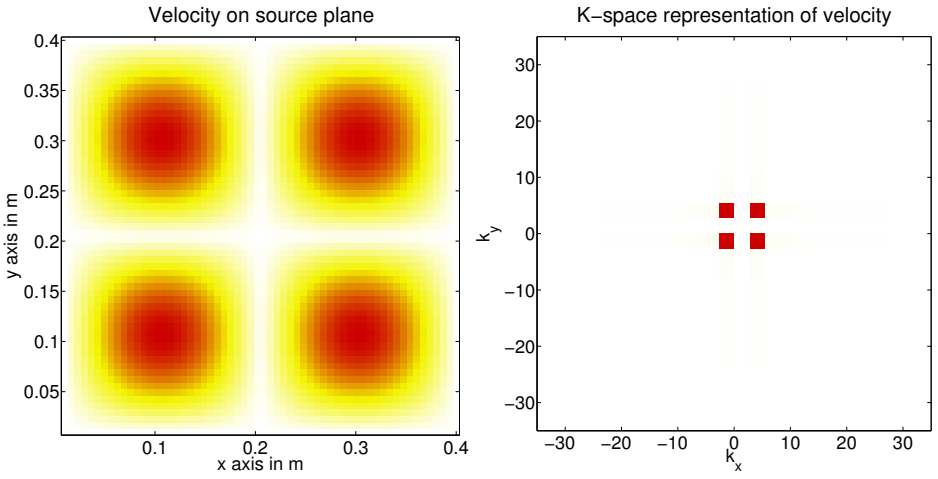

(a) plate mode 2-2 in space (b) plate mode 2-2 in k-space

Figure 3.11: Modal vibration of a plate and its sparse k-space representation

On discrete measurements along x and y, the transformation into k-space is achieved by multiplying the velocity with

$$\mathbf{f}^{(l_x, l_y)}_{(w_x, w_y)} = e^{-i \frac{2\pi}{N^2} (w_x l_x + w_y l_y)} ,$$

where

w_x	frequency bin in x-direction
w_y	frequency bin in y-direction
l_x	step size in x-direction
l_y	step size in y-direction ,

so that

$$\mathbf{V}[w_x, w_y] = \sum_{l_x, l_y} \mathbf{v}[l_x, l_y] \, \mathbf{f}^{(l_x, l_y)}_{(w_x, w_y)} .$$

It is important to mention that this transformation only works for a rectangular, equidistant measurement grid. For other grids, an inversion of the Fourier-synthesis matrix would be required.

The sparse optimization in k-space is again performed with the help of the *cvx*-toolbox. This time, the penalty function contains the transformation mentioned above in terms of a matrix:

$$\mathbf{F} = \left[\mathbf{f}_{(w_x,w_y)}^{(l_x,l_y)}\right]_{(w_x,w_y)}^{(l_x,l_y)} .$$

```
n = size(G,2);
    cvx_begin
        variable v(n) complex

        minimize(norm(F*v,1));
        subject to
              norm((2*1i*omega*rho)*G*v - p) <= beta ;
    cvx_end
```

A simple crossfade-parameter w might combine both, mode and spatial formulations. With this, the solution can either support sparsity in space or in modes, however at a strongly increased computation cost and maybe not the best controlability:

```
n = size(G,2);
    cvx_begin
        variable v(n) complex

        minimize((1-w)*norm(v,1)+(w)*norm(F*v,1));
        subject to
              norm((2*1i*omega*rho)*G*v - p) <= beta ;
    cvx_end
```

With $w = 0$ sparsity in space is promoted whereas $w = 1$ leads to a sparse optimization of modes.

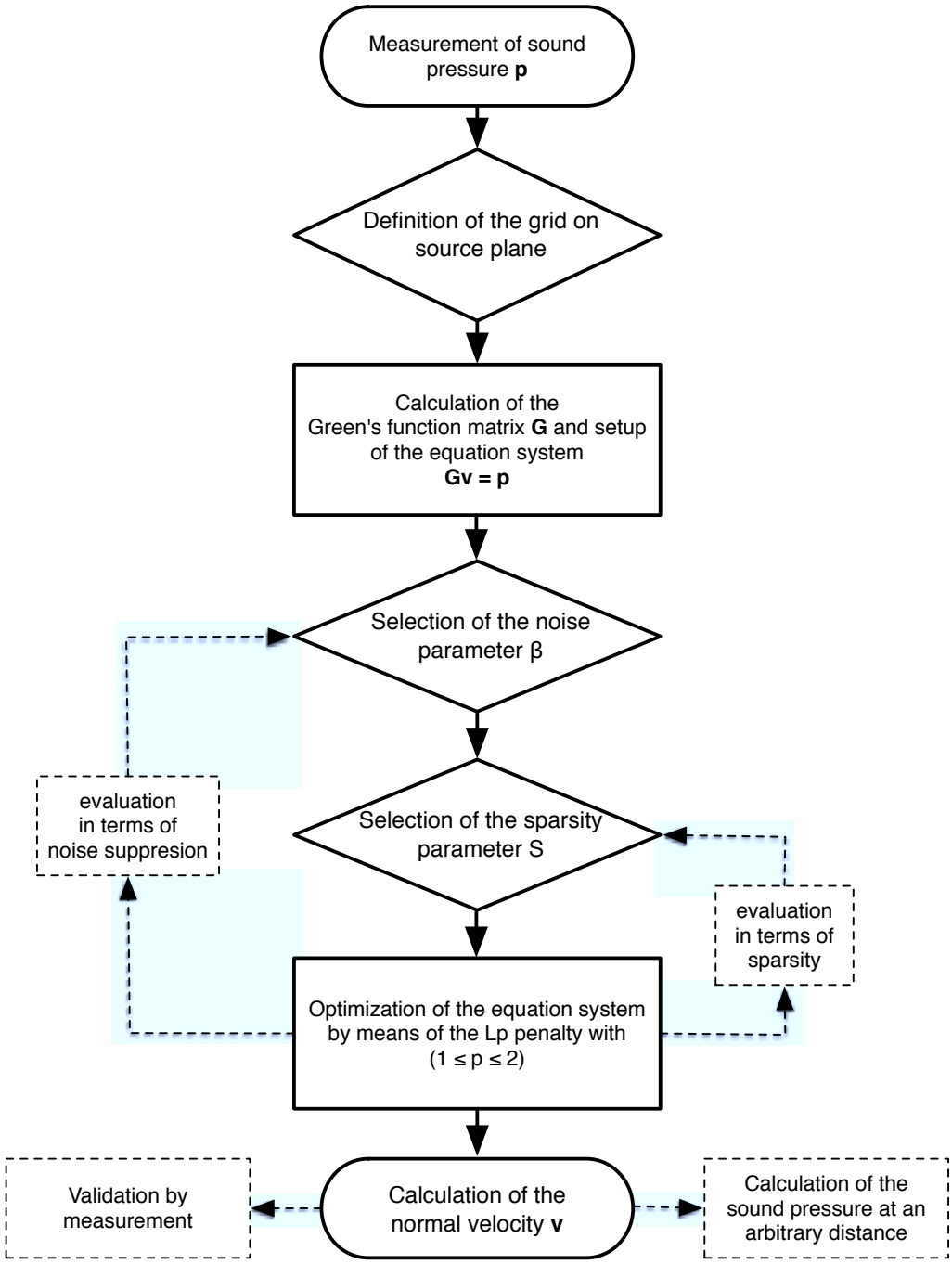

Figure 3.12: State graph of the sparse holographic imaging

In this chapter, the simulation results of sparse optimized PAH problems are presented. For this, similar setups like in chapter 2 are chosen, where the least-squares optimization was examined.

3.3.1 *Sparse optimized PAH solution for point sources*

To analyze the sparse PAH solution, we evaluate the simulation setup of the solid plate already presented in chapter 2.3.2. The sound pressure propagation of the three point sources is given in figure 2.28 of the previous chapter 2. To compare the results with the least-squares solution of chapter 2, the measurement aperture is initially simulated at a distance of $0.02\mathrm{m}$ and analyzed at a frequency of 1000Hz. Further measurement distances are simulated to get a feeling how well the ℓ_1-optimization behaves for the vanishing evanescent wave components. Figure 3.13 illustrates the results for the sparse optimized PAH of the exactly determined equation system.

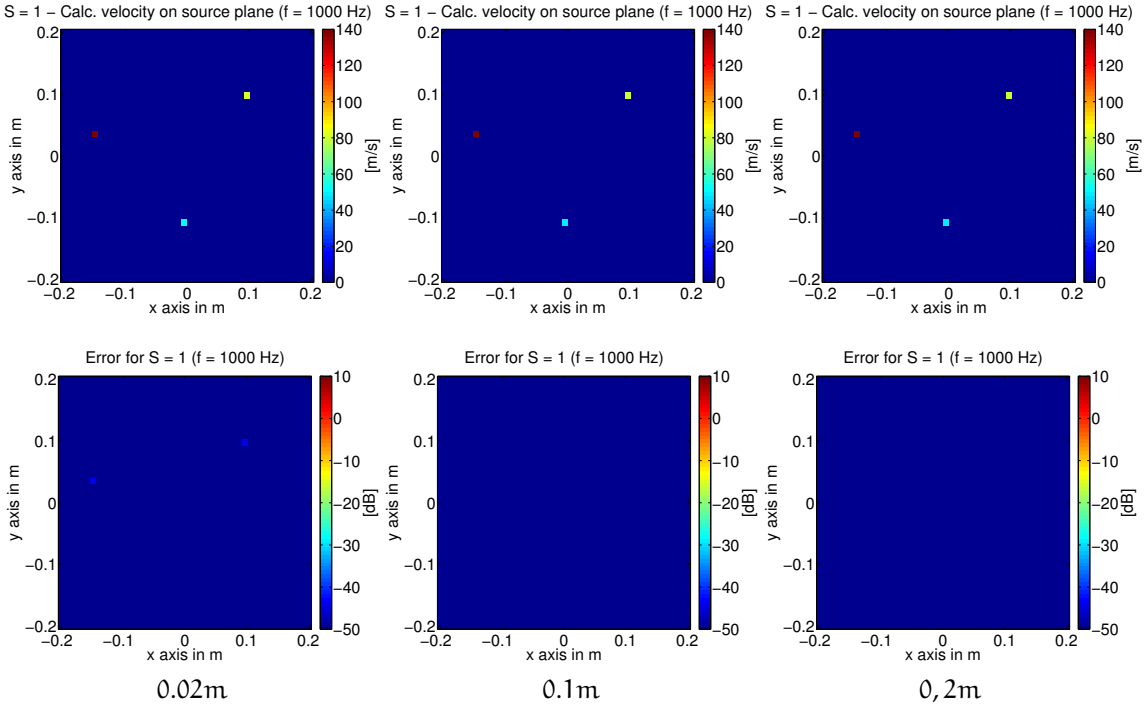

Figure 3.13: ℓ_1-optimized normal velocity on source plane (upper row) and equivalent error (lower row) for the exactly determined equation system

The sparse optimization reveals a good solution to the exactly determined system for $a = 0.02\mathrm{m}$ and surprisingly an even better result for a placement at $a = 0.1\mathrm{m}$. The reason for the enhanced error at a closer positioning results from higher wavenumber components near the point source as described in chapter 2.2.6. It is also important to mention that noise due to the

vanishing evanescent waves at higher distances might lead to a degeneration of the solution. To circumvent the resulting artifacts, the regularization parameter of β has to be set to $\beta = 0.9$ to come to this solution.

To judge the performance of the sparse optimization concerning underdetermined systems, the analysis is performed for microphone arrays of 8×8, 6×6 and 4×4 sensors. The results displayed in figure 3.14 illustrate a significant increase of accuracy compared to the former simulations where the least-squares solution was applied (cf. figure 2.31). For the optimization of fig. 3.14, we also choose the regularization parameter $\beta = 0,9$.

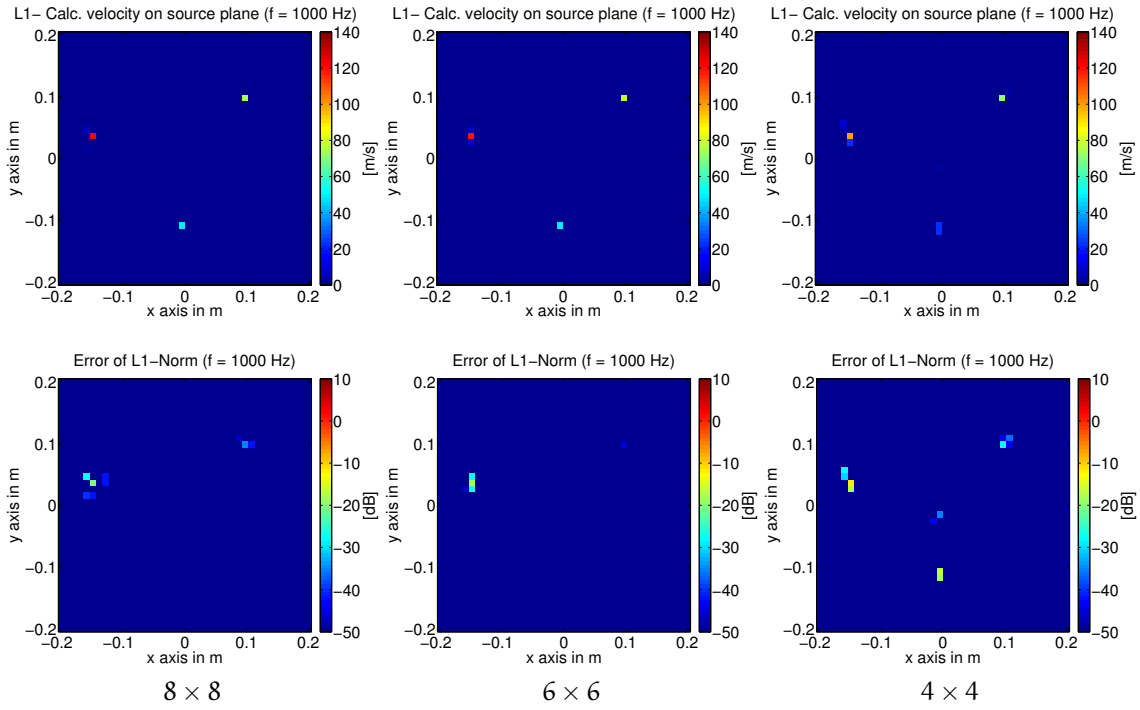

Figure 3.14: Calculated normal velocity (upper row) and equivalent error (lower row) for a measurement distance $a = 0.02m$ at $f = 1000Hz$ and reduced sensor positions

Evaluating the results in table 3.1 reveals that the error e does obviously not increase linearly with the number of measurement points. There are two cases, where a reduction of microphones even leads to a smaller error. However, slight variation of the sensor grid, ie. for the 8×8 setup at 3000Hz, leads to a bisection of the error to $e = 4,6$. This observation leads to the assumption that the quality of the result depends on the number and position of the microphones, the array distance, and the regularization parameter β.

A direct comparison between the least-squares and the sparse optimized PAH solution reveals that a suitable reconstruction for underdetermined sparse problems is only achieved by the ℓ_1-penalty. To illustrate the differ-

	40×40 $a = 0.02$	40×40 $a = 0.1$	40×40 $a = 0.2$	8×8 $a = 0.05$	6×6 $a = 0.05$	4×4 $a = 0.05$
300Hz	**0.7**	**0.75**	**4.14**	**14.3**	**9.3**	**119.9**
1000Hz	**1.4**	**0.36**	**0.1**	**12.4**	**14.5**	**35.9**
3000Hz	**0**	**0.002**	**0.005**	**9.3**	**5.2**	**1.51**

Table 3.1: Single value error e for sparse optimized solutions

ence between the ℓ_1-optimized and the ℓ_2-solution, figure 3.15 shows the PAH result of an array with 4×4 microphones. The single value error of table 3.2 confirms this significant difference between sparse and least-squares optimized PAH.

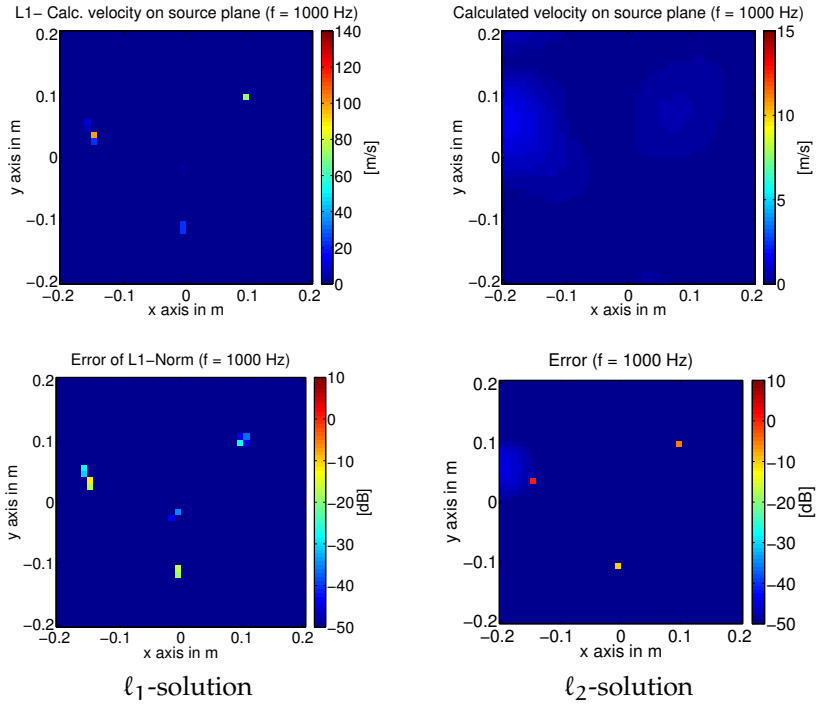

ℓ_1-solution ℓ_2-solution

Figure 3.15: Comparison of ℓ_1 and ℓ_2-optimized normal velocity on source plane for 4×4 microphone positions at $a = 0.05\text{m}$

4×4	ℓ_1-optimized	ℓ_2-optimized
1000Hz, $a = 0.05\text{m}$	**35.9**	**99.6**

Table 3.2: Single value error e for 4×4 aperture at 0.05m

3.3.2 *Sparse optimized PAH solution to modal vibration*

This chapter investigates the new tool of sparse optimization to resolve structural modes. As described in chapter 3.2.3, a transformation into the

k-space results in a sparse representation of structural modes. We simulate the optimization of the resonating plate already described in chapter 2.3.1 with a measurement aperture of 8×8 and 6×6 sensors at a distance of $0.05\mathrm{m}$. Figure 3.16 compares the result of the this approach with the ℓ_2-optimization. It shows that the ℓ_2-solution yields slightly better results, which also holds for a reduced number of microphones and a larger distance. The regularization parameters for both simulations were set to values that yield satisfactory results.

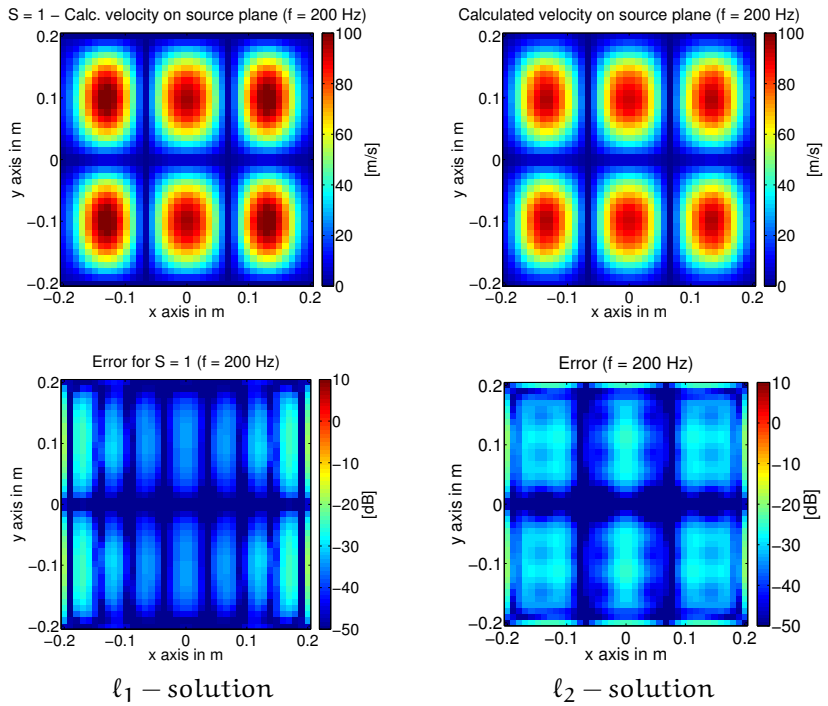

Figure 3.16: Comparison of ℓ_1 and ℓ_2-optimized normal velocity on the source plane for 8×8 microphone positions at $a = 0.05\mathrm{m}$

	6×6	8×8
ℓ_1-optimized	**16.1**	**7.4**
ℓ_2-optimized	**13.6**	**4.4**

Table 3.3: Single value error e for ℓ_1-optimized mode solutions at $a = 0.05\mathrm{m}$

However, it is important to mention that no further regularization was performed in k-space itself. It is most likely, to decrease the error and to reach the error values of the ℓ_2-optimized problem when using such techniques.

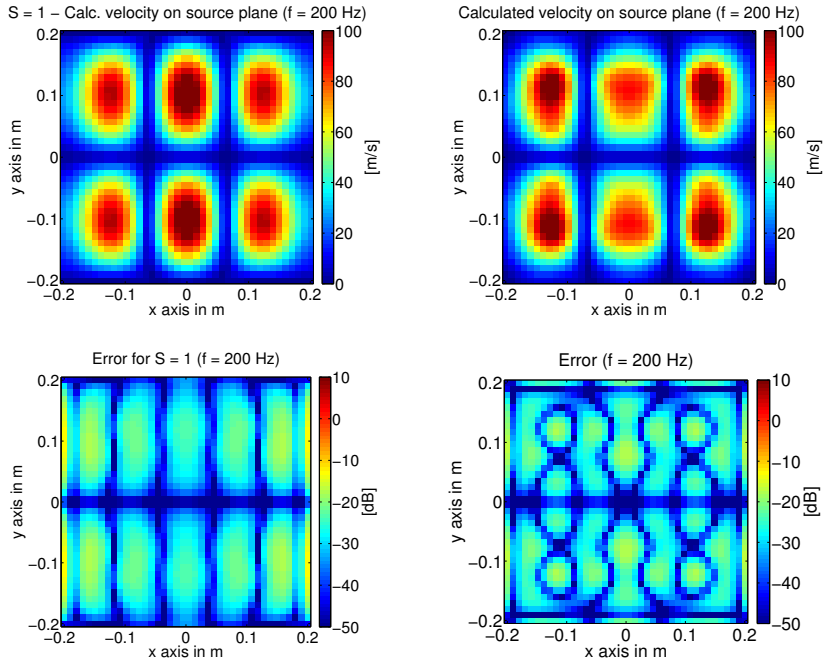

Figure 3.17: Comparison of ℓ_1 and ℓ_2-optimized normal velocity on source plane for 6×6 microphone positions at $a = 0.05m$

3.3.3 *Sparse optimized PAH in the presence of noise*

Up to now, we only considered the noise-free case in sparse holographic imaging. To evaluate the performance for systems with additional noise, the measured pressure values are corrupted by *white Gaussian noise*. The amount is denoted in terms of the *signal to noise ratio (SNR)* which is defined as

$$SNR = 10\log_{10}\left(\frac{\mathcal{P}_{signal}}{\mathcal{P}_{noise}}\right) = 20\log_{10}\left(\frac{p_{signal}}{p_{noise}}\right),$$

where

$\mathcal{P}_{signal}$	power of the desired signal,
$\mathcal{P}_{noise}$	power of the noise signal,
p_{signal}	sound pressure of the desired signal,
p_{noise}	sound pressure of the noise signal.

To begin with, the point source example is simulated for an 8×8 sensor setup at $0.05m$ distance with $SNR = 50dB$, $SNR = 40dB$ and $SNR = 30dB$. We now need to adjust the parameter β to handle the noise. Figure 3.18 displays the ℓ_1-optimized solutions to these corrupted examples. The values for the resulting error and the selected values for β are displayed in table 3.4.

A further reduction of the SNR leads to a degeneration of the reconstructed velocity. The noise is bundled by the optimizer into small peaks that corrupt the result. These "bundles" already occur at the solution for $SNR = 30dB$.

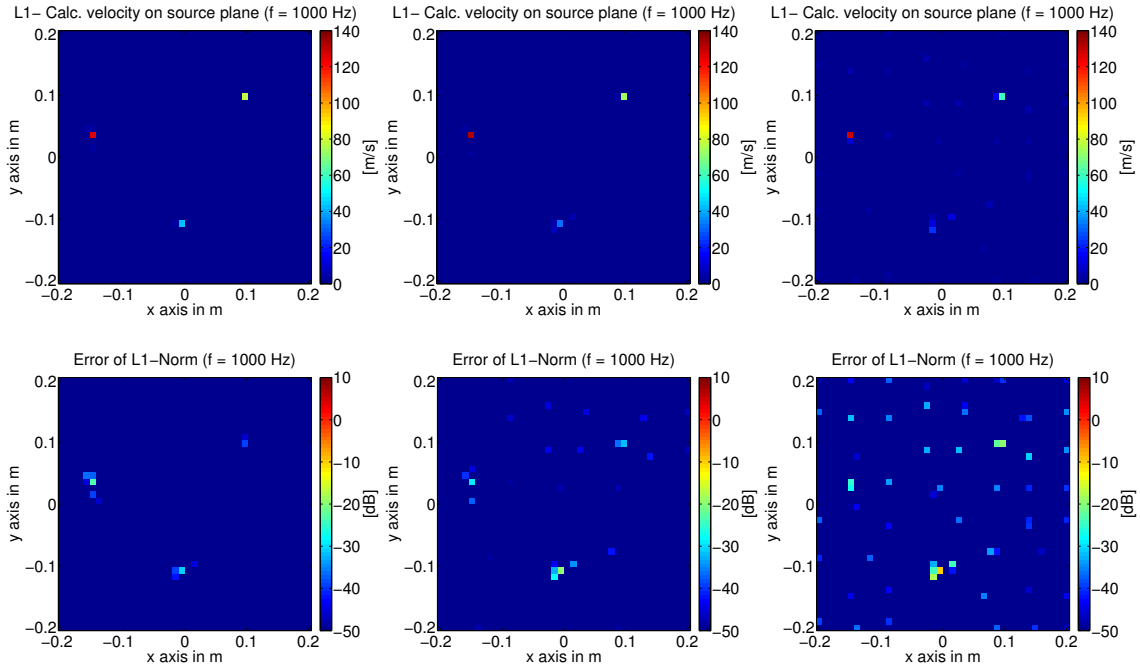

Figure 3.18: Calculated normal velocity (upper row) and equivalent error (lower row) for a measurement distance $a = 0.05m$ at $f = 1000Hz$ with 8×8 sensor positions and different SNR

8×8	SNR = 50dB	SNR = 40dB	SNR = 30dB
$a = 0.05$	$\beta = 1,1$	$\beta = 3$	$\beta = 30$
1000Hz	**10.2**	**15.4**	**40.1**

Table 3.4: Single value error e for noise corrupted solutions of the point source problem

By the use of a large noise suppression parameter $\beta = 30$ it is possible to suppress them and to reconstruct a reasonable result. However, this comes at the cost of the smallest source component which can hardly be recognized in the result.
Another interesting observation is that the error for the noise free example (cf. figure 3.14a) is a little larger than for the slightly noisy case (SNR = 50dB). The optimizer seems to handle the equally distributed white Gaussian noise better than shaped noise caused by evanescent waves.

The same analysis is performed for the sparse mode problem. Again, a setup of 8×8 microphones at a distance of $0.05m$ is chosen. The results are displayed in table 3.5 and figure 3.19.
For this example, only small enhancements due to the application of β can be observed. Further regularization techniques in k-space might be more efficient but are not the main focus of this thesis.

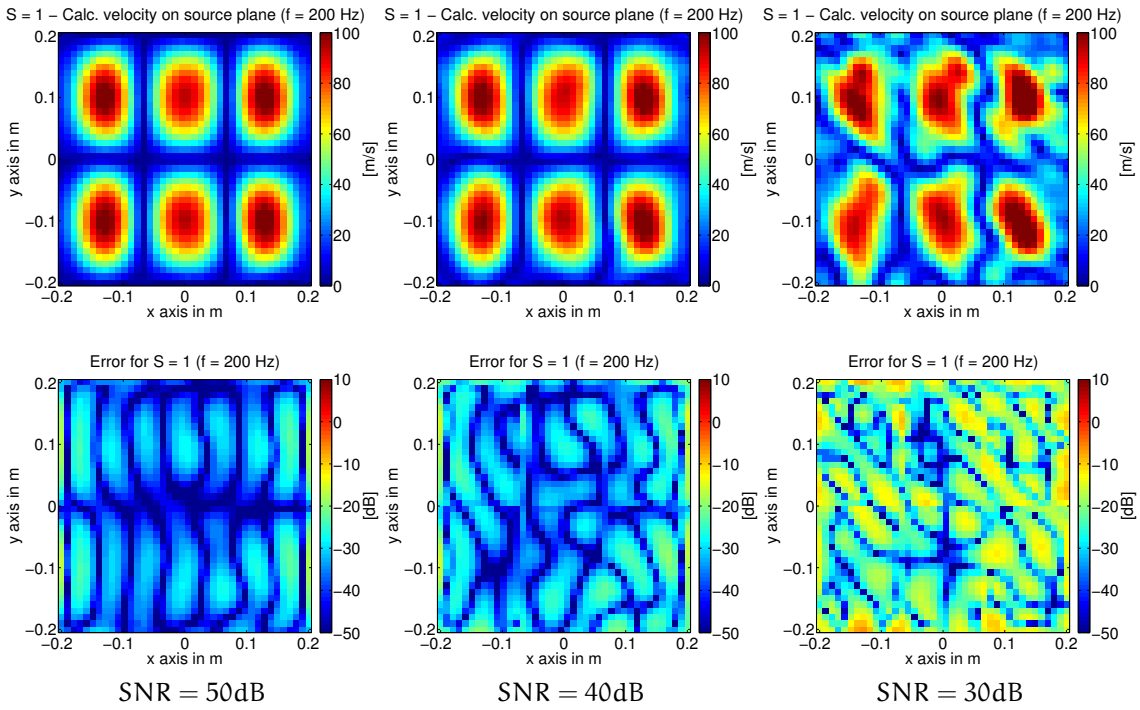

Figure 3.19: Calculated normal velocity (upper row) and equivalent error (lower row) for a measurement distance $a = 0.05m$ at $f = 200Hz$ with 8×8 sensor positions and different SNR

8×8	SNR = 50dB	SNR = 40dB	SNR = 30dB
$a = 0.05$	$\beta = 0.1$	$\beta = 3$	$\beta = 3$
1000Hz	**9.1**	**11.3**	**30.3**

Table 3.5: Single value error e for noise corrupted solutions of the spase mode problem

3.3.4 *Application of the Sparsity S*

To analyze the newly introduced parameter of *sparsity* S, a source excitation combined of several single components is assumed. This source layer consists of a sparse and a broadly distributed excitation at once and is shown in figure 3.20

The propagation of the sound pressure is again simulated for the frequencies 300Hz, 1000Hz and 3000Hz. To investigate the capability of the blending parameter S, a measurement of an 8×8 sensor array at a distance of $a = 0.05m$ is simulated for ℓ_1 ($S = 1$), ℓ_2 ($S = 0$) and an optimal sparsity parameter [4]. The simulations reveal that the capability of the ℓ_2-norm minimization to resolve sparse components is, as expected, limited. By contrast to this, the ℓ_1-solution tries to sparsify all of the exciting source velocity,

4 Detailed examples of stepwise blending between $S = 0$ and $S = 1$ are illustrated in appendix A.1 - A.4

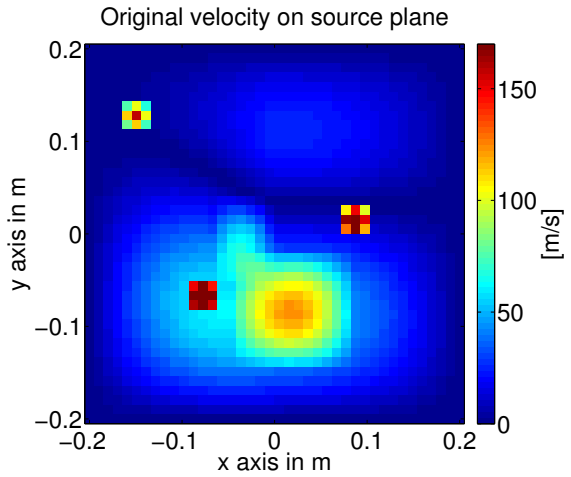

Figure 3.20: Normal velocity of a combined problem

which leads to a complete degeneration of the solution. For the optimal sparsity-value of this setup, we found $S = 0.65$ which corresponds to an optimization with an ℓ_p-norm with $p = 1.06$. The results are illustrated in figure 3.21.

However, the single value error e used to adapt to this solution might not be the best choice for an optimal result in terms of source identification. In figure 3.22 we can see that it is even possible to enforce the sparsity further, although this leads to a increase of the single value error. As this quality parameter only holds one value it is questionable if it is able to judge the distribution of sparse sources at all. In this case, it seems to be adequate, to select the solution empirically by looking at the calculated velocity.

Another important issue is that the quality of the optimization clearly depends on the combination of sparse and broadly distributed sources. If a sparse component is located on top of a modal maximum, either the spread or the sparse component gets optimized.

Figure 3.23 and 3.24 display this evaluation also for the frequencies 1000Hz and 3000Hz. The results are similar to the former evaluation at 300Hz.

8×8 $a = 0.05$	$e(S = 1)$	$e(S = \text{opt.})$	$e(S = 0)$
300Hz	**529**	**31.7**	**36.8**
1000Hz	**466**	**31.9**	**36.8**
3000Hz	**366**	**36.6**	**37.4**

Table 3.6: Single value error e for the combined problem at different values of S

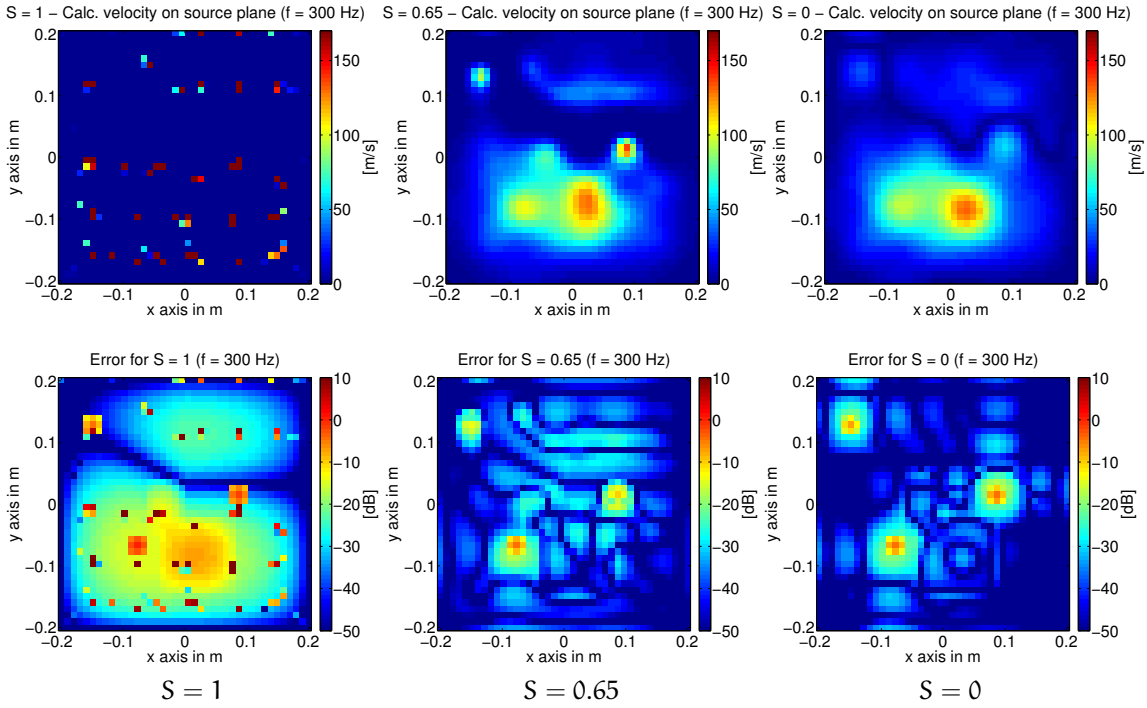

Figure 3.21: Calculated normal velocity (upper row) and equivalent error (lower row) for a measurement distance $a = 0.05m$ at $f = 300Hz$ with 8×8 sensor positions and different values for sparsity S

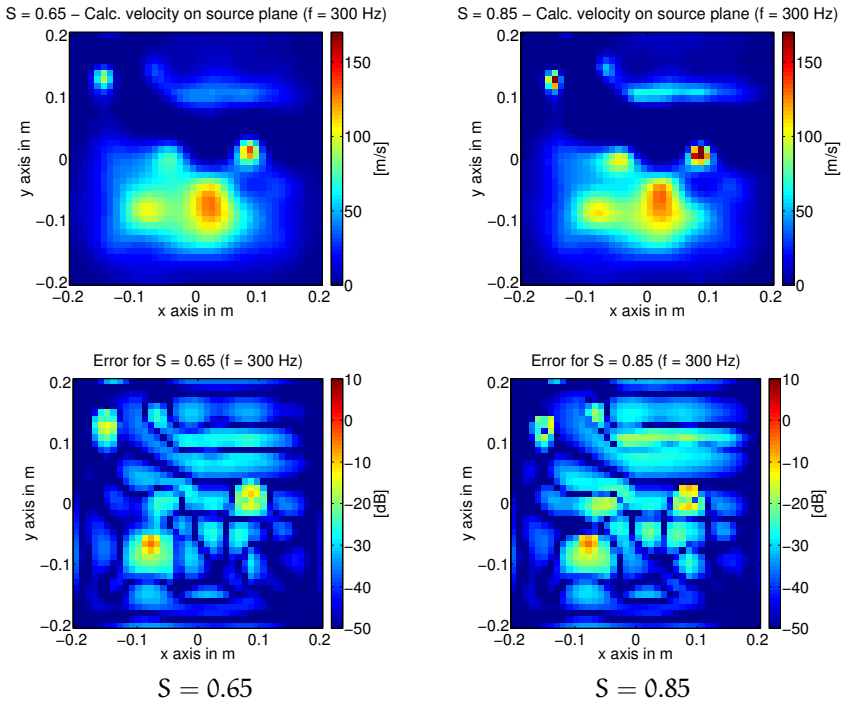

Figure 3.22: Comparison of the optimized normal velocity on source plane for different values of S. Although the right solution yield an increased error, it leads to a better resolution.

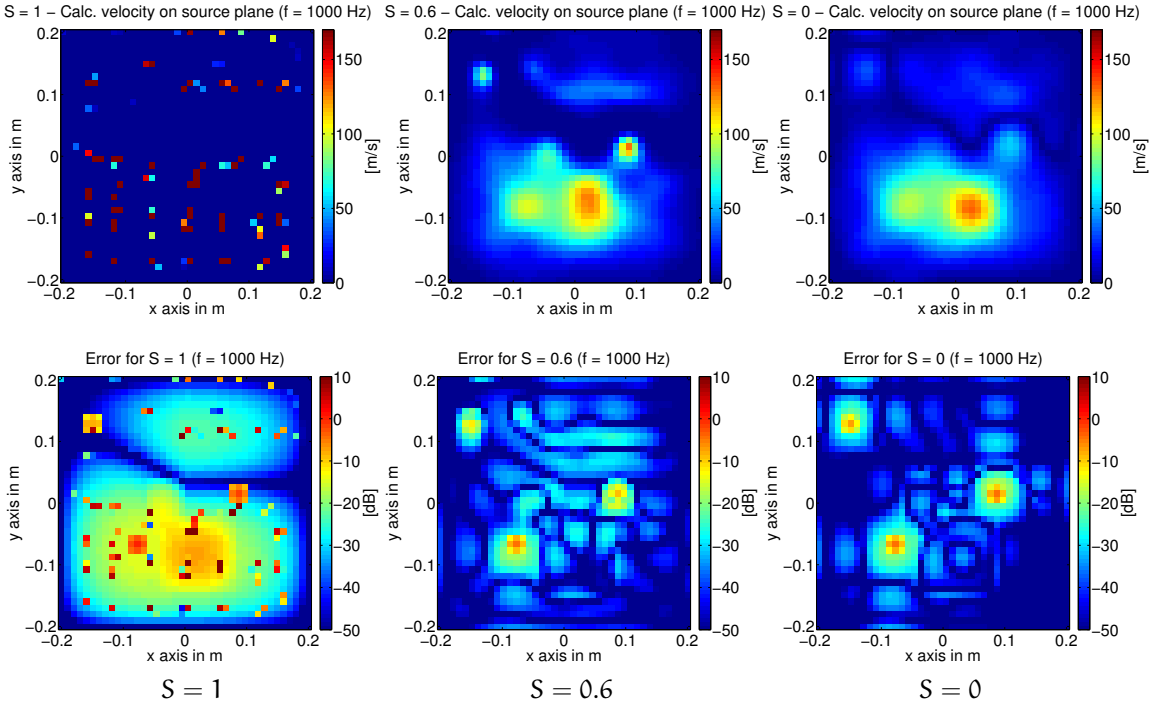

Figure 3.23: Calculated normal velocity (upper row) and equivalent error (lower row) for a measurement distance $a = 0.05m$ at $f = 1000Hz$ with 8×8 sensor positions and different values for sparsity S

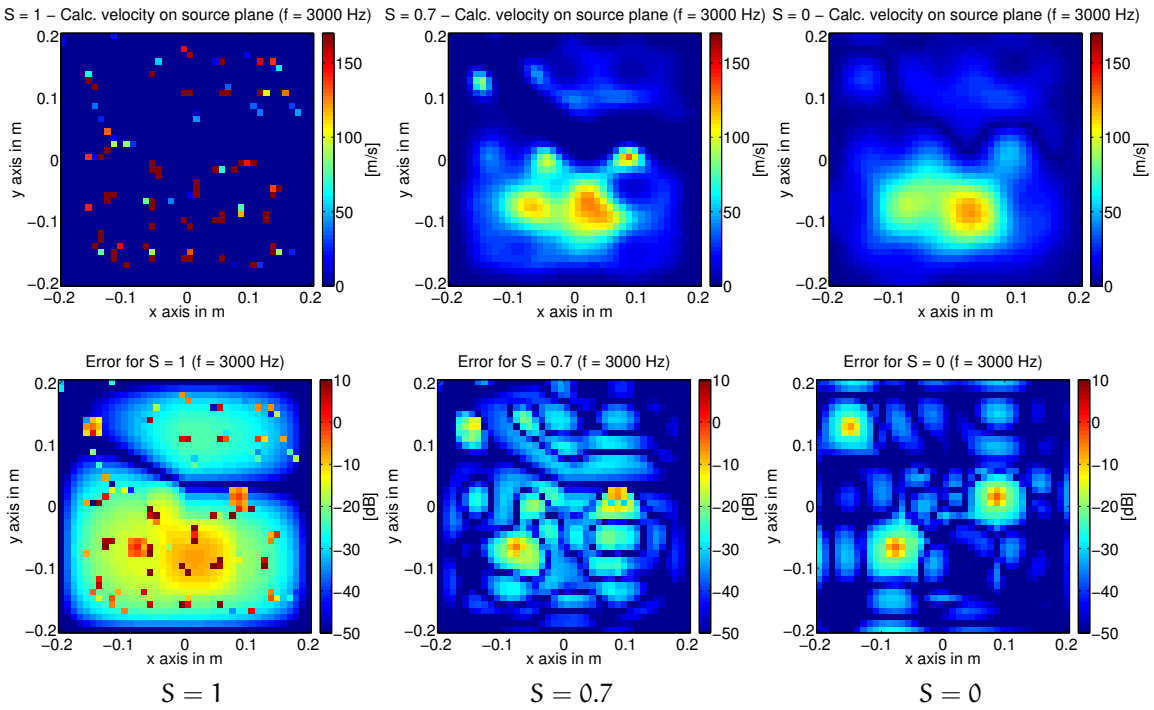

Figure 3.24: Calculated normal velocity (upper row) and equivalent error (lower row) for a measurement distance $a = 0.05m$ at $f = 3000Hz$ with 8×8 sensor positions and different values for sparsity S

3.4 SUMMARY

In this chapter, the theory of sparse optimization was introduced and evaluated for the Rayleigh-based PAH. Thereby it has become obvious that suitable optimization criteria can enhance the resolution of the planar acoustic holography. This depends on the kind of the given problem and the choice of adequate ℓ_p-penalties. The presented solutions are stable even in the presence of noise. Because real-world problems are never perfectly sparse, a blending parameter "sparsity" S was introduced to permit seamless adjustment in cases that are somewhat between sparse and spread modal.

The computational cost of this sparse holographic imaging is much bigger than for the "classical" ℓ_2-penalized PAH solution. Nevertheless, the advent of sparse optimization algorithm will probably lead to faster implementations in the future.

4 MEASUREMENTS

To evaluate the power of the Rayleigh-based PAH formulations with real-world data, a set of exemplary array measurements were taken in the lab. In particular, a sparse point source-like case and a damped plate with modal vibrations were measured.

4.1 MEASUREMENT SETUP

For the measurement, a microphone array developed by the institute of electronic music and acoustic in Graz (IEM) is used. This array was originally built in the scope of the thesis of Hofer [31] to apply Fourier-based NAH to planar acoustic emission. It consists of 64 measurement microphones that are attached to the array in a way that the microphone distance can be easily changed. The 64 microphone signals are transmitted to the PC via MADI and recorded in *pure data*[1]. Gain alignment is achieved by a reference signal of a pistophone with a level of 104dB at 1000Hz. Further evaluation of the measurement data was performed with MATLAB. The array and the signal conversion front end is depicted in figure 4.1.

(a) Microphone array

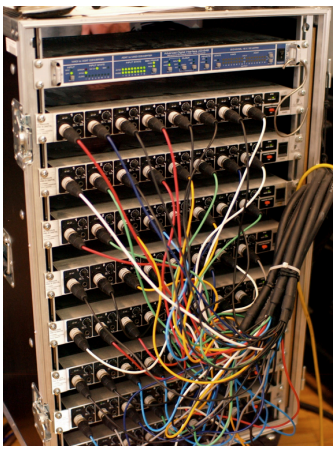

(b) Front end

Figure 4.1: 64-channel microphone array hardware

For our purpose, an aperture of the size $0.56\text{m} \times 0.56\text{m}$ was set up. This leads to a microphone distance of $d = 7\text{cm}$ and therefore to a upper frequency limit of 2450Hz for planar waves, before spatial aliasing might occur.

1 Pure data is an open source real-time computer music programming language with multi-channel audio processing characteristics.

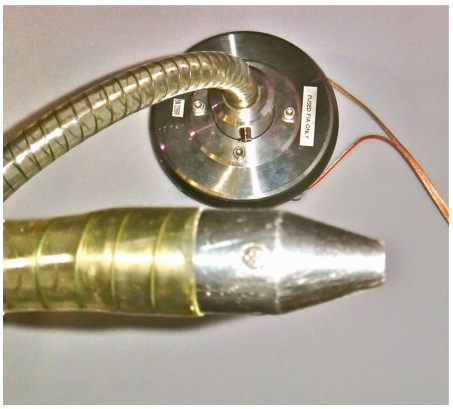

(a) Volume acceleration source from LMS

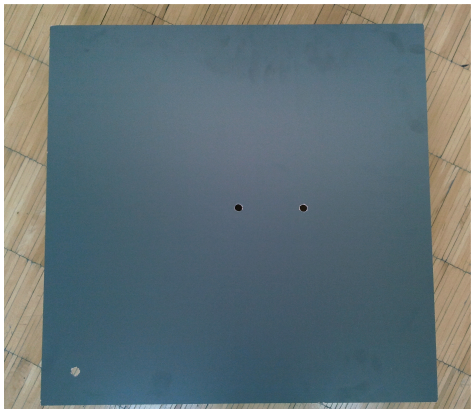

(b) prepared point source plane

Figure 4.2: Localized structural vibration measurement setup

As a localized structural vibration example, a *mid-high frequency volume acceleration source* from LMS is used which consists of a tube, mounted onto a horn driver. At the end of this tube, a nozzle is positioned at which a measurable velocity signal is emitted. The aperture of the nozzle is $0.9\text{cm} \times 0.9\text{cm}$. Figure 4.2 illustrates the source and its components. To ensure the claimed boundary conditions at the source plane, the tip of the nozzle was fixed on a sound-reflecting plate of the dimensions $0.6\text{m} \times 0.6\text{m}$. Three positions are measured (mid, right-mid, lower left corner).

(a) Exciter from ELAC

(b) panel clammed in frame

Figure 4.3: Clamped DML-panel with exciter on its backside

As a spread mode example, a plate of rigid foamed plastic (so called DML-panel), which is clamped at the rim and driven by a standard audio exciter is used. The exciter is attached to the backside of the panel at its upper right corner to ensure an excitation of many mode shapes (cf. figure 4.3). The size of the panel is $0.33 \times 0.52\text{m}$. The 8×8 measurement grid is positioned at

a distance of $d = 0.065m$ with a microphone spacing of $d_x = 4.95cm$ in x-direction and $d_y = 6.0cm$ in y-direction. Therefore, the maximum resolvable frequency without farfield aliasing is 2858Hz.

The measurement took place in a room with a $4m \times 4m \times 3.3m$ measurement cabin installed. The acoustic treatment of the environment is considered sufficiently, but not anechoic.

4.2 MEASUREMENT

The measurement over a broad frequency range was realized using exponential sweeps. This technique, which is extensively covered in the work of Torras and Jacobsen [32], exploits the property of its excitation to separate harmonic distortions from the rest of the electroacoustic transfer function. The impulse response of the given source-microphone path is calculated as follows:

$$h(t) = iDFT\left(\frac{DFT(p(t))}{DFT(s(t))}\right) , \tag{4.1}$$

where
$p(t)$ microphone signal (measured sweep)
$s(t)$ exponential sweep .

The inverse Fourier transform separates the harmonic distortion components of the measurement to a point ahead in time of the actual impulse response. Therefore, these can be simply removed. The final impulse responses are used to calculate the solutions of the PAH at several frequencies.

4.3 ERROR

An important aspect for the evaluation of a system is its error. For the simulations and the measurements, we specify two errors: The single value error, which sums the distance of the reconstruction to the original and an error matrix that illustrates the derivation of the optimized solutions at each individual point. Both values may be useful, depending on the given situation. The *single value error* is a relative magnitude error as given in [20]:

$$e = \sqrt{\left(\frac{\sum_{j=1}^{N}\left(|v_{calc}| - |v_{orig}|\right)^2}{\sum_{j=1}^{N}|v_{orig}|^2}\right)} , \tag{4.2}$$

where
$\mathbf{v}_{orig}$ Original velocity components
$\mathbf{v}_{calc}$ Calculated velocity components .

It delivers a simple scalar measure to compare two different holographic results.

The drawback is the missing indication about the location of the errors. An error measure providing this detailed information is the relative magnitude error without a summation across the spatial samples:

$$\mathbf{E} = \sqrt{\left(\frac{\left(|\mathbf{V}_{calc}| - |\mathbf{V}_{orig}| \right)^2}{\max |\mathbf{V}_{orig}|^2} \right)}, \tag{4.3}$$

where

$\mathbf{V}_{orig}$ Vector/Matrix of the original velocity components,

$\mathbf{V}_{calc}$ Vector/Matrix of the calculated velocity components .

4.4 RESULTS

Because the measurements take place in a real-world setup, noise due to the equipment, the room and the inaccuracies at the microphone positions might occur. Therefore, we need to apply the regularization parameter β, to exclude the influence of noise on the results. In the holographic processing, this parameter is always chosen suitably as denoted in the title of each plot. All localized point-shape examples are calculated on a 60×60 grid of the holographic image to arrive at the size of the source aperture for a single holographic component. This is chosen due to the real aperture of the applied point source. The grid for the modal vibration example was chosen to be 40×40 points.

4.4.1 *Measurement of point source*

For the analysis of localized point-shape vibrations, three frequencies at 300Hz, 1000Hz and 3000Hz are selected in accordance with the former chapters. As already described, the point source is positioned at three different locations (mid, mid-right, lower left corner). The emitted velocity is determined using the internal volume probe of the LMS acceleration source and shown in table 4.1. For the sparse holographic calculation, the MATLAB toolbox *cvx* is used again.

	300Hz	1000Hz	3000Hz
emitted velocity	$\mathbf{245}\frac{\mathbf{m}}{\mathbf{s}}$	$\mathbf{627}\frac{\mathbf{m}}{\mathbf{s}}$	$\mathbf{823}\frac{\mathbf{m}}{\mathbf{s}}$

Table 4.1: Velocity of the LMS point source

Before the benefits of the sparse holographic imaging are presented, the sparse problem is analyzed using the least-squares solution. Figure 4.4 displays the results and illustrates its serious flaws concerning localization.

Comparing these results with the exciting velocity, we observe that the sparse holographic imaging technique is well motivated as sharp edges and discontinuities are smeared. We encounter the same artifacts as for the

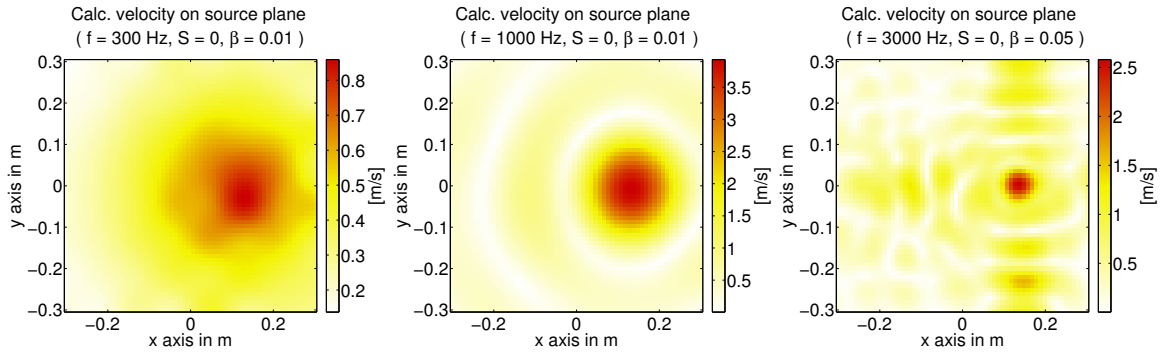

Figure 4.4: Calculated normal velocity for a measurement distance $a = 0.07m$ with 8×8 sensor positions at different frequencies for a sparsity $S = 0$ of a sparse real-world problem

simulation study in chapter 2.2.4. Sidelobes emerging around the peak at 1000Hz, for example, originate from the measurement distance and the thereby introduced spatial filtering. Increasing the frequency to 3000Hz leads to additional aliasing artifacts due to the microphone spacing. The localization of the source might be possible in this simple setup, however for more complex excitation patterns, the task will most likely become futile.

To enhance the result concerning the value of the velocity and its exact localization, the calculation is repeated using sparse holographic imaging introduced in chapter 3. At the analysis frequency of 300Hz, a good and sparse localization of the source at all positions is obtained as figure 4.5 displays. Specific attention is drawn to the adjustment of β. On the one hand, this regularization parameter suppresses noise in the sparse image. On the other hand, it is easy to over-regularize the optimization, which leads to a decrease of the resulting velocity magnitude. Therefore, the value has to be adapted very carefully. The resulting velocity values are also described in table 4.2.

Despite the artifacts caused by the distance of the aperture, the results of the evaluation at 1000Hz are satisfying, too. The slight deviation compared to the source velocity most likely originates from measurement imprecision. However, we encounter a significant degeneration of the result for the point positioned in the corner of the source plane[2]. The reason for this decrease might be sound pressure components, which are simply not measured due to the limited array aperture. It is known from Fourier-based NAH that the measurement aperture should exceed the source plane in size, to come to a reasonable result. A similar demand for Rayleigh-based PAH could be a solution to this problem. However, further investigation would be required to prove this statement.

2 This can already be observed for the analysis at 300Hz

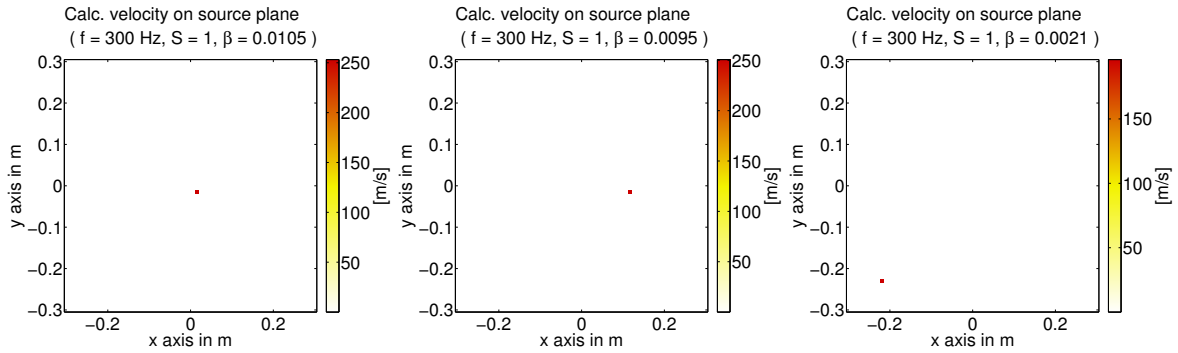

Figure 4.5: Calculated normal velocity for a measurement distance $a = 0.07m$ with 8×8 sensor positions at 300Hz and a sparsity $S = 1$ of a sparse real-world problem

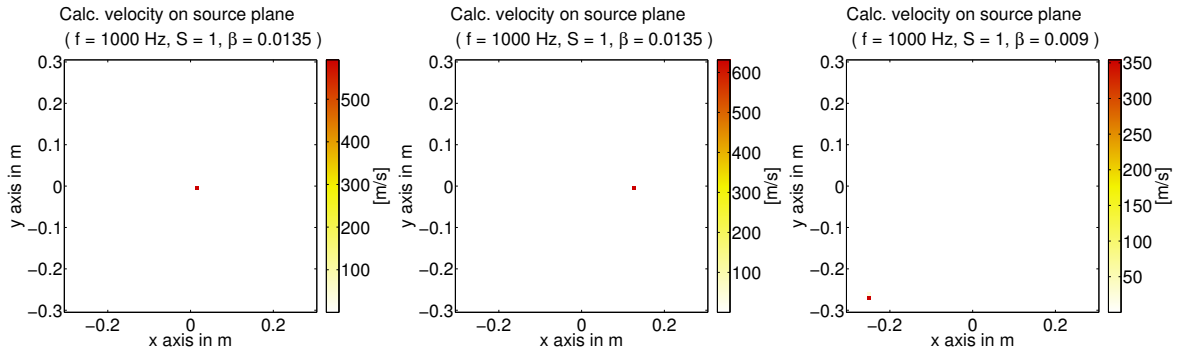

Figure 4.6: Calculated normal velocity for a measurement distance $a = 0.07m$ with 8×8 sensor positions at 1000Hz and a sparsity $S = 1$ of a sparse real-world problem

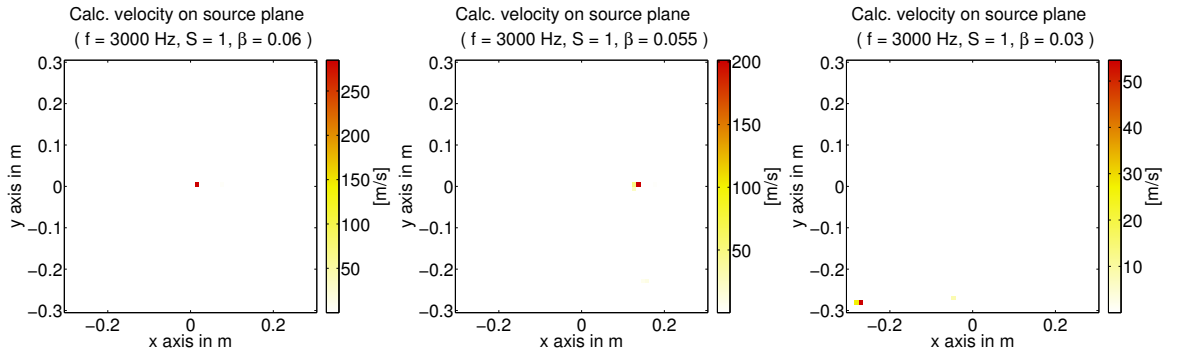

Figure 4.7: Calculated normal velocity for a measurement distance $a = 0.07m$ with 8×8 sensor positions and at 3000Hz a sparsity $S = 1$ of a sparse real-world problem

The least-squares solution displayed in figure 4.4 already revealed the disturbing influence of aliasing. The question arises of how this affects the sparse holographic image. Examining the sparse optimization at 3000Hz in figure 4.7 reveals that the localization is still acceptable. However the regu-

larization parameter β was increased to suppress aliasing components that emerge as speckles around the source position. In return, this leads to a decrease of the optimized velocity as illustrated in table 4.2.

	mid	side	edge
300Hz	$253\,\frac{\mathrm{m}}{\mathrm{s}}$	$251\,\frac{\mathrm{m}}{\mathrm{s}}$	$196\,\frac{\mathrm{m}}{\mathrm{s}}$
1000Hz	$592\,\frac{\mathrm{m}}{\mathrm{s}}$	$632\,\frac{\mathrm{m}}{\mathrm{s}}$	$354\,\frac{\mathrm{m}}{\mathrm{s}}$
3000Hz	$285\,\frac{\mathrm{m}}{\mathrm{s}}$	$201\,\frac{\mathrm{m}}{\mathrm{s}}$	$55\,\frac{\mathrm{m}}{\mathrm{s}}$

Table 4.2: Measured velocity results for the sparse optimization

4.4.2 *Measurement of a vibrating DML-panel*

To analyze the vibrating panel, the resonance frequencies are determined first. For this, the averaged Fourier transform of all impulse responses is depicted in figure 4.8.

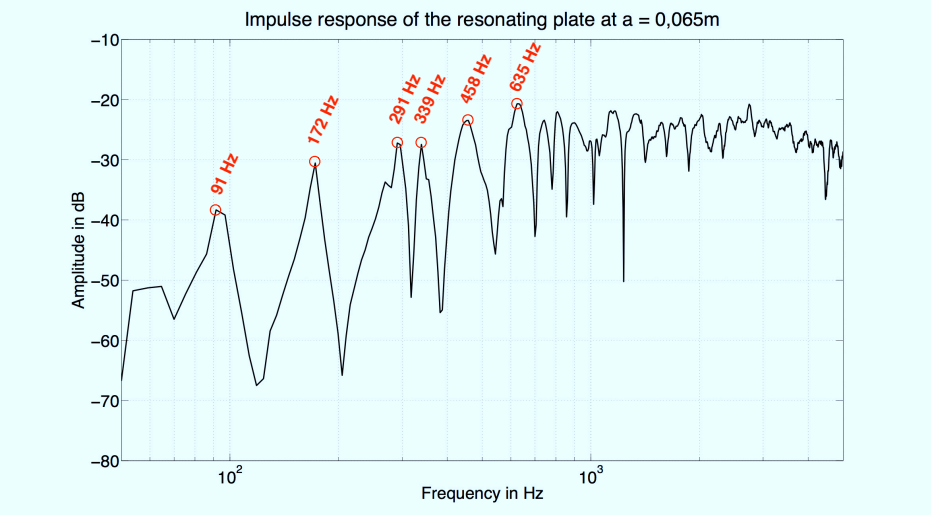

Figure 4.8: Impulse response of the resonating plate

Six modes are chosen for a thorough analysis. The holographic reconstruction of the source velocity is again calculated using the optimization toolbox *cvx* in MATLAB. To give an overview of the mode structure, the least-squares optimized solution of the source velocity is illustrated in figure 4.9. Because these real-world measurements might contain noise artifacts, the solution is regularized.

We observe the mode structure of the panel clearly. This experiment confirms that the least-squares optimization of the Rayleigh-based PAH works very well for problems where the exciting velocity is broadly distributed with no discontinuities at the source.

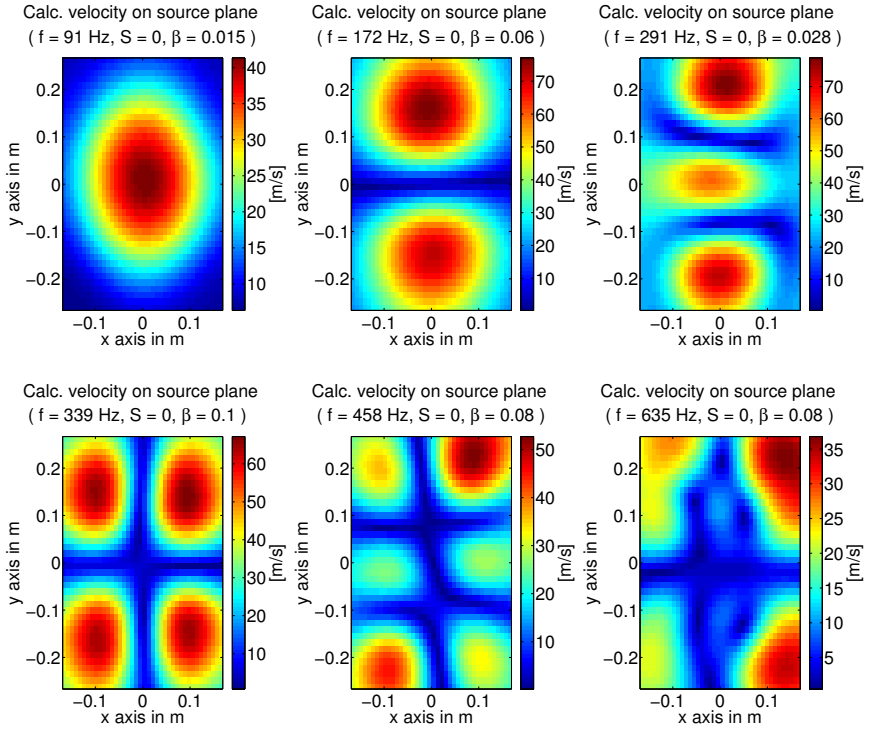

Figure 4.9: Calculated normal velocity for a measurement distance $a = 0.065m$ with 8×8 sensor positions and a sparsity $S = 0$ (= least-squares optimization) of a real-world measurement.

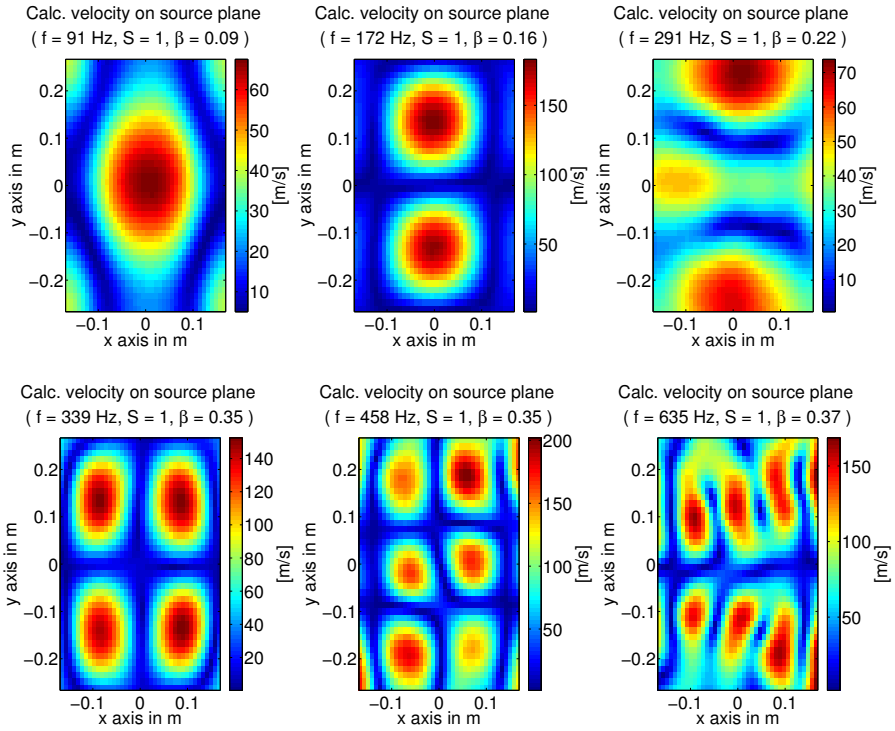

Figure 4.10: Calculated normal velocity for a measurement distance $a = 0.065m$ with 8×8 sensor positions and a sparse mode optimization of a real-world measurement.

Knowing that the underlying excitation complies with a mode structure, we can apply sparsity in the modal domain as described in chapter 3.2.3. Although the regularization for the mode-sparse optimization is tricky and no further optimization in k-space was performed, it turns out that the results are promising (cf. figure 4.10). Compared to the least-squares solution, a cleaner mode structure is observed, especially for the evaluation at 458Hz and 635Hz. The three modal lines of the 635Hz mode were not even resolved in the holographic analysis of figure 4.9. Nevertheless, noise can easily corrupt the solution, especially at higher frequencies where a blurring occurs. Another problem appears at the frequency of 291Hz, where the source velocity seems to inherits some cyclic elements from the Fourier transform that was applied.

Although we know that sparsity in space is nonsense for identifying the modes of a plate, it can be used to accurately detect the point of the maximal displacement. For this, the sparsity parameter S is adjusted to come to a good trade-of between mode recognition and peak detection. The result is illustrated in figure 4.11 for the mode at $f = 291\text{Hz}$.

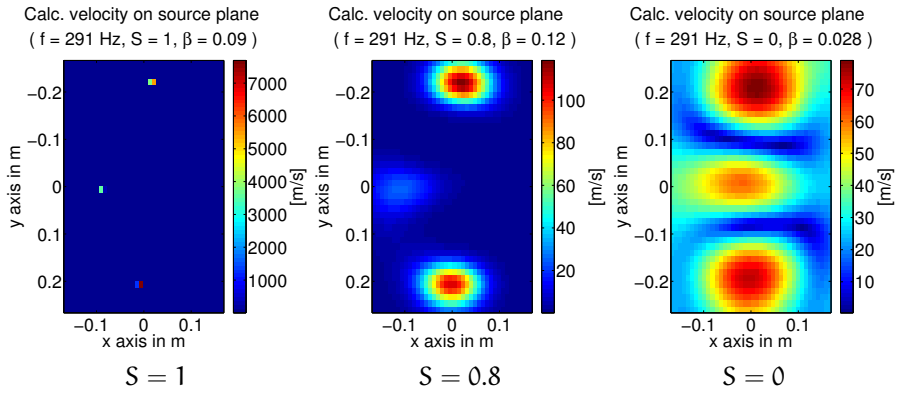

Figure 4.11: Calculated normal velocity for a measurement distance $a = 0.065\text{m}$ with 8×8 sensor positions and different values for Sparsity S

The results of the real-world measurements illustrates the capabilities of the Rayleigh-based PAH. Structures that are broadly excited in space are resolved and reasonable solutions are calculated using the standard least-squares based holography. For problems that are known to be sparse in space or modes, we can expand the formulation to sparse holographic imaging. With this optimization, point sources and modes can be identified in a very accurate way.

By the application of the newly introduced parameter of the sparsity S, it is also possible to blend between the solutions. Trade-offs between least-squares and sparse optimization can help to either give a broad overview of mode structures or enforce an exact localization of the maximum displacement on the source plane.

The regularization parameter β helps to exclude noise components from the holographic image and leads to a good applicability to real-world measurements.

5

CONCLUSION AND FUTURE WORK

5.1 CONCLUSION

This thesis presents a formulation for acoustic holography based on Rayleigh integrals in particular aiming at methods for improved resolution. The objective is to recalculate the exciting structure velocity from a limited number of measured sound pressure signals. The benefit of the proposed expression is its simplicity and the formulation as an underdetermined linear equation system. Using the tools of linear algebra, an optimal solution of the system in the least-squares sense is easily achieved. Simulations and measurements confirmed that this solution works well for broadly excited, modal structure vibrations. However it works poorly for sparse and localized vibration as the holographic image is strongly smeared and the velocity magnitude is underestimated.

To solve this deficiency, convex optimization using the ℓ_1-norm was introduced to solve underdetermined holography equations. This enforces sparse solutions on the source plane and leads to a good localization and an improved velocity magnitude. The performance was tested using simulations and real-world measurements and yield convincing results. This optimization was also applied to modal problems. Exploiting the ideas of compressive sampling theory, a sparse representation of modal structure vibration was found. The optimization was then performed in the k-space-domain and yields promising results that outperformed the classical least-squares holographical image.

Real-world problems are usually neither perfectly sparse, nor exclusively resonating phenomena. Therefore, a simple criterion to blend between least-squares and sparse optimization is of great benefit. A new parameter was introduced to do so. It was called *sparsity* and was used to enforce sparse solutions where it is necessary or to give a clue about modal structure vibration. Simulations of a mixed source setup revealed that the application of this parameter is necessary to arrive at reasonable holographic images.

5.2 FUTURE WORK

A drawback of the sparse optimization is the increased computational cost compared to conventional Fourier-based NAH or the proposed least-squares solution. However, as research of sparse optimization is recent, more efficient algorithms can be expected in the nearer future. Even to-

day, iterative algorithms are known to accelerate this task. The application of those techniques should be investigated to come to faster implementations of sparse holographic imaging.

Further research might also focus on the errors and the limits of the Rayleigh-based PAH in real-world setups. Topics such as measurement aperture size or maximum aperture distance are not sufficiently discussed yet. Techniques to reduce resulting errors, such as regularization in the spatial domain or k-space, also provide a large field of future investigations.

APPENDIX

APPENDIX A

A.1 SPARSE EVOLUTION FOR A MULTI-DIMENSIONAL PROBLEM

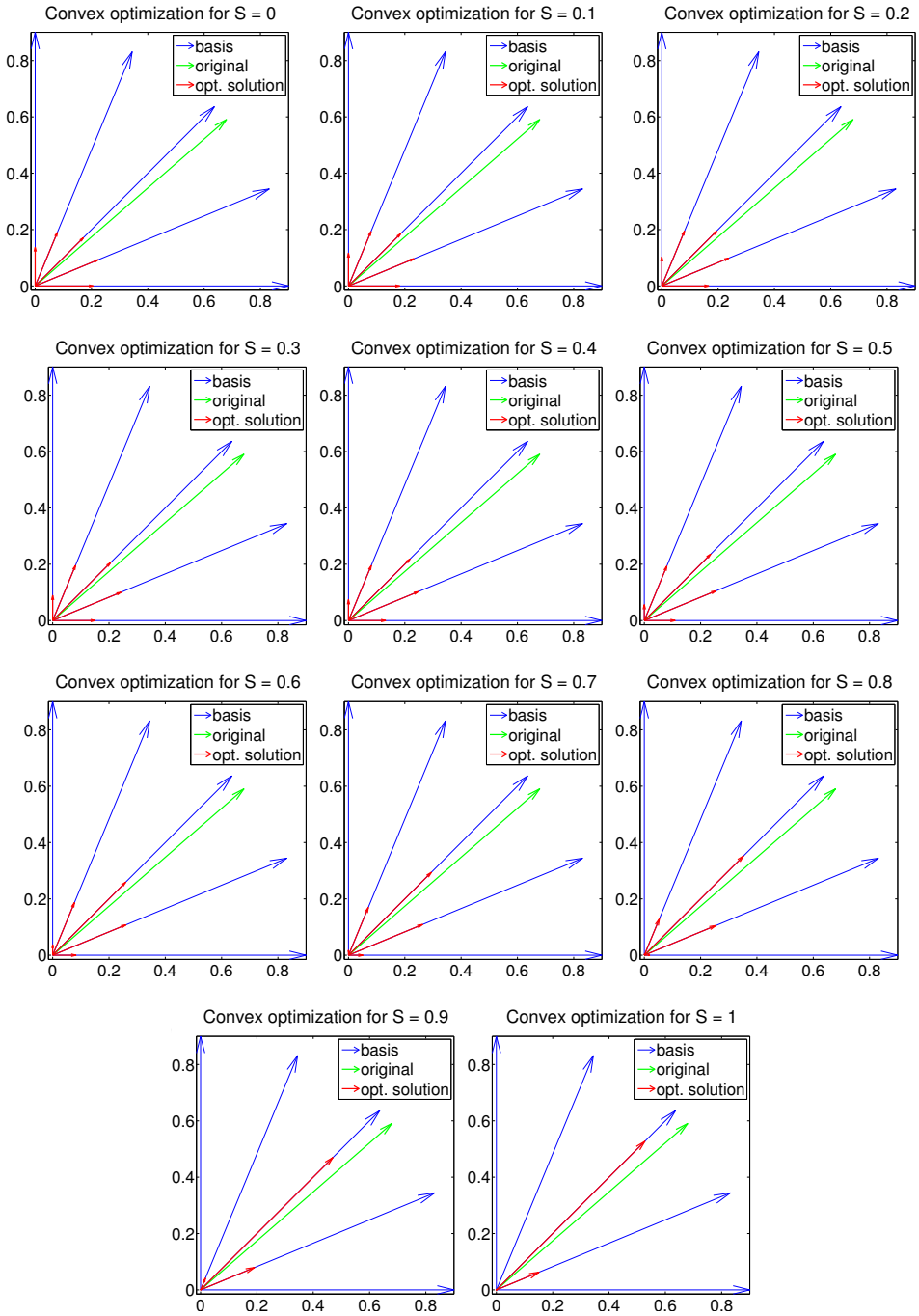

Figure A.1: Optimization for different values of sparsity S

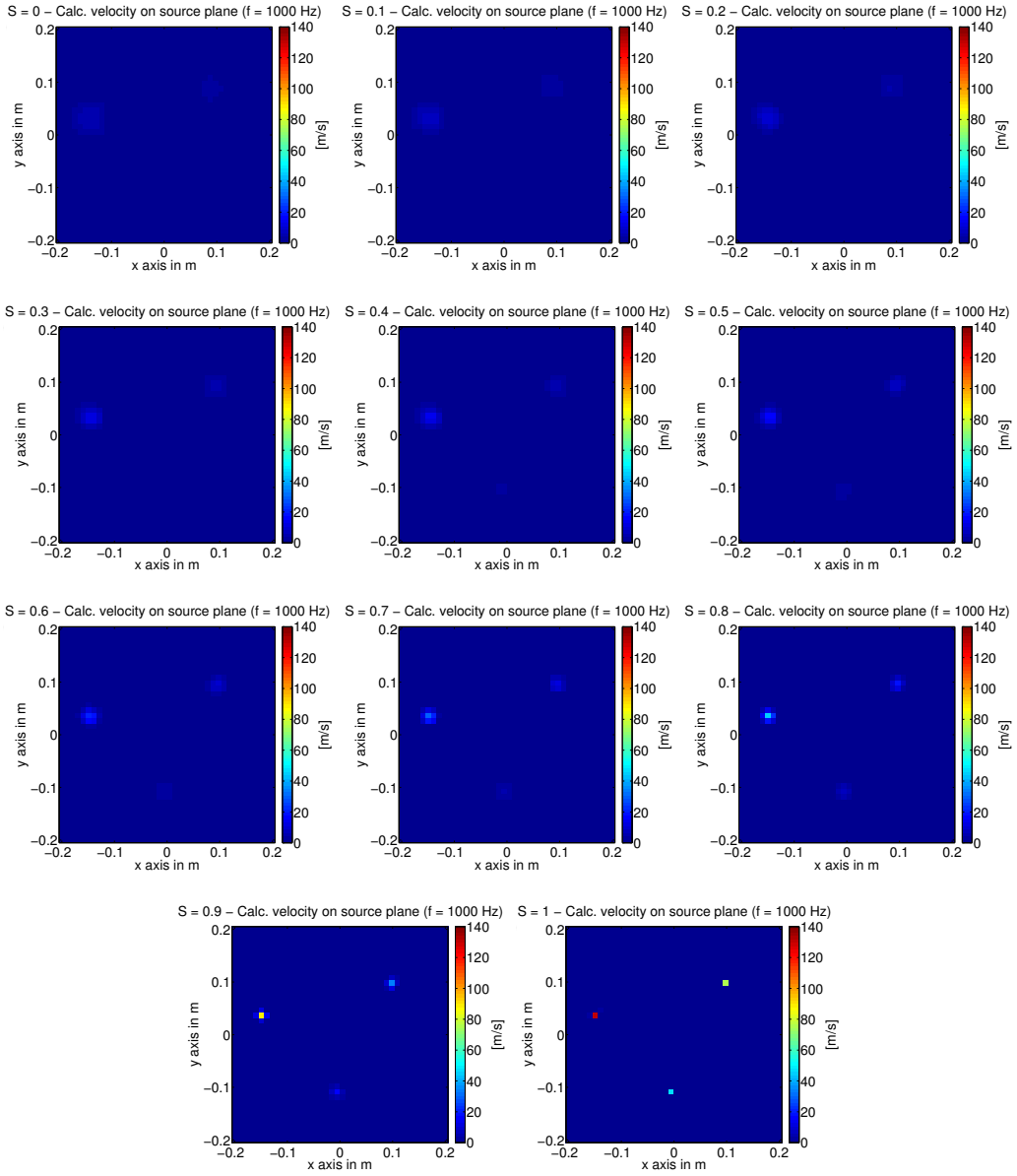

Figure A.2: Optimization of a problem sparse in space for different values of sparsity S, simulated for an 8×8 sensor array at a distance of $a = 0.05m$ and a frequency of 1000Hz

A.3 EVOLUTION OF SPARSITY S FOR RESONATING PLATE

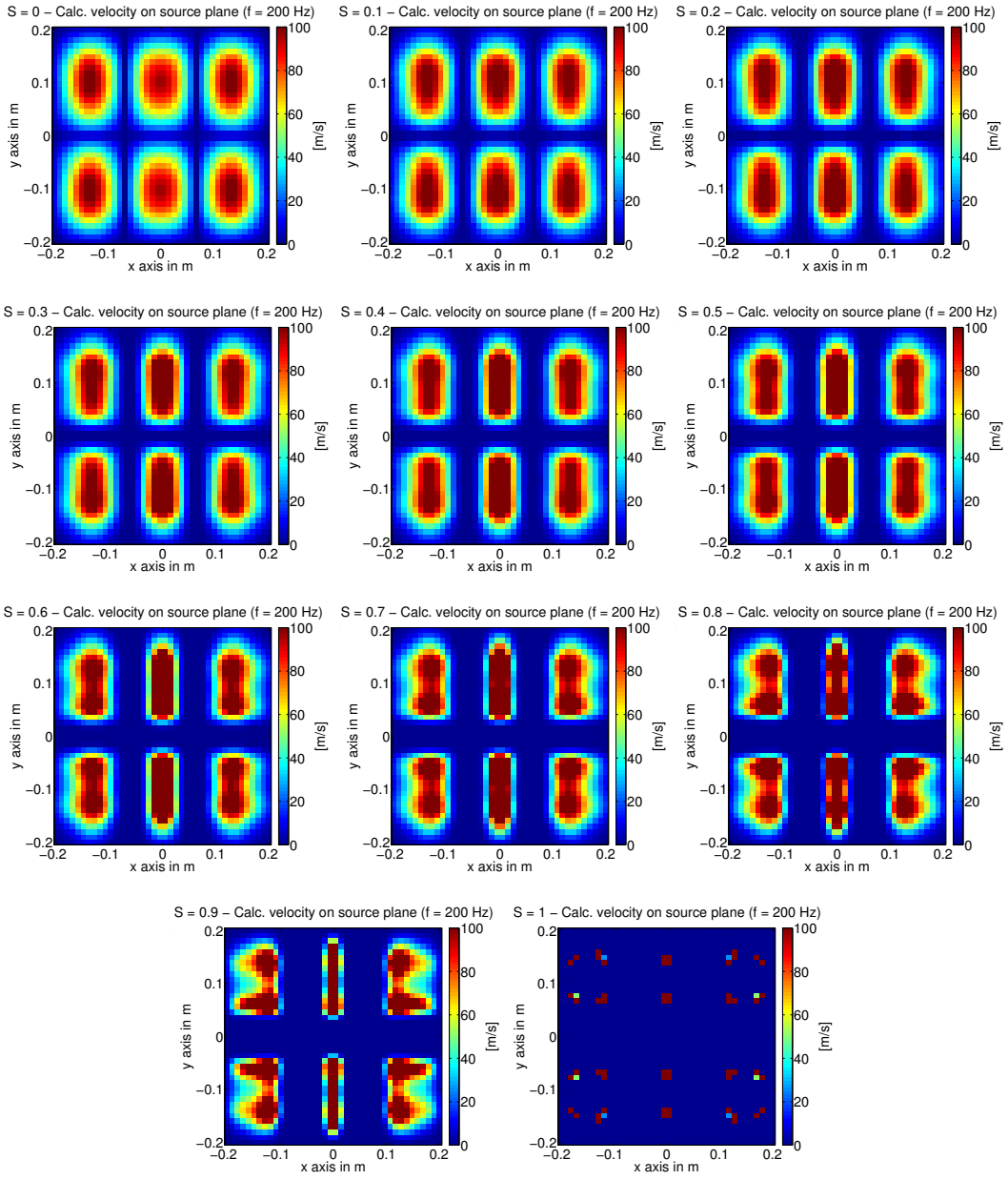

Figure A.3: Optimization of a resonating plate for different values of sparsity S, simulated for an 8×8 sensor array at a distance of $a = 0.05m$ and a frequency of $200Hz$

A.4 EVOLUTION OF SPARSITY FOR A COMBINED PROBLEM WITH RESONANCES AND SPARSE PEAKS

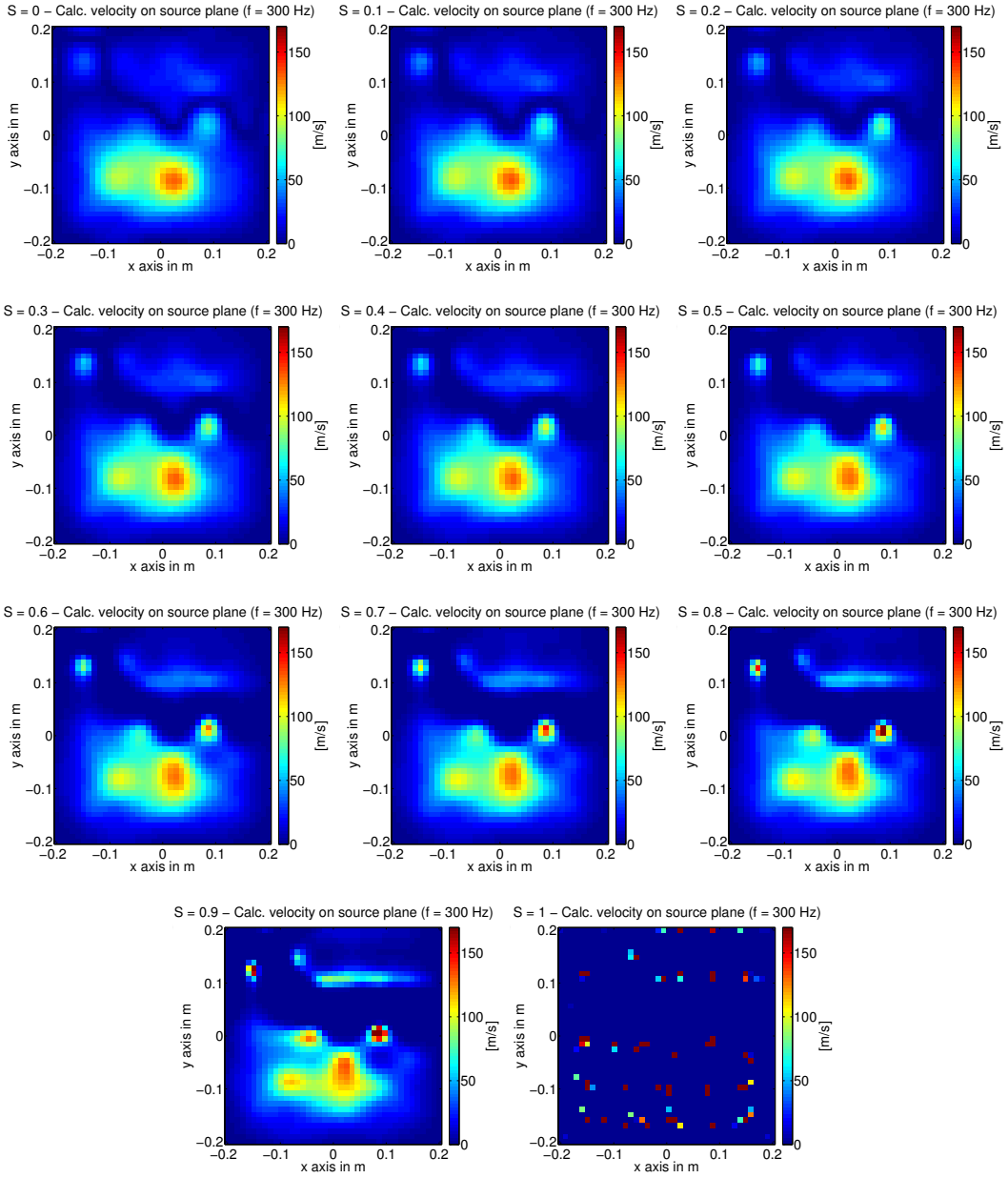

Figure A.4: Optimization of the combined problem for different values of sparsity S, simulated for an 8×8 sensor array at a distance of $a = 0.05\text{m}$ and a frequency of 300Hz

BIBLIOGRAPHY

[1] S. F. Wu, "Methods for reconstructing acoustic quantities based on acoustic pressure measurements," J. Acoust. Soc. Am., vol. 124, 2008.

[2] J. Maynard and E. Williams, "Nearfield acoustic holography: I. Theory of generalized holography and the development of NAH," J. Acoust. Soc. Am., 1985.

[3] J. Hald, "Basic theory and properties of statistically optimized near-field acoustical holography," J. Acoust. Soc. Am., vol. 125, 2009.

[4] G. H. Koopmann, "A method for computing acoustic fields based on the principle of wave superposition," J. Acoust. Soc. Am., vol. 86, 1989.

[5] Z. Wang, "Helmholtz equation–least-squares method for reconstructing the acoustic pressure field," J. Acoust. Soc. Am., 1997.

[6] W. A. Veronesi, "Digital holographic reconstruction of sources with arbitrarily shaped surfaces," J. Acoust. Soc. Am., vol. 85, 1989.

[7] Frank Fahy, "Foundations of Engineering Acoustics", Academic Press, 2003

[8] Thomas D. Rossing (Ed.), "Springer Handbook of Acoustics", Springer, 2007

[9] Allan D. Pierce, "Acoustics - An Introduction to Its Physical Principles and Applications", Acoustical Society of America, 1989

[10] Frank Fahy (Ed.), John Walker (Ed.), "Fundamentals of Noise and Vibration", E & FN SPON, 1998

[11] Earl G. Williams , "Fourier Acoustics - Sound Radiation and Nearfield Acoustical Holography", Academic Press, 1999

[12] G. Golup, C.F. Van Loan, "Matrix Computations", The Johns Hopkins University Press, 1989

[13] F. Zotter, H. Pomberger, "Acoustic Holography and Holophony - Lecture notes," Nov. 2011.

[14] J. Ahrens, "The single-layer potential approach applied to sound field synthesis including cases of non-enclosing distributions of secondary sources", Dissertation TU Berlin, 2010.

[15] Philip M. Morse, K. Uno Ingard, "Theoretical Acoustics",Princeton University Press, 1987.

[16] E. N. G. Verheijen, “Sound reproduction by wave field synthesis,” 1998.

[17] Adi Ben-Israel, Thomas N. E. Greville ”Generalized Inverses: Theory and Applications”, Springer, 2003

[18] E. J. Ientilucci, “Using the singular value decomposition,” Rochester Institute of Technology, 2003.

[19] E. G. Williams, B. H. Houston, and P. C. Herdic, “Fast Fourier transform and singular value decomposition formulations for patch nearfield acoustical holography,” J. Acoust. Soc. Am., vol. 114, 2003.

[20] A. Sarkissian, “Method of superposition applied to patch near-field acoustic holography,” J. Acoust. Soc. Am., vol. 118, 2005.

[21] E. Williams, “Regularization methods for near-field acoustical holography,” J. Acoust. Soc. Am., 2001.

[22] R. Scholte, “Fourier based high-resolution near-field sound imaging”, Dissertation Technische Universiteit Eindhoven, 2008.

[23] Technische Akustik
M.Möser; Springer, 2007

[24] Vorlesungen über Technische Akustik
L. Cremer; H.A. Müller ; Springer, 1990

[25] N. P. Valdivia and E. G. Williams, “Study of the comparison of the methods of equivalent sources and boundary element methods for near-field acoustic holography,” J. Acoust. Soc. Am., vol. 120, 2006.

[26] B. HAYES, “The best bits,” American scientist, vol. 97, 2009.

[27] M.Elad, ”Sparse and Redundant Representations - From Theory to Applications in Signal and Image Processing ”, Springer, 2010

[28] S. S. Chen, D. L. Donoho, and M. A. Saunders, “Atomic Decomposition by Basis Pursuit,” SIAM Journal on Scientific Computing, vol. 20, 1998.

[29] S. P. Boyd and L. Vandenberghe, “Convex optimization,” 2004.

[30] D. Malioutov, “A sparse signal reconstruction perspective for source localization with sensor arrays”, Master thesis MIT, 2003.

[31] D. Hofer, “Implementierung eines 64 Kanal Mikrofonarrays,” Diploma thesis IEM, 2008.

[32] A. Torras-Rosell, “A New Interpretation of Distortion Artifacts in Sweep Measurements,” Journal of the Audio Engineering Society, 2011.

EIDESSTATTLICHE ERLÄRUNG

Ich erkläre an Eides statt, dass ich die vorliegende Arbeit selbstständig verfasst, andere als die angegebenen Quellen/Hilfsmittel nicht benutzt, und die den benutzten Quellen wörtlich und inhaltlich entnommenen Stellen als solche kenntlich gemacht habe.

Graz, May 29, 2012

Philipp Schmidt

STATUTATORY DECLARATION

I declare that I have authored this thesis independently, that I have not used other than the declared sources / resources, and that I have explicitly marked all material which has been quoted either literally or by content from the used sources.

Graz, May 29, 2012

Philipp Schmidt